

AD-A108 140

UNITED TECHNOLOGIES RESEARCH CENTER EAST HARTFORD CT F/0 20/14
INFLUENCE OF CONTACT CONDITIONS AND THE CIRCUIT ON SHORT NEGATI--ETC(U)
AUG 81 H L GRUBIN N00014-78-C-0269

UNCLASSIFIED

2

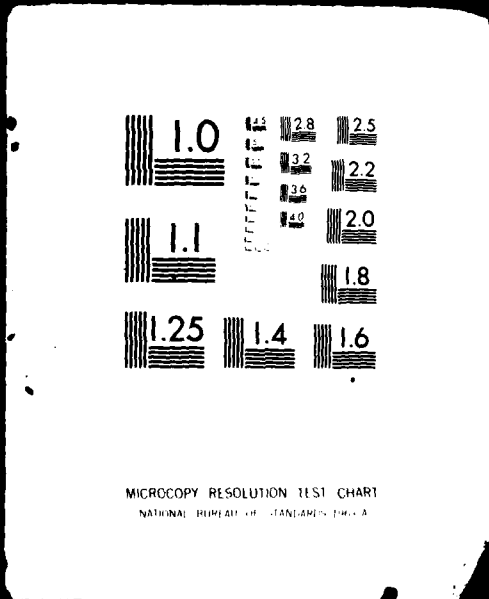
400000

ML

IFIED

1 OF 2

AD A108140



12

LEVEL II

AD A108140

**INFLUENCE OF CONTACT CONDITIONS AND THE CIRCUIT
ON SHORT NEGATIVE DIFFERENTIAL MOBILITY SEMICONDUCTING DEVICES**

Final Report for ONR
under Contract N00014-78-C-0269

DTIC ELECTE
S D
DEC 4 1981
D

Prepared by
H. L. Grubin

DTIC FILE COPY

DISTRIBUTION STATEMENT A
Approved for public release
Distribution Unlimited

01 79 00 000

x

Studying the Physics and Operation of Multi-terminal Near-
and Sub-micron Length, Hot Electron Semiconductor Devices

Final Report for ONR
under Contract N00014-78-C-0269

3 Aug. 1981

Accession For	
NTIS GRA&I	<input checked="" type="checkbox"/>
DTIC TAB	<input type="checkbox"/>
Unannounced	<input type="checkbox"/>
Justification	
By <i>Per ltr. on file</i>	
Distribution/	
Availability Codes	
Dist	Avail and/or Special
A	

Prepared by
H. L. Grubin

DTIC
ELECTE
DEC 4 1981
S D
D

DISTRIBUTION STATEMENT A
Approved for public release
Distribution Unlimited

Studying the Physics and Operation of Multi-terminal Near-
and Sub-micron Length, Hot Electron Semiconductor Devices

TABLE OF CONTENTS

	<u>Page</u>
SUMMARY	ii
I. INTRODUCTION.	I-1
II. SUMMARY OF STUDIES UNDER ONR CONTRACT N00014-78-C-0269.	II-1
II.1 Introduction.	II-1
II.2 Scattering Integrals.	II-3
II.3 Studies Using the Drift and Diffusion Equation.	II-4
II.4 Studies Using the Boltzmann Transport Equation.	II-5
II.4.i Transient Overshoot	II-5
II.4.ii Bias Dependence of Overshoot.	II-7
II.4.iii Self-Excited Oscillations	II-8
II.4.iv Length Dependence of Negative Differential Mobility Region	II-8
II.4.v Spatial Transients in Short Channel GaAs Devices.	II-9
III. RECENT PUBLICATIONS UNDER ONR CONTRACT N00014-78-C-0269	III-1
IV. NUMERICAL CODES, PARTIALLY SPONSORED BY ONR, CONTRACT N00014-78-C-0269	IV-1
V. REFERENCES.	V-1
VI. FIGURE CAPTIONS	VI-1

TABLE

FIGURES

Studying the Physics and Operation of Multi-terminal Near-
and Sub-micron Length, Hot Electron Semiconductor Devices

SUMMARY

This final report, N00014-78-C-0269, summarizes recent studies by H. L. Grubin, the Principle Investigator, as they relate to near- and sub-micron device physics studies.

I. INTRODUCTION

During the last two or three years we have seen a remarkable resurgence of interest in the physics of nonlinear semiconductor devices and transport. While there are probably as many reasons for this development as there are practitioners, we can group them into several categories.

First there are the anticipated fruits of the VLSI and VHSIC programs. These programs are geared primarily to the development of conventionally conceived devices fabricated on a submicron scale, and provide the primary motivation for all other submicron programs. While the VLSI and VHSIC development will provide new, important military and commercial gains, its potential accomplishments are limited by our present understanding of semiconductor device physics. Most devices fabricated as part of this program use design tools generated by semiclassical transport, the best known being the mobility concept where the carriers respond instantaneously to changes in electric field.

The inadequacy of the mobility concept for submicron length high speed devices was raised implicitly by Butcher and Hearn in 1968 (Ref. 1); and Rees in 1969 (Ref. 2); and explicitly by Ruch in 1972 (Ref. 3) in his well-known paper on velocity overshoot. Indeed, Ruch's paper was a watershed for device transport studies insofar as it focused attention on the transient dynamics of carrier transport and showed that the response of the carrier velocity to a sudden change in field was considerably different from that associated with mobility models. In fact, values of velocity three or four times higher than steady state values were commonly reported. With the exception of a few workers, e.g., Refs. 4-6, there was not much follow-up to Ruch's study. The situation changed dramatically in the late 1970's with a plethora of papers on transient carrier dynamics. At this time, we also saw private industry increasingly able to fabricate submicron length electron devices while simultaneously expressing concern about transient effects on device performance, particularly with regard to GaAs FET's. Of significance were such questions as: (1) could the high transient velocities be adequately exploited in submicron design geometries, (2) could negative differential mobility be eliminated from sufficiently short submicron devices. Answers were rapid in coming, but they were of a patchwork quality insofar as they were based primarily on uniform field calculations. Thus, while temporal transients received a great deal of attention, spatial transients were largely ignored. In spite of the broad range of assumptions here, it has become increasingly clear that a physics of submicron devices has been developing, one that we have been calling the numerical physics of semiconductor devices: see Grubin, et al. (Ref. 7).

The numerical physics of semiconductor devices serves to determine the temporal and spatial transient dependence of submicron length electron devices and to account as well as possible for the environment surrounding the device. As indicated

above, however, most activities are based upon uniform field calculations, although Rees, and Rees, et al. (Ref. 8) have made major advances in the art of numerical device analysis when nonuniform fields are present. While the need for nonuniform field calculations is apparent, Rees' methods are not finding widespread use, due primarily to high computational costs. Instead, for nonuniform fields and multi-dimensional device simulations, more frequent use is made of the method of moments as applied to the Boltzmann transport equation (BTE). Here the most common form for the moment equation is that summarized by Blotekjar (Ref. 9) under the assumption that the carriers are described by a displaced Maxwellian function. Representative calculations using these equations appear, for uniform fields in Ref. 1 (Butcher and Hearn), and Ref. 10 (Grubin, Ferry and Barker), for nonuniform fields and micron length variations in Ref. 11 (Bosch and Thim), and Ref. 12 (Cheung and Hearn), for submicron length devices in Ref. 7 (Grubin, Ferry, Iafrate and Barker). And while there is widespread concurrence that realistic device simulations require the incorporation of spatial derivatives, the primary origins of the field non-uniformities associated with these derivatives is less certain. These must surely arise from contact effects (which are imperfectly understood from a device viewpoint), material variations (can background doping variations be adequately treated by 'jellium distributions'), environmental interactions (nearby devices and circuits). In addition, one-dimensional approximations to three-dimension devices are almost certainly inadequate for submicron length electron device simulations.

A variety of predictions have been made from simulations of submicron electron device behavior. In particular, as the device length shrinks, the peak velocity is expected to increase and the regions of negative differential mobility becomes less pronounced. In addition, a ballistic regime, where the carriers suffer no, or a few, collisions, is thought by some to be conceptually possible (see Ref. 13). The experimental observation of such effects occupies the third area of active interest, with workers in France, Laval, et al. (Ref. 14), and in the U.S., involved, e.g., Eastman, et al. (Ref. 15) and Zuleg (Ref. 16). While some of these experiments clearly demonstrate the length dependence of carrier transport, there are generally too many variables involved to allow an unequivocal explanation of device behavior.

The discussion above, with regard to the numerical physics of submicron length electron devices, has focused primarily on problems associated with the Boltzmann transport equation. The BTE is the cornerstone of semiclassical device transport drift and diffusion semiconductor equations. Its central concept is the idea of a single carrier distribution function, $f(r,p,t)$, which may be used to compute expectation values for macroscopic current flow. When we examine this idea from a quantum mechanical viewpoint, we see some necessary averaging if f is to be regarded as a simultaneous function of position and momentum. From a device perspective, care must therefore be exercised if f and/or the critical device dimension, L , is smaller than an electron wavelength, λ . For a quasi-particle with an effective mass m^*

$$\Lambda = h/m^* v_{\text{therm}} \quad (1)$$

where Λ is the thermal de Broglie wavelength. For GaAs central valley electrons $\Lambda \approx 270$ angstroms.

In addition to spatial consideration, from a temporal perspective, the BTE describes irreversible phenomena and it is assumed that collisions occur on a scale short compared to an observation time. Thus, e.g., relaxation times should be short compared to a transit-time. This assumption will be routinely violated in submicron devices and again caution must be exercised in using the BTE.

It is clear, that from a device modeling viewpoint, we are faced with serious problems. On the one hand, the BTE overcomes many objections to the use of the semi-conductor drift and diffusion equation. On the other hand, the above arguments suggest abandoning the BTE for ultrasmall devices and replacing it with a quantum transport formulation. While the latter may be necessary, the current approach is to retain the BTE as long as useful quantum effects can be incorporated. It is abandoned when first order quantum effects occur, as e.g., transport in quantized inversion layers.

A summary of the above discussion is represented by the flow diagram of Fig. 1. The arrows flow from the major motivating discipline to the new area of study.

In the following, we summarize recent work by the Principle Investigator on ONR Contract N00014-78-C-0269 as it relates to near- and submicron device physics studies. Detailed discussions of our studies are contained in published or submitted papers. A listing of these papers, along with select copies of them is included.

II. SUMMARY OF STUDIES UNDER ONR CONTRACT N00014-78-C-0269

II.1 Introduction

The studies carried out under ONR support involve the formulation and simulation of the transient behavior of transferred electron multiterminal one- and two-dimensional electron devices. The devices studied fall into two broad categories: (1) The first is for devices for which the current response is represented by the equation

$$\vec{J} = Ne \mu \vec{F} + e D \vec{\text{grad}} N + e \frac{\partial F}{\partial t} \quad (2)$$

where F is a field, μ the mobility, and D the diffusivity. This equation is based on the Boltzmann transport equation (BTE) for a distribution function only slightly modified by a self-consistent field. For high-field-nonlinear-hot-carrier-effects the distribution function is strongly dependent on F and the usual approach replaces μF by a nonlinear $v(F)$ curve, and D by a field dependent diffusivity; (2) The second category is for devices for which Eq. (2) is inadequate and the Boltzmann transport equation is needed:

$$\frac{\partial f}{\partial t} + \vec{V} \cdot \frac{\partial f}{\partial \vec{r}} + e \vec{F} \cdot \frac{\partial f}{\partial \vec{p}} = \int d\vec{p}' \left[f(\vec{p}') S(\vec{p}', \vec{p}) - f(\vec{p}) S(\vec{p}, \vec{p}') \right] \quad (3)$$

where $f(\vec{r}, \vec{p}, t)$ is the carrier distribution function, and $W(p', p)$ is a scattering kernel.

In our studies, Eq. (2) is often solved directly; Eq. (3) is not. Instead, working under the assumption that when the carrier concentration exceeds a critical concentration (i.e., provided that the rate of inter-carrier energy exchange is sufficiently large), the carrier distribution is taken to be a displaced Maxwellian.

$$f(\vec{p}_i) \propto \left(\frac{n_i}{T_i^{3/2}} \right) \exp - \left(\frac{(\hbar \vec{k} - \vec{p}_i)^2}{2m_i k_o T_i} \right) \quad (4)$$

Then the transport problem for a given spatially dependent field reduce to computing the carrier density, the displaced momentum and the electron temperature, for each valley of a multivalley semiconductor, such as GaAs or InP. These are obtained by self-consistently solving 3A balance equations, where A is the number of nonequivalent valleys. The balance equations are generated by multiplying the BTE by successive powers of k ; i.e., $\phi^j(k) = k^j$, where $j = 0, 1, 2$ and integrating over all k space. The result is

$$\frac{\partial}{\partial t} \langle \phi^j \rangle + \frac{\partial}{\partial \vec{r}} \cdot \langle \phi^j \vec{v} \rangle + e\vec{F} \cdot \langle \frac{\partial}{\partial \vec{p}} \phi^j \rangle =$$

$$\langle \int d\vec{p}' \left[\phi^j(\vec{p}') - \phi^j(\vec{p}) \right] S(\vec{p}, \vec{p}') \rangle$$
(5)

where the brackets represent \vec{k} -space integrations:

$$\langle () \rangle \equiv \int () f d\vec{k}$$
(6)

The first three moment equations are well known (see Ref. 9), and are summarized below (Particle Balance),

$$\frac{\partial N_i}{\partial t} + \nabla \cdot (\vec{v}_i N_i) = \left(\frac{\partial N_i}{\partial t} \right)_c$$
(7)

(Momentum Balance)

$$\frac{\partial \vec{P}_i}{\partial t} + \nabla \cdot (\vec{v}_i \vec{P}_i) = -e N_i \vec{F} - \nabla (N_i k T_i) + \left(\frac{\partial \vec{P}_i}{\partial t} \right)_c$$
(8)

(Energy Balance)

$$\frac{\partial W_i}{\partial t} + \nabla \cdot (\vec{v}_i W_i) = -e N_i \vec{v}_i \vec{F} - \nabla \cdot (\vec{v}_i N_i k T_i) - \nabla \cdot \vec{q}_i + \left(\frac{\partial W_i}{\partial t} \right)_c$$
(9)

where the subscripts identify a particular valley. Here,

$$\vec{P}_i = m_i N_i \vec{v}_i$$
(10)

$$W_i = \frac{3}{2} N_i k T_i + \frac{m_i}{2} N_i v_i^2$$
(11)

and m_i is the effective mass of electrons in the i^{th} valley. T_i is a measure of the average thermal energy of an electron, and W_i is regarded as the average total kinetic energy density. The terms in brackets on the right-hand side of Eqs. (7) through (9) represent scattering integrals.

Equations (8) and (9), for momentum and energy balance, represent the essential structural differences between the semiconductor, Eq. (4), and transport as given by the BTE. Apart from intervalley transfer, Eq. (7), the particle balance (or continuity) equation, is also required for the drift and diffusion equations.

Solutions to Eq. (4), with continuity, and to Eqs. (7) through (9), have occupied most of the Principle Investigators efforts over the past few years. We will illustrate results of this study below, but it is instructive to see how Eq. (4) is recovered from the balance equations. To do this, we need explicit representations for the scattering integrals.

II.2 Scattering Integrals

The scattering terms in Eqs. (7) through (9) may be approximated analytically or given exactly for a displaced Maxwellian distribution function. In our studies we have chosen the latter, and use the integrals summarized in Butcher's review article (Ref. 18). The scattering integrals are represented

$$\left(\frac{\partial N_i}{\partial t}\right)_c = \frac{-N_i}{\tau_{N_{ij}}} + \frac{N_j}{\tau_{N_{ji}}} \quad (12)$$

$$\left(\frac{\partial \vec{P}_i}{\partial t}\right)_c = \frac{-\vec{P}_i}{\tau_{p_i}} \quad (13)$$

$$\left(\frac{\partial W_i}{\partial t}\right)_c = -\frac{3}{2} \frac{N_i k T_i}{\tau_{\epsilon_{ij}}} + \frac{3}{2} \frac{N_j k T_j}{\tau_{\epsilon_{ji}}} \quad (14)$$

We illustrate a set of scattering curves for a Γ -X orientation in Fig. 2. The parameters used in the calculation are given in Table 1. These results should be compared to those of Bosch and Thim (Ref. 11). We retain the Γ -X orientation because most of the early space charge work involving the moment equations was performed for this ordering.

Recovery of the drift and diffusion equation requires the judicious neglect of select space and time derivatives. For the particle balance equation, conduction within a single parabolic band, and neglect of avalanching allows us to set $(\partial N / \partial t)_c = 0$. We then obtain current continuity

$$\frac{\partial N}{\partial t} + \nabla \cdot (\vec{v} N) = 0 \quad (15)$$

For the momentum term, we set $(\partial \vec{P}_i / \partial t)_c = -P_i / \tau_p$. Then, neglecting all spatial and temporal transients, i.e., the terms $\partial \vec{P}_i / \partial t$, and $\nabla \cdot (\vec{v}P)$, we obtain

$$N\vec{v} = \frac{\vec{P}}{m} = N \mu \vec{F} - \frac{\mu}{e} \nabla(NkT) \quad (16)$$

where $\mu = e\tau_p/m$. Using Einstein's relation, $D = \mu kT/e$, we obtain

$$N\vec{v} = -N \mu \vec{F} - \nabla (ND) \quad (17)$$

which, when coupled to the equation of continuity (Eq. (15)), yields the semiconductor equation (Eq. (2)). Based on the above approximations, it is clear that within the framework of the Boltzmann equation, we see that even in the simplest case the semiconductor equations must be used with caution.

The question as to just how serious the above approximations are, can be examined analytically. However, for highly nonlinear problems, a more useful approach is a numerical one. In perhaps the only serious comparison, Cheung and Hearn (Ref. 12), studied Gunn domain propagation using the semiconductor equations with that obtained using the balance equations (neglecting the temporal derivative in the momentum balance equation). Their results show dramatic differences and are displayed in Fig. 3.

While one may have many serious reservations about unbridled use of the semiconductor equations, its effectiveness for micron length and moderate frequency devices has been established by experience. It also has the significant advantage of familiarity. A balanced numerical physics program should involve continued use of the semiconductor equations, as well as the Boltzmann transport equation.

II.3 Studies Using the Drift and Diffusion Equation

In the past several years we have used the semiconductor equations to describe time-dependent transport in two and three terminal negative differential mobility devices. The two terminal work was concerned primarily with elucidating the operational physics of GaAs and InP X-band devices. Most of this work has been summarized in a monograph "The Gunn-Hilsum Effect" (Ref. III-1, see Section III*) and in a review article (Ref. III-2). The studies described in these reviews represent the nonlinear semiconductor as a one-dimensional entity.

* References preceded by the Roman numeral III have been wholly or partially supported by ONR Contract N00014-78-C-0269. They are listed in Section III.

Studies in 1980, in collaboration with the Solid State Device Technology Branch at the Naval Research Laboratory, required a broadening of this program. Here, using a well developed two-dimensional simulation, we sought design concepts to obtain repeatable coherent microwave transit time oscillations from coplanar InP two terminal devices (see Fig. 4). The basis of this study was the observation at NRL that repeatable and predictable oscillatory behavior from device to device had not been forthcoming. Our simulations revealed that some sort of significant drop in the background doping near the source contact may be required for repeatable and predictable oscillations from device to device.

The two-dimensional simulations used in the NRL study were developed earlier to examine the time-dependent behavior of GaAs FET's. Here our initial theoretical work predicted the presence of oscillations in these devices (Ref. 19). Subsequent work, in collaboration with workers at NRL and at Colorado State University, confirmed these predictions (Refs. III-3 and III-4). These results were presented at numerous meetings and at the NATO Advanced Study Institute on the Physics of Non-linear Transport in Semiconductors. The lecture notes have been published (Ref. III-5) and are part of a major review article to appear in 1981 (Ref. III-6). In addition, we have used the two-dimensional simulation to compare the switching properties of GaAs and silicon MESFETs. We find much higher switching speeds for GaAs at low bias levels, while at high bias levels, due to similar values of the saturated drift velocity, the switching speeds are comparable (Ref. III-7). There appears to be experimental confirmation of these results (Ref. 20).

We began an assessment of the role of the substrate. Part of this aspect of the study was closely related to the NRL collaboration. In one case, a two-terminal device whose channel height was sufficient to generate a high field recycling domain at a notched cathode was redesigned with a substrate. The substrate now occupied one-half of the active region and the oscillation ceased. This result is thought to relate to a critical 'thickness-doping product' criteria. In another case, a three terminal device with a channel height sufficient to sustain recycling high field domains was placed on a p-type substrate with varying doping levels. The bias level sufficient to generate an instability in the absence of a substrate was insufficient when the substrate was present.

II.4 Studies Using the Boltzmann Transport Equation

II.4.i Transient Overshoot

The second aspect of our program involves solving the Boltzmann transport equation to examine the short temporal and spatial transients of submicron device structures. At the beginning of this program, the primary focus was on evaluating the scattering integrals. In this evaluation, we avoided most of the approximations made by others and instead used the complete set of integrals listed by

Butcher (Ref. 18). The values of the scattering integrals for the set of parameters displayed in Table 1 has been briefly mentioned earlier and was shown in Fig. 2.

The next phase of the calculation involved computing the transient response of the carriers to a sudden change in field. This is the standard velocity overshoot calculation and was reviewed by the Principle Investigator at the NATO Advanced Study Institute (summarized in Ref. III-8). There are several features of overshoot. As discussed in an earlier paper (Ref. III-9), overshoot effects are consequences of differences in momentum and energy relaxation times. In multi-valley semiconductors, the overshoot contributions, therefore, appear in the momentum, as well as the mean velocity computations. We review this below for both the central and satellite valleys and for the situations where electrons starting with zero drift velocity are subjected to a sudden change in electric field. In the following, the subscripts "C" and "S" denote central and satellite valleys.

For the central valley and at low values of bias, the electron temperature is approximately equal to room temperature and the ordinary time dependent dynamic behavior occurs. At elevated bias levels, the electron temperature is substantially increased and the momentum relaxation time, due to strong intervalley coupling, decreases with increasing temperature (Fig. 2). Thus, we see overshoot, in that the final momentum is below the peak momentum (Fig. 5). (We point out that over moderate temperature increases LO phonon intravalley and ionized impurity scattering do not provide a momentum relaxation time that decreases with energy. Intervalley phonons are required. Indeed, for ionized impurity scattering, the relaxation time increases with energy.) During this same time interval, the increasing central valley temperature (Fig. 5b), results in electron transfer, and the momentum density, $N_C P_C$, shows an even greater overshoot (Fig. 5c).

The moment equations also contain a contribution from differential repopulation. This contribution enters as an effective temporal scattering term in the momentum equation

$$\frac{d \log N}{dt}$$

For the central valley, where at $t = 0$, $N_S \approx 0$, and $P_C = P_S = 0$, this term is approximately zero. However, when we consider the transient behavior of the satellite valley, the time derivative of $\log N_S$ is important because the change in the satellite population, relative to the original number present, is quite large. In addition, we note that the satellite valley momentum relaxation contribution is almost an order of magnitude larger than that of the central valley. Thus, in a time considerably shorter than that associated with the central valley, the satellite valley momentum reaches the value

$$P_s = -eF(t) \left[\frac{1}{\tau_{ps}} + \frac{d \log N_s}{dt} \right]^{-1} \quad (18)$$

where, since the satellite temperature remains close to room temperature for large changes in field, the scattering rates may often be taken as approximately constant. Combining both scattering contributions we see some "overshoot" due to differential repopulation, but none as dramatic as that associated with the central valley. Figure 6 illustrates. For part a, 1 corresponds to the increasing momentum prior to any significant electron transfer; 2 represents the scattering rate due to repopulation; 3 is the steady state value. In Fig. 6 we show the product of $N_s P_s / (N_c + N_s)$, where the effect of electron transfer is included. We see that as far as the contribution to velocity overshoot is concerned, the electron transfer tends to wipe it out.

The complete calculation requires that we obtain the drift velocity. For the calculations associated with Figs. 5 and 6, the drift velocity is shown in Fig. 7. Perhaps the most remarkable aspect of this result is the very large peak velocity prior to steady state (see, e.g., Ref. 3). This result has been one among many that have led some to suppose that narrow channel devices will yield higher carrier velocities. To a large extent, very high overshoot velocities are illusory as they are very sensitive to rise time. We illustrate this for a sequence of trapezoidal bias pulses, each with a varying rise time (see Fig. 8).

II.4.ii Bias Dependence of Overshoot

The first set of results is for a relatively slow rise time and the dynamic curves come very close to the steady state curves (see Fig. 9). A more significant departure from steady state occurs for the somewhat steeper rise time. In Fig. 10, we see some asymmetry in the time dependence of the central valley population and temperature, and an increase in the peak velocity. In the final sequence, we show results for a very short rise time. We see a dramatic increase in the peak velocity and clear asymmetry in the carrier dynamics (Fig. 11). Indeed, the final point of approximately zero-field and velocity is not an equilibrium state. Rather, we have a dramatic example of velocity undershoot. A longer time is needed for the electron temperature to approach equilibrium. There are strong implications here for upper frequency limits of device operation.

Perhaps the earliest attempt to examine the upper frequency limit for large signal oscillation was that of Butcher and Hearn (Ref. 1). Here, using a set of displaced Maxwellian electron distributions for each valley, the set of differential equations for the time dependent electron temperatures, drift velocities, and valley populations was solved for a dc bias field plus rf field.

II.4.iii Self-Excited Oscillations

From the point of view of a device physics, a driven oscillator probably lies somewhere between a small signal and a large signal self-excited oscillator. The self-excited oscillator is perhaps the most interesting of the three because it highlights the tenacious balance between electron transfer and sustained oscillators. It is extremely sensitive to contact, space charge and circuit conditions. We have been examining the upper frequency limit for self-excited oscillations for the device in a circuit with reactive elements. Figure 12 shows the oscillation. Here the current through the load resistor is displayed in part b; the dynamic voltage and I versus ϕ , obtained by eliminating time between current and device is shown in Fig. 12a. We also display the mean velocity (dynamic conduction current). The details of the oscillation are as follows:

As the field across the device increases and exceeds a threshold value transfer begins to occur. But since the field changes more rapidly than the electron temperature, more carriers are retained in the central valley, and with higher momenta, than steady state would dictate. This effect is responsible for the higher peak conduction current. But if the increasing electric field sustains high fields for a sufficient duration enough carriers will transfer to result in negative differential mobility (NDM). NDM of sufficient magnitude is required for sustained self-excited oscillations.

On the downswing the field again changes more rapidly than the electron temperature and more carriers are retained in the satellite valley - we achieve transient undershoot. Now while NDM is not necessary on the downswing (Ref. III-1) enough carriers must be returned to the high mobility valley for transfer on the upswing and NDM to occur. This means that the field must change slowly enough to allow a dump of carriers from the satellite to the central valley. If the field changes too rapidly too many carriers are retained in the satellite valley and NDM is too weak to sustain steady state oscillations. In Fig. 13, we plot the maximum frequency of self-excited oscillations as a function of dc bias.

We note the results in Figs. 5 through 13 are taken from Ref. III-6.

II.4.iv Length Dependence of Negative Differential Mobility Region

We have been discussing the upper frequency limit of transferred electron devices from the circuit viewpoint and the transfer and return of electrons between the central and subsidiary valleys. In this analysis we have not explicitly considered the following problem: When an electron enters the active region of a device, it will accelerate in the presence of an applied electric field. If the initial drift velocity of the carrier is low, is the transit length sufficient to cause electron transfer and negative differential mobility? The answer lies in earlier calculations. If the carrier experiences a sudden change in field, the

initial transient ($t \ll$ LO phonon scattering time) will be ballistic, followed by a region where v will approach $-e\tau F/m^*$ for a single valley. If the transit time is short enough to prevent significant transfer NDM will be weak, if at all. Figure 14 summarizes (Ref. III-10) where, for uniform fields, device length is a derived quantity. Here,

$$L = \int_0^T v(t) dt \quad (19)$$

where T is a transit time.

Now the velocity versus field curves and the velocity versus time curves of the type shown here provide an indication of why there is interest in submicron devices. The possibility exists for achieving very high velocities over very short distances. But again, a word of caution. The calculations of Fig. 14 are for carriers subjected to sudden changes in field. As we have seen, finite rise time dramatically reduce this peak, and so the results will be somewhat less important.

II.4.v Spatial Transients in Short Channel GaAs Devices

Velocity overshoot and other uniform field transient calculations are a very common feature of submicron device physics studies. Spatial transients, of the type discussed by Kroemer (Ref. 21), where rapid changes in field, as in a high field Gunn domain, can cause velocity overshoot transients has received less exposure. Spatial transient calculations are, however, likely to be essential for realistically determining the effectiveness of overshoot in improving the frequency response of, e.g., submicron field effect transistors. We have begun to examine some of these problems by solving the full spatially dependent one-dimensional Boltzmann transport equations (Eqs. (7) through (9)). We do this for a one-dimensional 5000 Å GaAs element with a donor distribution as shown in Fig. 15. The element is part of a resistive circuit which is biased at a finite rate. The carrier dynamics is examined at two instants of time. (Note: serious objections can be raised to use of "jellium" distributions. For any combination of increased donor density or size reduction will necessarily introduce effects due to the discrete nature of the donors. This is ignored below.)

As the bias is turned on, there is an increase in potential across the device, and a corresponding increase in current and field. The field is computed self-consistently and its slopes reflect any incomplete screening of inhomogeneities by the mobile carriers. For the device in the schematic configurations of Fig. 15, as the field in rising energy relaxation is incomplete and velocity overshoot contributions are dramatic (see Figs. 16 and 17). Here, velocity is computed from the equation

$$\langle v(x,t) \rangle = \frac{\frac{N_P}{m_c} + \frac{N_P}{m_s}}{N_T(x,t)} \quad (20)$$

In steady state the extent of the spatial transient will depend on the bias. In Figs. 18 and 19, the fields are high enough to accommodate almost complete transfer. Here, the carrier temperature is reduced, the energy relaxation rates are shorter, and there is virtually no overshoot. The results here are virtually the same as we would obtain using the steady state curves. The nonuniform field calculations are summarized in Ref. III-6.

III. RECENT PUBLICATIONS UNDER ONR CONTRACT N00014-78-C-0269

1. Shaw, M. P., Grubin, H. L. and Solomon, P. R.: The Gunn-Hilsum Effect, Academic Press, N.Y. (1979).
2. Shaw, M. P., Grubin, H. L. and Solomon, P. R.: Gunn-Hilsum Effect Electronics, Adv. Electronics and Elect. Phys. 51, 310, Academic Press, Inc., N.Y. (1980).
3. Grubin, H. L., Ferry, D. K. and Gleason, K. R.: Spontaneous Oscillations in Gallium Arsenide Field Effect Transistors, Solid State Electronics, 23, 157 (1980).
4. Grubin, H. L., Ferry, D. K. and Gleason, K. R.: Hot Electron Induced Oscillations in Gallium Arsenide Field Effect Transistors, Conference Record of the 3rd Biennial University/Industry/Government Microelectronics Symposium (1979).
5. Grubin, H. L.: Hot Electron Contributions in Two and Three Terminal Semiconductor Devices. In Physics of Nonlinear Transport in Semiconductors, Ed. by D. K. Ferry, J. R. Barker, and C. Jacoboni (Plenum, New York, 1980) 153.
6. Grubin, H. L., Ferry, D. K., Iafrate, G. J. and Barker, J. R.: The Numerical Physics of Micron-Length and Submicron-Length Semiconductor Devices, in Microstructure Science and Engineering VLSI, Ed. by N. Einspruch (Academic Press, N.Y., 1981).
7. Grubin, H. L.: Switching Characteristics of Nonlinear Field Effect Transistors: Gallium Arsenide versus Silicon, IEEE Trans. Microwave Th. and Tech., MTT-28 442 (1980).
8. Grubin, H. L.: Hot Electron Effects in Semiconductor Devices. In Physics of Nonlinear Transport in Semiconductors, Ed. by D. K. Ferry, J. R. Barker, and C. Jacoboni (Plenum Press, New York, 1980) 311.
9. Grubin, H. L., Ferry, D. K., Barker, J. R., Littlejohn, M. A., Glisson, T. H. and Hauser, J. R.: Transient Relaxation Effects in Transferred Electron Devices: Proc. 7th Biennial Cornell U. Electr. Eng. Conf. (1979).
10. Grubin, H. L., Ferry, D. K., Barker, J. R.: Transient Effects in Submicron Devices Load Line Dependence: Proc. 1979 IEDM (IEEE Press, N.Y.) 394, (1979).

H. L. Grubin
United Technologies Research Center

D. K. Ferry
Colorado State University

K. R. Gleason*
Naval Research Laboratory

I. INTRODUCTION

The operating principles of the field effect transistor were set down by Shockley in 1951. The device was a three-terminal device with one of its terminals connected to a pn junction (see Fig. 1a). The pn junction provided a region of local charge depletion whose width $W(x)$ could be varied by changing the bias on the gate contact. In this way the resistance to the flow of carriers from the source to the drain contact could be altered and current-voltage relations of the type shown in Fig. 1b resulted.

Since 1952, as new problems arose and a variety of different materials were used, FET behavior has required models increasingly more sophisticated than that proposed by Shockley. In general, however, as new models were proposed; their validity was soon called into question. For example, in Shockley's analysis, which was often applied to the material silicon, the mobility was assumed to be constant. While this was expected to be reasonably accurate for low bias levels it was also applied to those situations where the presence of high fields made the assumption inadequate. Modifications have since been made which include velocity saturation².

Along with velocity saturation comes the notion that carriers in the FET behave like a compressible fluid, bunching together and yielding local regions of high electric field³. When this occurs in other semiconductors such as gallium arsenide, dramatic effects may occur. In the case of gallium arsenide, while early interest was based on its high mobility; it was recognized, almost at the onset, that nonlinearities in the carrier velocity would have to be included. At the beginning, and for FETs, the carrier velocity was modelled with two sections, with the high-field section accounting for velocity saturation⁴. While this could predict some of the GaAs FET properties, it could not explain the current instabilities that were reported in

1966⁵ and 1968⁶. In 1976-79, the first papers to deal with these dynamic effects began to appear⁷⁻⁹. These calculations were more general than the earlier studies in that the nonlinearities in the velocity electric field relation included a region of negative differential mobility, as shown in Fig. 2a. Currently, the use of these curves, which represents steady state equilibrium situations for explaining the dynamic behavior of electrons, is being called into question¹⁰. In particular, its use for explaining highly doped submicron device behavior is being treated gingerly. The questions of where and when the equilibrium velocity electric field curve of Fig. 2a can be used is as yet unanswered. Meanwhile, we will discuss what it predicts. We will also summarize our experimental results with GaAs Schottky gate FETs which tend to confirm these predictions¹¹.

II. INSTABILITIES IN SCHOTTKY GATE GALLIUM ARSENIDE FIELD EFFECT TRANSISTORS

II.a Summary

The static and dynamic properties of a Schottky gate gallium arsenide field effect transistor are summarized in Fig. 2b. The bold curve in the figure is the equilibrium velocity electric field curve scaled to the current and voltage parameters. The current is in multiples of $N_0 v_p A$, where N_0 is the active region doping level, v_p the peak carrier velocity, and A the cross-section area in the direction of current flow. The voltage is in multiples of $E_p L$, where E_p is the field at peak velocity. With reference to Fig. 2b, we have found that whenever the drain current density $I \geq I_s$, the value associated with the saturated drift velocity of the carriers, an instability can occur. In two terminal device language, I_s is referred to as the sustaining current¹². Generally, because of the nonlinear distribution of potential under the gate contact very thin FETs sustain lower current density levels than thicker devices. This particular

Conference record of the 3rd Biennial University Industry/Government Microelectronics Symposium (1979).

feature has led to the following device classification scheme¹¹. We have classified devices as being members of one of two groups as determined by the ratio

$$K = \frac{\text{Gate voltage at cutoff}}{\text{Drain voltage at the onset of current saturation for zero gate voltage}}$$

Devices with K greater than unity sustain current oscillations, those with K approximately equal or less than unity are electrically stable. For those cases with K greater than unity, oscillations begin beyond the knee of current saturation (denoted by dashed line in Fig. 2b). Oscillations cease at high values of drain and gate bias (the solid lines in Fig. 2b). The instability is initiated when the average field under the gate contact reaches the NDM threshold value. (This result holds true at different temperatures.) An estimate of the carrier velocity in the channel between the gate and drain contacts indicates that just prior to the oscillation the electrons are usually drifting at speeds in excess of the high field saturation drift velocity. When the oscillation ceases with increased gate bias, the velocity drops to values significantly below the saturation drift velocity. The above conclusions emerge from numerical simulation and experiment.

II.b Numerical Results

The operation of the GaAs FET is critically dependent on the behavior of local regions of high electric field of 'domain'. And depending on device size and bias values, these domains are either trapped near the gate or drain contacts or propagate between them¹¹. The numerical simulation reveals the presence of two qualitatively different trapped and one traveling domain. The first trapped domain forms within the conducting channel and at the drain edge of the gate contact. Its formation is a direct consequence of velocity saturation, and its presence is responsible for current saturation at values of drain voltage significantly below that predicted by Shockley¹ (thus values of K greater than unity). The second trapped domain is qualitatively different and forms in FETS capable of sustaining current instabilities arising from negative differential mobility. This domain forms near the drain contact at high drain and low gate bias levels and is coincident with the cessation of oscillatory activity in GaAs FETs. The domain is qualitatively similar to the high anode field¹² configuration in two terminal devices, where it is responsible in many cases for cessation of oscillations. In the case of the traveling domain, it is launched at the drain side of the gate contact, propagates to the drain contact, and then recycles. The general properties of this

domain are qualitatively similar to that for two terminal devices; and when the current density is somewhat below I_s , all oscillatory activity ceases¹².

II.c Experimental Results

The oscillatory activity of the GaAs FETs was detected with spectrum analyzers and sampling oscilloscopes. Spectral analysis on one device showed oscillations at 6.5, 13, 23, 30, 36, and 40 GHz. Higher frequencies could not be detected. The oscillations were strongest near the instability threshold but ceased at high drain bias levels. At high drain and zero gate bias levels, white light was detected. An initial reduction in bias on the gate contact resulted in similar behavior, but all oscillatory activity ceased at sufficiently high gate bias levels, including the appearance of light. The appearance of light is compelling evidence for the presence of regions of high electric field domains. Others have also observed white light¹³ at high drain bias levels and attributed it to impact ionization within a domain trapped at the drain contact. The intensity of light was also observed to increase with drain bias and decrease with increased gate bias.

III. CONCLUSIONS

Based upon the results of our numerical and experimental study we have reason to conclude that our observations of oscillations in gallium arsenide field effect transistors arise from negative differential mobility contributions. Although the possibility exists that these oscillations are a consequence of feedback between the gate and drain loop, the critical parameters for the initiation and cessation of oscillations appear to be determined by the material properties of the device rather than the circuit. Of course the circuit and the device may determine the oscillation frequency much in the same way of circuit controlled oscillations occur in two terminal device; but in the study reported here the oscillation conditions are primarily materials dependent. The details of our result appear elsewhere¹¹.

IV. ACKNOWLEDGMENT

This work was partially supported by the Office of Naval Research (HLG) and the Army Research Office (DKF).

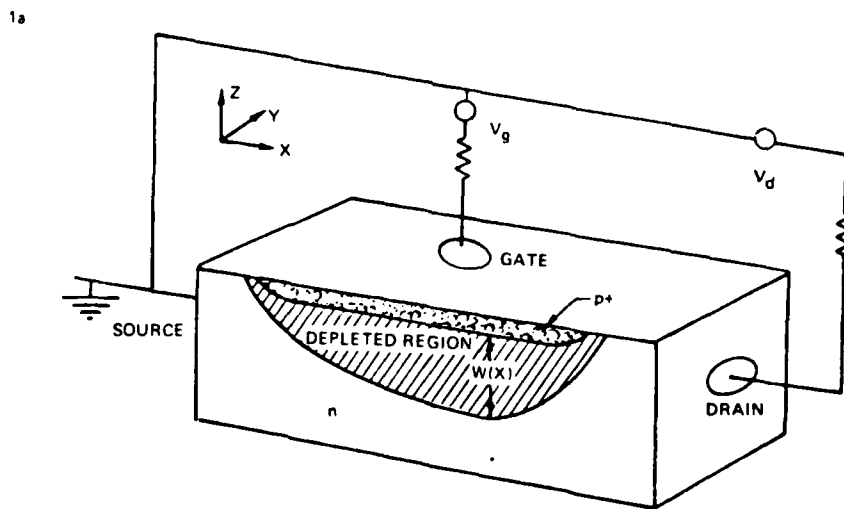
REFERENCES

1. Shockley, W.: Proc. IRE. 40, p. 1365, 1952.

REFERENCES (Cont'd)

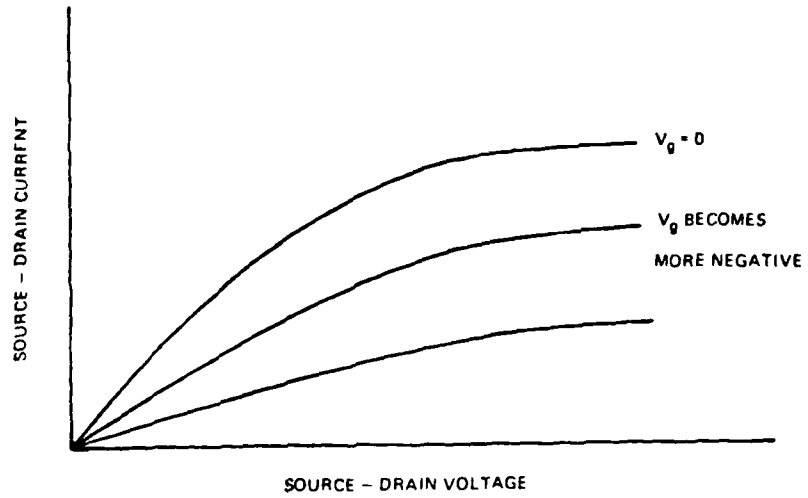
2. Dacey, G. C. and I. M. Ross: Bell System Tech J. 34, p. 1149, 1955.
3. Kennedy, D. P. and R. R. O'Brien. IBM J. Research Develop. 14, p. 95, 1970.
4. Turner, J. A. and B. L. H. Wilson. Proc. 1968 GaAs Symposium, Institute of Physics, (London) Conf. Series No. 7, p. 195, 1969.
5. Winteler, H. R. and A. Steinmann: Proc. Int. Symp. GaAs 1966, Inst. of Phys. (London) Conf. Ser. No. 3, p. 228, 1967.
6. Zuleg, R. Proc. Int. Symp. GaAs, Inst. of Phys., (London) Conf. Ser. No. 7, p. 181, 1969.
7. Yamaguchi, K. A. Asai, and H. Kodera: IEEE Trans. Electron Devices, ED-23, p. 1283, 1976.
8. Grubin, H. L. and T. M. McHugh: Proc. Sixth Biennial Cornell Elect. Engineering Conf., Cornell Univ., Ithaca, p. 409, 1977.
9. Grubin, H. L. and T. M. McHugh: Solid St. Electron., 21, p. 69, 1978.
10. J. Ruch: IEEE Trans Electron Devices, ED-9, p. 652, 1972.
11. For details see H. L. Grubin, D. K. Ferry, and K. R. Gleason, Solid State Electrons, (to be published 1979).
12. Shaw, M. P., H. L. Grubin, and P. R. Solomon: The Gunn-Hilsum Effect, Academic press, New York, 1979.
13. T. Mimura, H. Suzuki, and M. Fukuta: Proc. IEEE, 65, p. 1407, 1977.

*Present Address: Textronix, Inc.
Beaverton, Oregon



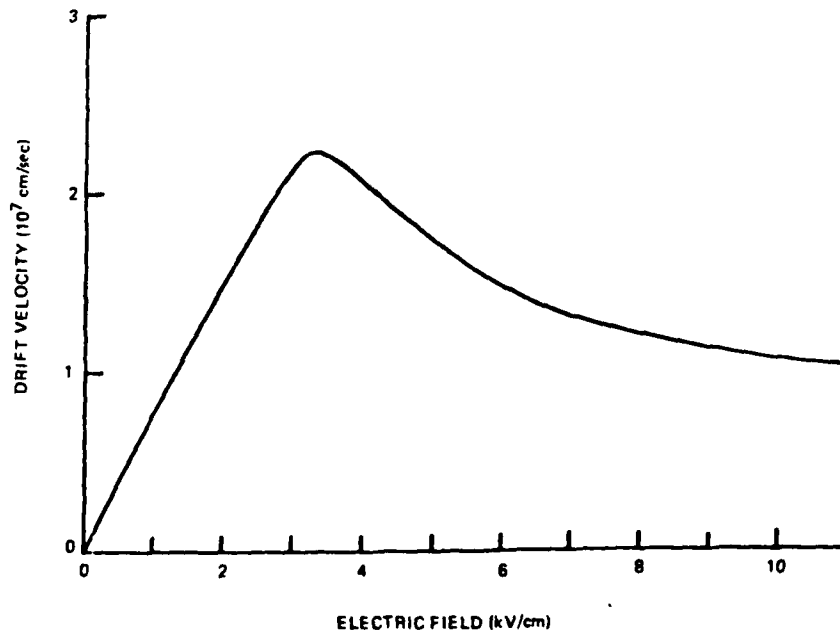
1a. Schematic representation of a junction field effect transistor

1b



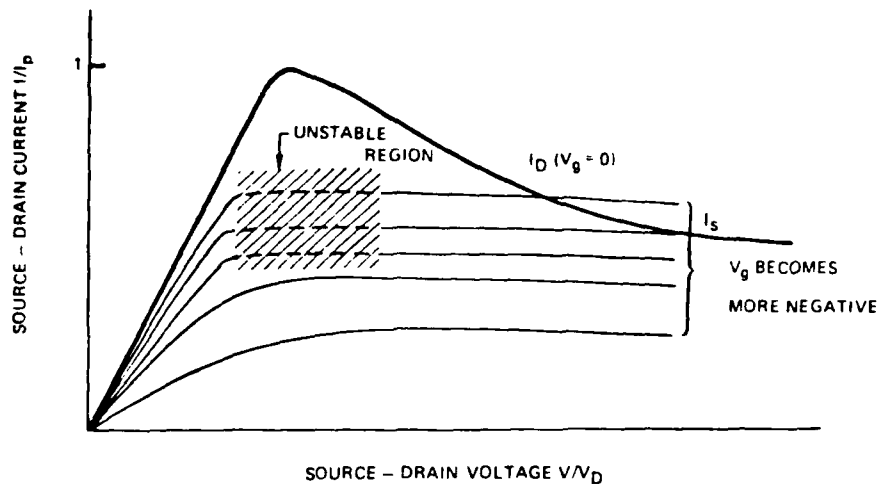
1b. Expected source drain characteristics of a junction field effect transistor

2a



2a. Drift velocity versus electric field for a semiconductor with a region of negative differential mobility

2b



- 2b. Expected current voltage characteristics for a negative differential mobility semiconductor. Stable regions are denoted by solid curves, unstable regions by dashed curves. Instabilities require $I_D \gtrsim I_S$. Devices where $I_D(V_g=0) < I_S$ will be electrically stable.

Transient Relaxation Effects in Transferred Electron Devices

H. L. Grubin

United Technologies Research Center, East Hartford, Connecticut

D. K. Ferry

Colorado State University, Fort Collins, Colorado

J. R. Barker

University of Warwick, Coventry, England

M. A. Littlejohn, T. H. Glisson and J. K. Hauser

North Carolina State University, Raleigh, North Carolina

I. INTRODUCTION

As devices are made smaller and doping levels increased, transient relaxation effects begin to dominate the behavior of transferred electron devices. One area that has received most attention is that of velocity overshoot in the central valley, an effect due mainly to differences in the energy and momentum scattering times (Ref. 1). There are, however, at least two other relaxation effects of interest. The first is important mainly in the satellite valley and is a direct consequence of its short momentum scattering time. The second is a consequence of the fact that scattering between two different quantum states takes place over a finite duration of time (Ref. 2). In the discussion that follows we will review overshoot contributions within the central valley and then discuss the remaining transient effects. Our results are presented within the framework of solutions to the moments of the Boltzmann transport equation, although many of the results have also been obtained using Monte Carlo methods. In these calculations we have also included a resistive circuit. Its consequences will be briefly discussed.

In an actual device the electric field will be a function of space and time. The present calculations assumes, however, a spatially uniform electric field between cathode and anode of a two terminal device. The electrons are assumed to enter the device with a zero drift velocity. The response of the average electron to a step change in bias is then obtained by simultaneously solving the external circuit equation with the zeroth, first and second moments of the Boltzmann transport equation assuming that the electron distribution may be approximated by a shifted Maxwell-Boltzmann distribution function (Ref. 3). The zeroth moment yields the equation of continuity, and the first moment yields Newton's law of motion for momentum density:

$$\frac{dP}{dt} + P \left[R_p + \frac{d \log N}{dt} \right] = -eI \quad (1)$$

Transient Relaxation Effects in Transferred Electron Devices

H. L. Grubin

United Technologies Research Center, East Hartford, Connecticut

D. K. Ferry

Colorado State University, Fort Collins, Colorado

J. R. Barker

University of Warwick, Coventry, England

M. A. Littlejohn, T. H. Glisson and J. R. Hauser
North Carolina State University, Raleigh, North Carolina

Presented at the 7th Biennial Cornell University
Electrical Engineering Conference 14-16 August 1979

In equation (1) R_p denotes the momentum scattering rate; its units are 1/sec. The second moment equation describes energy balance and its time dependence is governed by its scattering rates. Indeed, the important transient relaxation effects arise because the momentum scattering rate is an explicit function of electron temperature, and because for materials like GaAs, the time rate of change of momentum and energy, which are governed by their scattering rates, are different. Typical central valley momentum and energy scattering rates for Γ -X ordering are shown in figure 1a (see also Ref. 3)

II. CENTRAL VALLEY RELAXATION

Central valley overshoot can be understood by examining solutions to equation (1). For the case of a constant, temperature independent momentum scattering time, the solution to this equation subject to $P(t=0)=0$ is (ignoring $d \log h / dt$):

$$P(t) = -eR_p^{-1}F \left[1 - \exp -R_p t \right] \quad (2)$$

and the time dependence is similar to that shown in figure 2a, which was calculated exactly. For the calculation of figure 2a the bias was sufficiently low so that only a marginal increase in the central valley electron temperature occurs. For sufficiently high values of bias the electron temperature reaches a high enough value to cause a sizeable increase in the scattering rate. The result is that shown in figure 2b. If we examine the structure of the central valley momentum, we find that although the electron temperature is increasing the initial momentum transient is governed primarily by the momentum balance equations (1) and whatever resistance is in the external circuit. If the latter can be ignored, then for an average scattering rate of 3.5×10^{12} /sec over a temperature range of 300 to 1000°K, P_c will be within 75% of its peak value $-eF/R_p$ after a time duration of approximately 0.4ps. The central valley electron temperature, which has also been increasing (figure 2c) over this time period, continues to increase. And its increase, which is governed mainly by the external circuit parameters and the energy relaxation time, governs the successive increase in the momentum scattering rate and the decrease in the steady state value of the central valley momentum (see figure 2b).

The overshoot displayed in figure 2b is that associated with a single carrier. This is not the quantity usually discussed when velocity overshoot is considered. Rather, the average drift velocity

$$V = \frac{N_c P_c / m_c^* + N_s P_s / m_s^*}{N_c + N_s} \quad (3)$$

where P_s is the satellite valley momentum; m_c^* , m_s^* , N_c and N_s are respectively, the central and satellite valley effective masses and net carrier densities. In figure 2d we display the quantity

$$N_c P_c / (N_c + N_s)$$

versus time. We also superimpose the curves of figures 2b and 2c for reference. We note that the overshoot is considerably enhanced by electron transfer. Also note that the relaxation of the central valley drift velocity closely follows the relaxation of the electron temperature. This result holds true even for different resistive contributions and suggests that the relaxation to steady state in an actual device/circuit configuration will be governed by both energy relaxation and the external circuit.

III. SATELLITE VALLEY RELAXATION

In the above discussion we have ignored the quantity

$$\frac{d \log N}{dt}$$

appearing in equation 1. For the discussion so far, in particular, that associated with figure 1 where at $t = 0$, $N_s \approx 0$, and $P_c = P_s = 0$, this is approximately true. However when we consider the transient behavior of the satellite valley, the time derivative of $\log N_s$ is significant.

To examine the transient behavior of the satellite valley we first estimate the extent to which the satellite temperature exceeds room temperature. Typically, according to the results of reference 4, the satellite temperature is approximately equal to its room temperature value for fields below 40 kv/cm. Over this same temperature range the central valley temperature can exceed 2000°K. The origin of this difference lies in the scattering rates for the central and satellite valleys which we show below.

In steady state the energy balance equation yields (ref. 3)

$$0 = -N_c F P_c / m_c^* - N_c k_B T_c R(5) + N_s' T_s R(6) \quad (4)$$

$$0 = -N_s' F P_s / m_s^* - N_s' k_B T_s R(7) + N_c T_c R(8) \quad (5)$$

for the central and satellite valleys respectively. The prime on N_s denotes that N_s' is the density of only one of the satellite valleys. The numbers on the scattering rates refer to the central and satellite valley rates of figure 2. Using the steady state values of momentum and equations (4) and (5) we find the following relation for the central and satellite temperatures:

$$\frac{N_s' T_s}{N_c T_c} = \frac{\kappa(3)\kappa(5) + (m_s^*/m_c^*)R(4)\kappa(6)}{\kappa(3)\kappa(6) + (m_s^*/m_c^*)R(4)\kappa(7)} \quad (6)$$

where $\kappa(3)$, $\kappa(5)$ and $R(6)$ are central valley scattering rates. The others are satellite valley rates. As an example of the relative values of T_c and T_s we consider the time rate of change of carriers in the central valley:

$$\frac{dN_c}{dt} = -N_c \kappa(1) + N_s' R(2) \quad (7)$$

From figure 1d we see that the satellite valley scattering rates are relatively insensitive to temperature while the central valley scattering rates are temperature sensitive. We can estimate that in steady state $N_s \approx N_s'$ would occur with a central valley electron temperature of approximately 1500°K. The corresponding value of T_s as obtained from equation (6) is slightly larger than 300°K. The implication of this is that satellite valley momentum overshoot is not sensitively dependent on the satellite valley temperature.

As mentioned above, in examining the transient behavior of the central valley we have ignored contributions from the time derivative of $\log N_c$. From equations (1) and (7) we see that the net scattering rate is

$$R(3) - R(1) + R(2)N_s'/N_c.$$

For the initial transient where $N_s' < N_c$, and from the results of figure 2 we see that the dominant scattering contribution is from $R(3)$. The situation is considerably different when we consider the satellite valley. For this case, with 3 satellite valleys, as for Γ -X ordering the net momentum scattering rate is

$$R(4) + R(1)N_c/(3N_s') - R(2)/3$$

Now prior to intervalley transfer the sum of the last two terms is zero. But at elevated central valley temperature $R(1)$ increases rapidly with electron temperature. This coupled with the fact that at the initial stages of electron transfer the ratio of $N_c/3N_s'$ is large will lead to the result that the onset of transfer will significantly increase the satellite valley scattering rate.

In addition to the importance of the term $d \log N_s / dt$, we also note that the satellite valley momentum relaxation contribution $R(4)$ is almost an order of magnitude large than that of the central valley. Thus in a time considerably shorter than that associated with the central valley we expect the satellite valley momentum to reach its steady state value

$$P_s = -eF(t) \left[R(4) + \frac{d \log N_s}{dt} \right]^{-1} \quad (8)$$

where we can take $k(4)$ to be constant and equal to its room temperature value. $F(t)$ will continue to change in a manner determined by the external circuit and the central valley relaxation. Thus we expect that P will reach a maximum value given approximately by $-eF(t)/k(4)$ and then decrease as the contribution from $d\log N_s/dt$ enters. In steady state the final value of P_s will be given, again by $eF/R(4)$. This result is shown in figure 3a. In figure 3a, (1) corresponds to the increasing momentum prior to any significant electron transfer; (2) represents the scattering rate due to repopulation; (3) is the steady state value. In figure 3b we show the product of $N_s' P_s / (N_c + 3N_s')$. We see that as far as the contribution to velocity overshoot is concerned the electron transfer tends to wipe it out.

IV. FINITE QUANTUM TRANSITION TIMES

Most electron device calculations in which scattering events are accounted for are based upon the assumption that the transitions between two states within a particular valley, or between state within different valleys takes place during a zero time duration. This is an approximation; the transition can take place over a finite time duration and this time duration may be comparable to the transient response time. Ferry and Barker (Ref. 2) have suggested an approximation to account for these finite collision events. This is to replace the scattering rates 'R', which are implicit functions of time by the following expression

$$R(t) \Rightarrow \frac{1}{\tau_c} \int_0^t \exp(-t'/\tau_c) R(t - t') dt' \quad (9)$$

Thus the instantaneous scattering rate is averaged over an effective collision duration τ_c weighted by the function $\exp(-t/\tau_c)$. If as in the case of low fields $k(t)$ does not change much during a collision duration, the normal result is obtained. However, in a large field, where finite quantum transition times are important the weighting is necessary. These effects will also be important in high frequency transport where the collision duration becomes comparable to the relaxation times and the period of the wave.

The effect of including finite quantum transition times is illustrated in figure 4 where we show the transient response for a steady uniform field of 5kv/cm and 25kv/cm. The dashed lines are obtained for the case of instantaneous transition times. We see that in both cases the response for finite transition times is the faster one (Ref. 2). We note that results displayed in figure 4 were obtained for a two band Γ -L ordering, within the framework of the shifted Maxwellian distribution.

V. CONCLUSIONS

The purpose of the study was to highlight several new features associated with the transient behavior of electrons in GaAs. Particular emphasis was on overshoot in the satellite valley where its origin was due primarily to the onset of electron transfer. A similar type of overshoot may be expected to be associated with the central valley at very high bias levels. In the latter case the central valley is almost depleted of free carriers and a decrease in bias will result in a transfer of carriers from the satellite to central valley with resulting repopulation overshoot effects. In addition we also discussed the consequences of finite quantum transition times on the transient behavior of carriers in GaAs. Noting that these times may be comparable to the scattering times or the period of a high frequency signal, the effect of these finite times on the response of the carriers was computed. It was shown that the effect of a finite transition time is to increase the scattering rates and hence reduce the response times of the carriers.

VI. ACKNOWLEDGEMENTS

This study was supported by the Office of Naval Research and the Army Research Office, to whom we are grateful.

VII. REFERENCES

1. J. G. Ruch, IEEE Trans. Electron Devices, ED-19, 652 (1972).
2. D. K. Ferry and J. R. Barker, Solid State Electronics (in press).
3. R. Bosch and H. W. Thim, IEEE Trans. Electron Devices, ED-21, 16 (1974).
4. I. B. Bott and W. Fawcett, Adv. in Microwaves 3, 223 (1968).

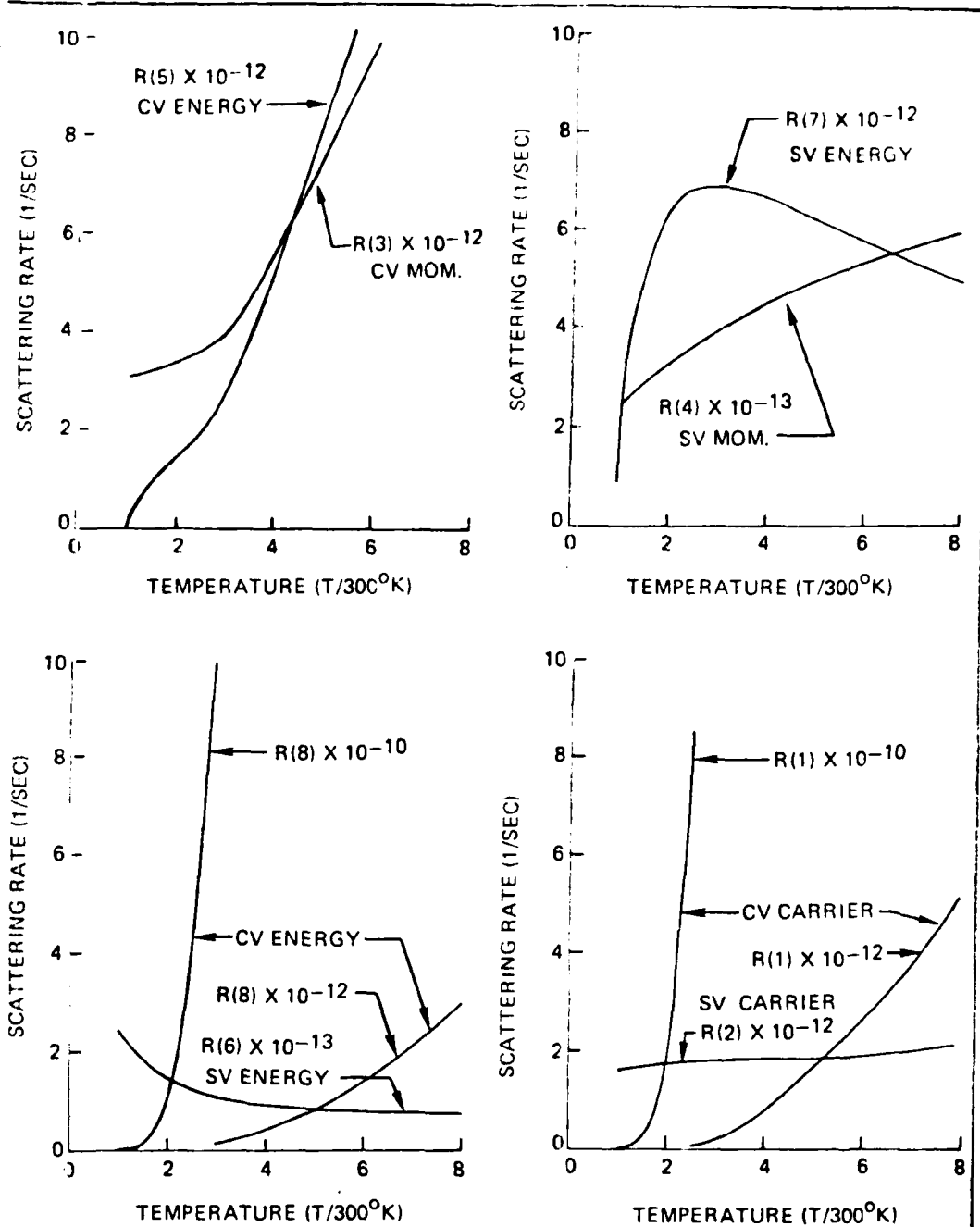


Figure 1. For GaAs, calculated zero drift energy scattering rates versus electron temperature. Parameters are the same as that of reference 3 except $m_s^* = 0.4m_0$. Scattering processes involved are: R(1), CV to all SV; R(2) and R(6), all SV to CV; R(3) and R(5), intravalley CV plus CV to all SV; R(4) and R(7), intravalley SV plus SV to CV and remaining SV; R(8), CV to one SV.

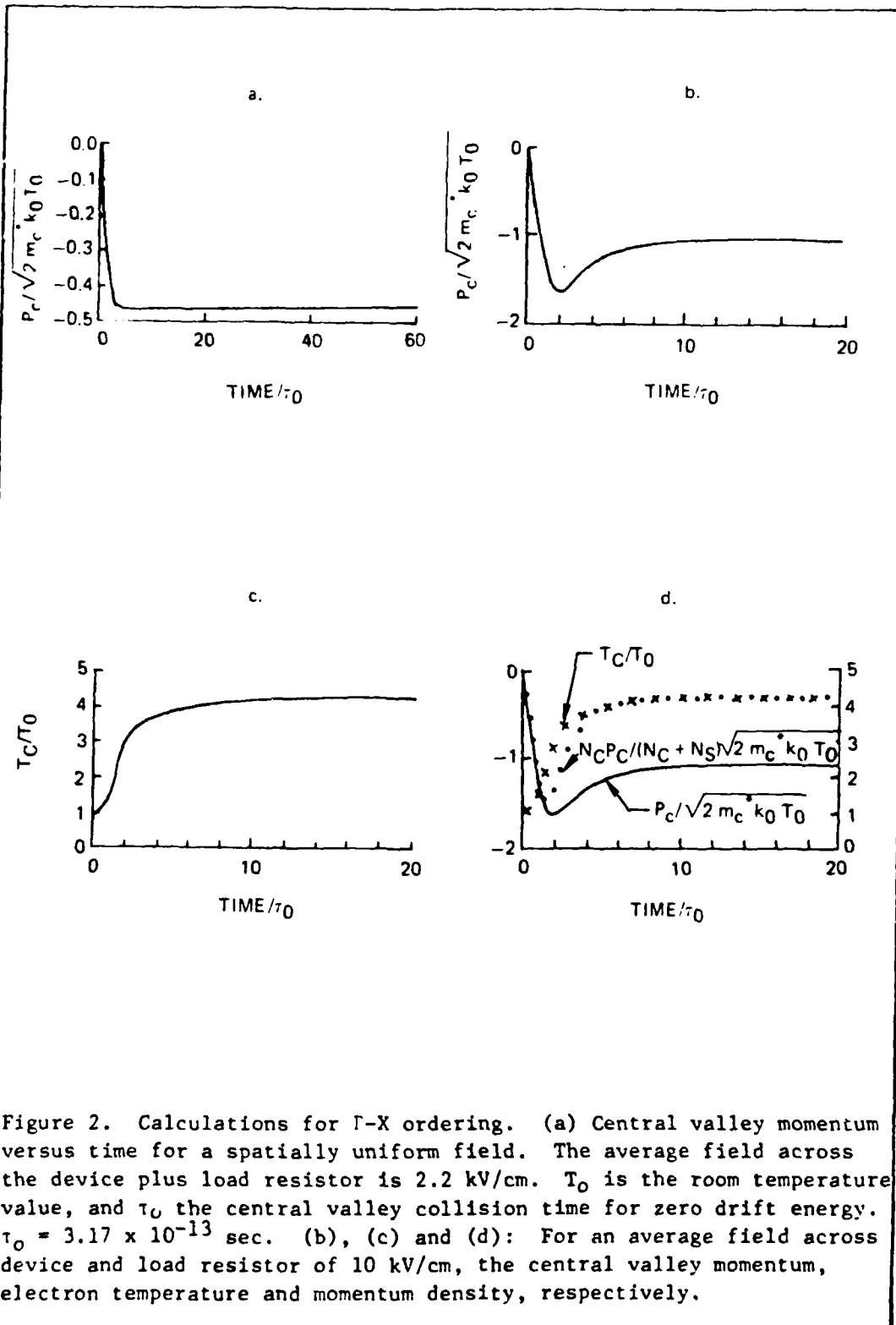


Figure 2. Calculations for Γ -X ordering. (a) Central valley momentum versus time for a spatially uniform field. The average field across the device plus load resistor is 2.2 kV/cm. T_0 is the room temperature value, and τ_0 the central valley collision time for zero drift energy. $\tau_0 = 3.17 \times 10^{-13}$ sec. (b), (c) and (d): For an average field across device and load resistor of 10 kV/cm, the central valley momentum, electron temperature and momentum density, respectively.

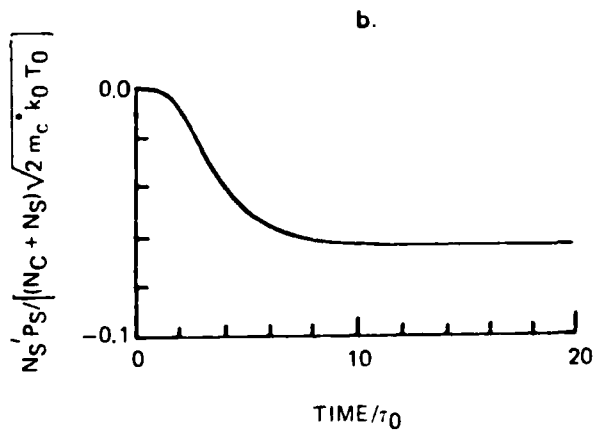
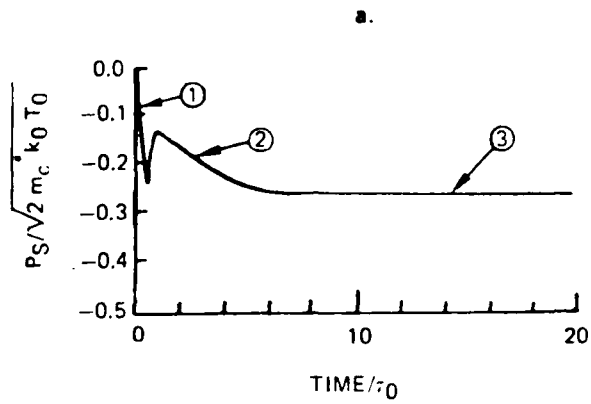


Figure 3. As in figures 2 (b) + (d). Figure 3a shows satellite valley momentum versus time. Figure 3b shows satellite valley momentum density versus time.

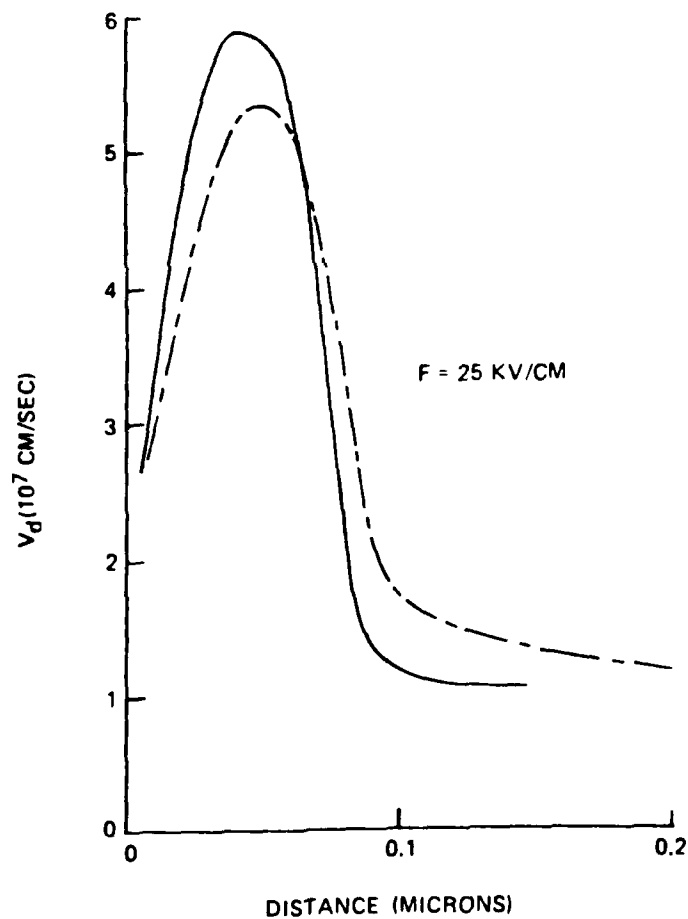
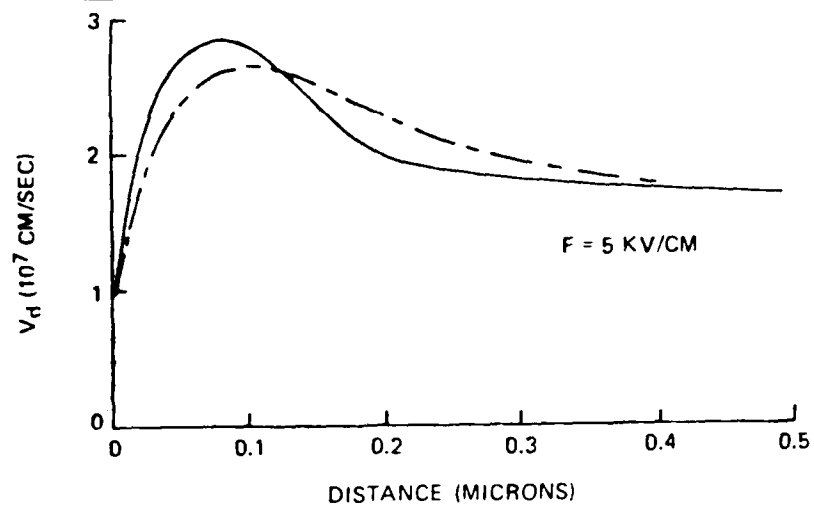


Figure 4. Transient drift velocity versus distance for GaAs in the Γ -L ordering. No external circuit was used for this calculation. Solid lines represent finite transition times. Dashed lines are for zero transition times. From reference 2, with permission.

Reprinted from:

PHYSICS OF NONLINEAR TRANSPORT IN SEMICONDUCTORS (1980)
Edited by David K. Ferry, J.R. Barker, and C. Jacoboni
Book available from: Plenum Publishing Corporation
227 West 17th Street, New York, N.Y. 10011

HOT ELECTRON CONTRIBUTIONS IN TWO AND THREE TERMINAL SEMICONDUCTOR
DEVICES

H. L. Grubin

United Technologies Research Center
East Hartford, Connecticut 06108

INTRODUCTION

In the previous discussion (Grubin, 1977) we concentrated on transient hot electron effects in semiconductor devices. We noted that these effects may be dominant for spatial dimensions of the order of the carrier mean free path and for doping levels common to currently fabricated field effect transistors. Perhaps one of the most significant consequences of these relaxation effects is that they will ultimately serve to eliminate the presence of negative differential mobility from such semiconductors as gallium arsenide and indium phosphide. Thus, there are at least two questions that we must consider: (1) Under what conditions will a semiconductor device possess a region of negative differential mobility, and (2) if it does possess this region, what are its consequences? We will examine these questions in reverse order.

In discussing the consequences of negative differential mobility (NDM) we are at that point in time where most of our device pictures are derived from models in which the equilibrium velocity electric field relation is taken to represent carrier drift in nonequilibrium situations. While the discussion of transient effects points to severe limitations with this model at extremes of size and doping levels, dynamic effects associated with such things as intervally scattering times will limit its usefulness to frequencies at and below the low millimeter-wave scale. Further, the equilibrium velocity electric field curve is dependent on impurity densities and so may vary from one region of the device to another. With these qualifications, it is clear that equilibrium velocity electric field models cannot be used confidentially for providing quantitative

determination of device behavior. Rather, we may expect that in those devices whose dynamic-relaxation contributions still allow a region of NDM to be present, such equilibrium velocity electric field models will provide the information necessary to present qualitative explanations of the oscillatory characteristics of NDM semiconductor devices. Indeed this is the very least we can expect of the equilibrium models; and as we will see, they have served us well.

In discussing NDM semiconductor device behavior through the equilibrium velocity electric field model we are going to concentrate on: (1) the role of the low resistance contacts on the oscillatory properties of the NDM device, and (2) the influence of the external circuit. We will first examine the two-terminal device, then move to the three-terminal device.

TWO-TERMINAL DEVICES

To highlight the importance of the cathode or anode region properties on the oscillatory behavior of two terminal NDM devices, we point out that while at the early stages of device development most devices were fabricated with ostensibly similar cathode and anode region contacts, it was the usual case to find that the current voltage characteristics of the device were not symmetrical with respect to the polarity of the applied bias (Shaw *et al.*, 1969). The importance of the circuit emerges when we realize that all current oscillations in NDM devices are not characterized by isolated propagating domains whose transit time determines the oscillation frequency of the device (Gunn, 1964). In some cases, the oscillation frequency bears no resemblance to the transit time of the carriers (Thim, 1968).

With regard to the low-resistance contact to materials such as gallium arsenide and indium phosphide, there appears to be general agreement that these contacts are highly nonlinear and have a non-negligible effect on device behavior at all except the lowest bias levels. There is not, however, any theory that self-consistently determines the properties of these contacts from first principles and then relates these properties to device behavior. Rather, there are a variety of phenomenological models. In our case, we have adopted the point of view that the alloyed metal/semiconductor contact imitates the properties of the unalloyed metal/semiconductor contact. The important distinction between these being that the alloyed contact has a substantially lower barrier height than the unalloyed contact. In analyzing the role of the contacts to the NDM device, we conceptually divide the device into three sections, as shown in Fig. 1.

The center region in Fig. 1 represents the NDM semiconductor. It is characterized by an equilibrium velocity electric field relation $v(E)$ and an equilibrium diffusion electric field relation $D(E)$. The time-

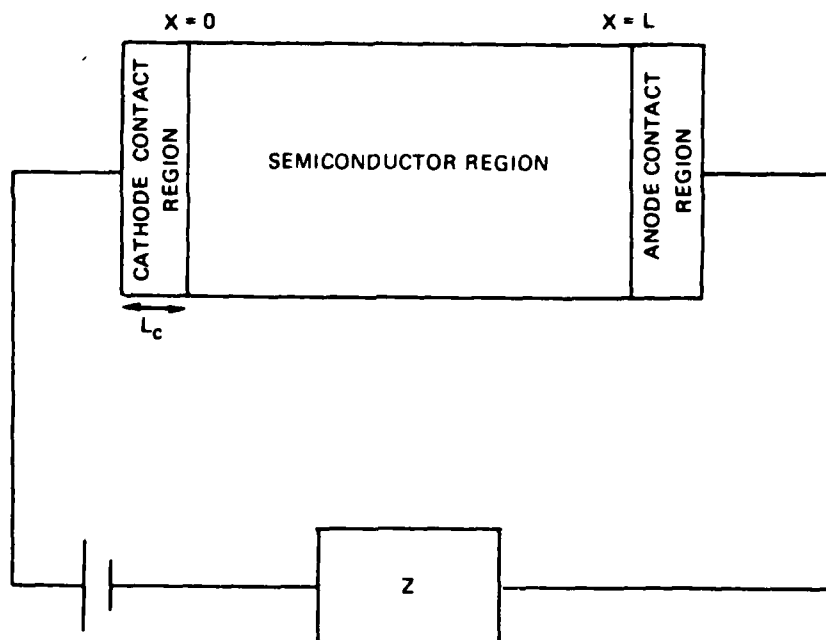


Fig. 1. Device - circuit configuration.

dependent dynamics of the carriers are obtained by solving the semiconductor equations, which for one dimension reduce to that shown below, for the total current density through the NDM semiconductor (see, e.g., Shaw *et al.*, 1979),

$$j_0(t) = v(E) \left[eN_0(x) + \epsilon \frac{\partial E(x,t)}{\partial x} \right] -$$

$$-D(E) \left[e \frac{\partial^2 E(x,t)}{\partial x^2} + e \frac{\partial N_0(x)}{\partial x} \right] + \epsilon \frac{\partial E(x,t)}{\partial t} . \quad (1)$$

The above equation deals with only one carrier specie, whose charge we take conveniently as the magnitude of the electron charge. Here, ϵ is the permittivity of the semiconductor, $N_0(x)$ is the background doping density, which may be spatially dependent, and $E(x,t)$ is the electric field.

The carrier dynamics in the cathode contact region are taken to be governed by the differential equation (Grubin, 1976a)

$$j_0(t) = j_c(E_c) + \lambda \epsilon E_c / dt, \quad (2)$$

where $j_c(E_c)$ represents the cathode conduction current density and has the same general properties as the 'control characteristic' discussed by Kroemer (1968). E_c is the electric field at the boundary between the cathode region and the semiconductor region. Depending on the contact, it may assume very high values as well as values near zero. λ is a dimensionless parameter. As indicated in Fig. 1, we assume that the cathode region, as represented by (2), separates the NDM semiconductor from the cathode proper. The rationale for this separation lies in experiments which indicate that for contacts with high cathode fields, the transition to the high field values may take place outside the NDM semiconductor. The cathode contact region is also taken to be electrically neutral and, for the cases considered below, to have a permittivity equal to that of the NDM semiconductor (i.e., $\lambda = 1$). E_c is assumed to be continuous across the interface between the NDM and separating elements.

As indicated above, the principle assumption we make about the alloyed contact is that it imitates the properties of the unalloyed metal/semiconductor contact. As used here, this implies that

$$j_c(E_c) = -j_r \{ \exp(-eV_c/nkT) - \exp[-(n^{-1} - 1)eV_c/kT] \}, \quad (3)$$

with $V_c = E_c L_c$. The form of (3) was adapted from studies of the unalloyed metal/semiconductor contact (Rideout, 1975). Its use here presumes a similar description. For the unalloyed contact, 'n' is the 'ideality' factor and describes the contact as dominated by thermionic emission ($n \approx 1$) or by tunneling ($n \gg 1$); j_r is the reverse current flux and may be related to the barrier height through the Richardson-Dushman equation

$$j_r = m^* A T^2 \exp[-(B/kT)] \quad , \quad (4)$$

where B is the barrier height (in eV), A is the Richardson-Dushman constant ($= 120 \text{ A/cm}^2/\text{k}^2$), and T is the absolute temperature. m^* is the ratio of an appropriate effective mass to that of the free electron mass. The results depend significantly on the value of j_r which we translate into values for B . For this we have arbitrarily assigned a value of 0.072 to m^* as representative of the central valley of CaAs. The relation between j_r and B is displayed in Table 1, where $j_p = N_0 e v_p$, with v_p being the peak drift velocity of the carriers as obtained from the equilibrium velocity electric field relation. Typical barrier heights for our discussion are about 0.2 eV. The

TABLE 1
BARRIER HEIGHT

$$-B = kT \log_e(j_r/m \cdot AT^2)$$

j_r/j_p	B
1.00	0.14
.80	0.15
.40	0.16
.20	0.18
.10	0.20
.05	0.22

parameter L_c , associated with (3), is specific to the formulation we use and does not appear in the formulation for metal/semiconductor contacts. While the parameter L_c is conceptually ambiguous, we regard it as representing the width of the alloyed region; n and j_r are thought of as more representative of the properties of the metal/semiconductor interface.

Figure 2 displays the dependence of the form of $j_c(E_c)$ on the choice of parameters. Note that significantly different parameters can yield similar $j_c(E_c)$ curves. We have also included for reference the neutral current density curve $j_c(E) = N_0 e v(E)$ which scales the velocity electric field curve for gallium arsenide. The significance of these curves for the space charge distribution within the NDM semiconductor device is considered below for steady-state time independent conditions. For this situation, we return to the total current density equation and examine it for zero diffusion and for constant doping density. At the cathode boundary,

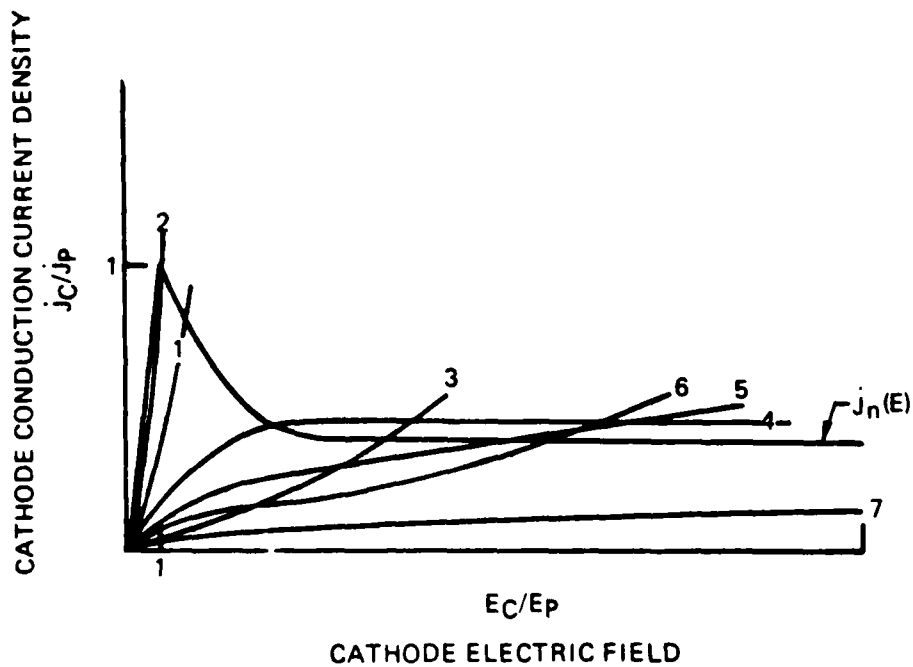
$$\frac{\partial E}{\partial x} = \frac{j_c(E_c) - j_n(E_c)}{\epsilon v(E_c)} \quad (5)$$

whereas within the bulk of the semiconductor, away from either the cathode or anode regions

$$E \approx j / N_0 e \mu_0 \quad , \quad (6)$$

where μ_0 is the low field mobility of the semiconductor.

In Fig. 3, we sketch the electric field profile for $x \geq 0$ for the situation where the cathode conduction current density curve intersects the neutral current density curve at a point somewhere below the threshold field for negative differential mobility. For successively higher current density values, by virtue of current continuity, the intersections of the vertical line $j = j_1$ with j_c and j_n determines, respectively, the cathode field E_{c1} and the bulk field E_{b1} . The value of j_n at E_{c1} exceeds j_c at this point, and there is a partially depleted region of charge adjacent to the cathode region boundary. Increasing the current density to the value j_2 , where j_c and j_n intersect, yields a situation of uniform fields throughout the cathode plus semiconductor region. For the situation where the current density is increased to j_3 , the field at the cathode is less than the field in the bulk, j_n is less than j_c and we have a region of charge accumulation adjacent to the cathode contact region boundary. A current instability may be expected to occur when the field away from the cathode region enters the region of negative differential mobility.



CURVE	J_r/J_p	n	$L_c \times 10^5$
1	0.1	10	1.5
2	0.1	10	3.0
3	0.1	10	0.2
4	0.4	1.0	1.0
5	0.2	1.05	1.0
6	0.1	1.1	1.0
7	0.1	1.1	0.2

Fig. 2. Cathode conduction current density versus electric field for seven of parameters, n , j_r and L_c . Also shown is the neutral conduction current density curve for gallium arsenide, denoted by $J_n(E)$. From Shaw et al. (1979).

The next situation to consider is that shown in Fig. 4, where the cathode current density curve intersects the neutral curve in the region of negative differential mobility. At the current density j_1 , we have as in the previous case, a region of charge depletion occurs adjacent to the cathode region boundary. Increasing the current

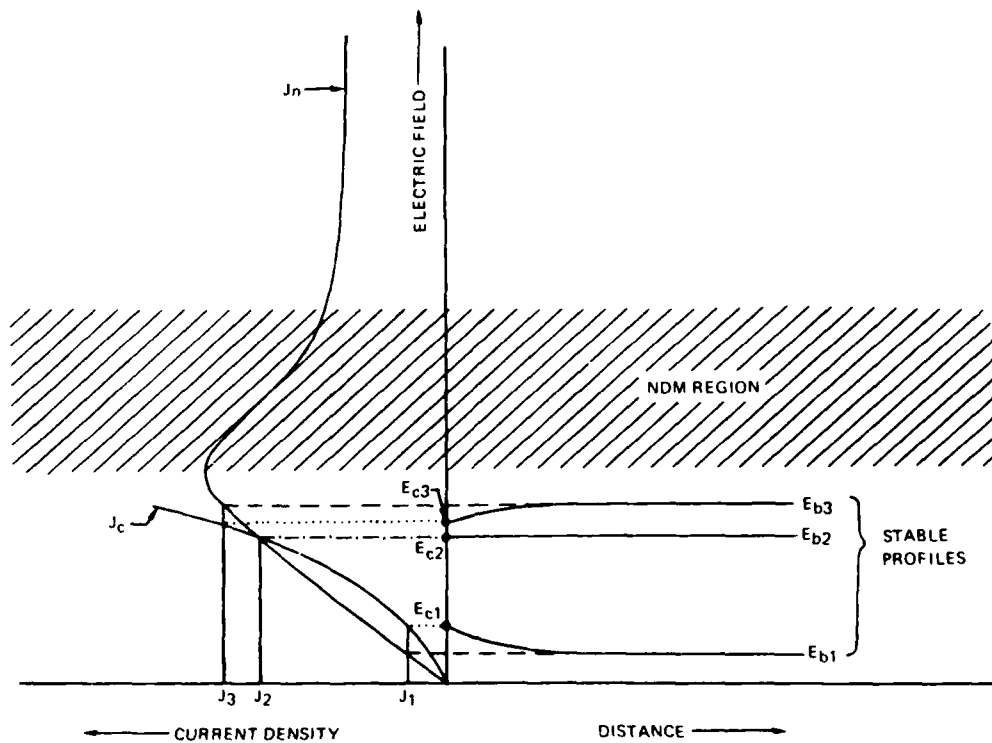


Fig. 3. Electric field versus distance profiles for the situation where $j_c(E_c)$ and $J_n(E_c)$ intersect at values of electric field below the NDM threshold field. The shaded region denotes the region of negative differential mobility.

density to j_2 results in an increase in cathode field to a value somewhere within the NDM region. The field within the bulk is still within the low field region as indicated. Further increases in current density j_3 result in the intersection of the j_n and j_c curves and charge neutrality at the cathode region boundary. Note that the field within the bulk is still significantly less than the field at the cathode boundary region. The situation at j_3 is unstable because now further increases in current density result in the formation of an accumulation layer adjacent to the cathode region, followed by a downstream depletion layer. This domain is wholly within the NDM region and may generate a large signal instability. A point worth drawing attention to at this time is made by comparing the current densities and the estimates of the average fields across the semiconductor elements, represented by Figs. 3 and 4. In Fig. 3, the current density at the instability threshold is near the peak value for NDM. Also, the average field just prior to the instability is approximately equal the threshold field for NDM. For the results

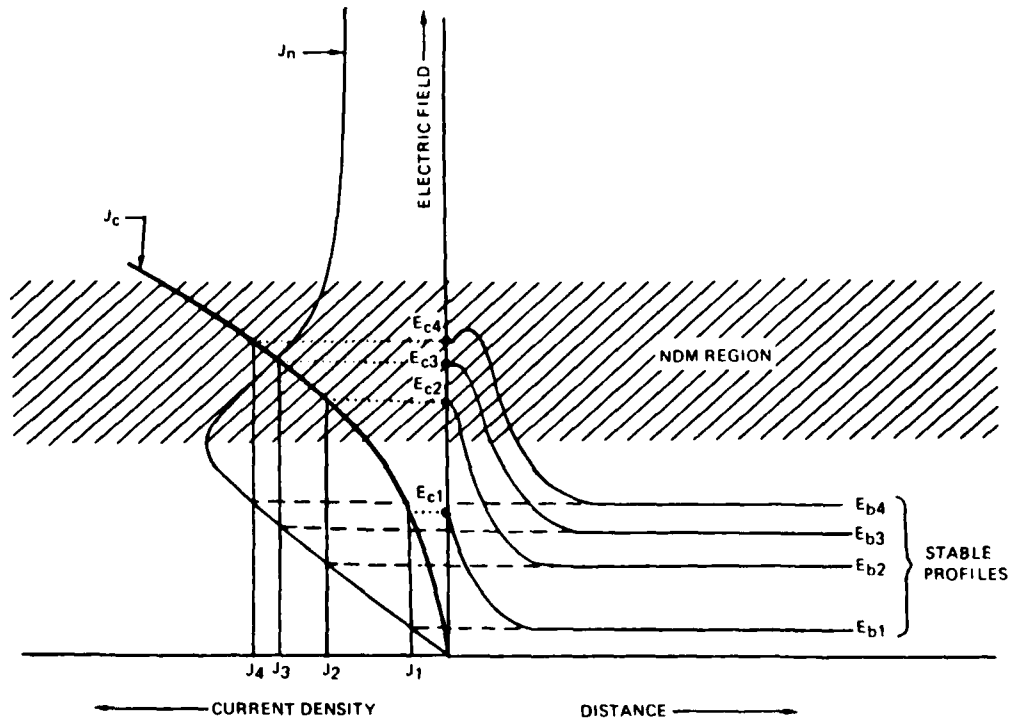


Fig. 4. As in Fig. 3, but $j_c(E_c)$ and $j_n(E_c)$ intersect within the region of negative differential mobility.

of Fig. 4, both the current densities and the average fields prior to the instability are significantly less than the NDM threshold values.

In Fig. 5, we illustrate the situation where the cathode conduction current density intersects the neutral curve somewhere within the region of saturated drift velocity region. For this case, we do not expect any charge accumulation until the value of current density exceeds the current density associated with the saturated drift velocity.

To examine the dynamic properties of these space charge layers, we resort to numerical simulation and solve the semiconductor equations simultaneously with the circuit equations. For this we need the anode contact region conditions. This is an easier contact to specify phenomenologically, for we have found that if the region is not tailored to meet specific and unusual requirements, its effect on the oscillation and instability conditions can be simulated by setting the anode field value to zero. With this in mind, we examine the simulation results.

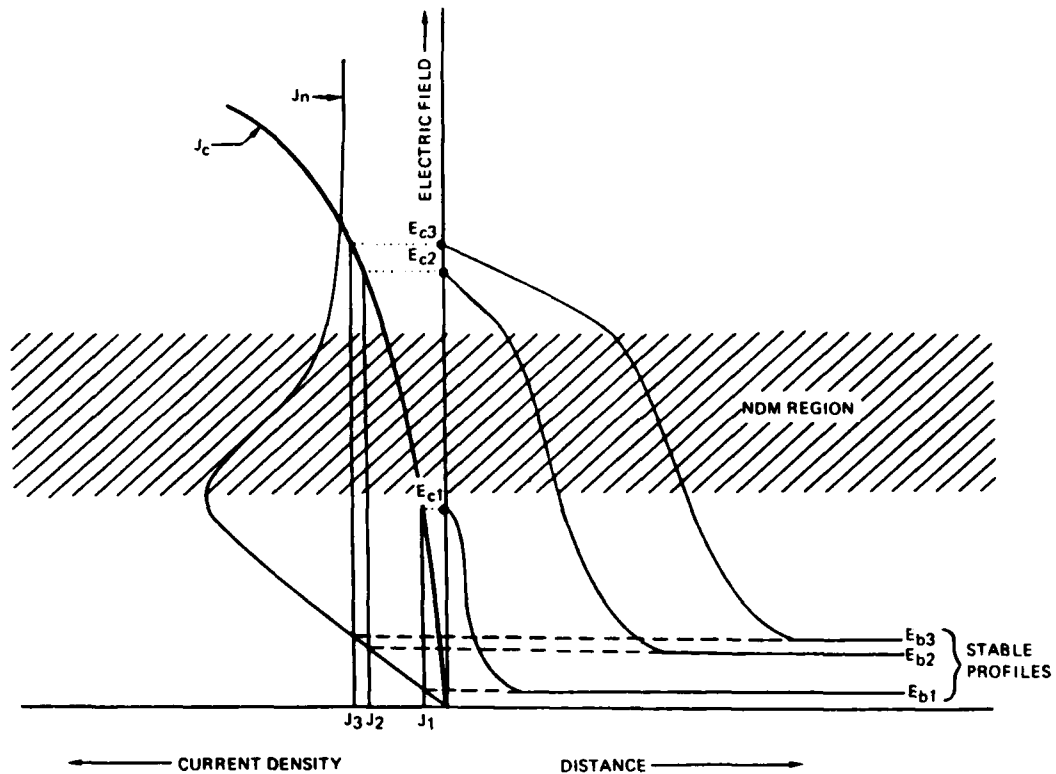


Fig. 5. As in Fig. 3, but $j_c(E_c)$ and $j_n(E_c)$ intersect within the region of saturated drift velocity.

We begin with the situation where the cathode conduction current density curve intersects the neutral curve within the region of negative differential mobility. For a resistive circuit, $Z = R$, we get the result in Fig. 6 (Shaw *et al.*, 1979) which shows the prethreshold electric field versus distance profile and the postthreshold electric field versus distance profile (at one instant of time). The nucleation criteria is the same as that discussed in Fig. 4, and the resulting domain travels between the contacts. It drains at the anode and is renucleated at the cathode region. The dc current voltage curves (Grubin, 1976b) are shown in the inset. We point out the sublinearity, just prior to the instability (represented by the 'wiggle' in the curve). The sublinearity is due to the enhanced voltage drop in the vicinity of the cathode contact. In a circuit containing reactive components, e.g., serial inductance and parallel package capacitance, the dynamic behavior of an NDM element with a similar contact may be different. This is displayed in Fig. 7a where we plot current density through a dc load resistor versus an average electric field, \bar{E} (Grubin, 1978). Time is eliminated between the two.

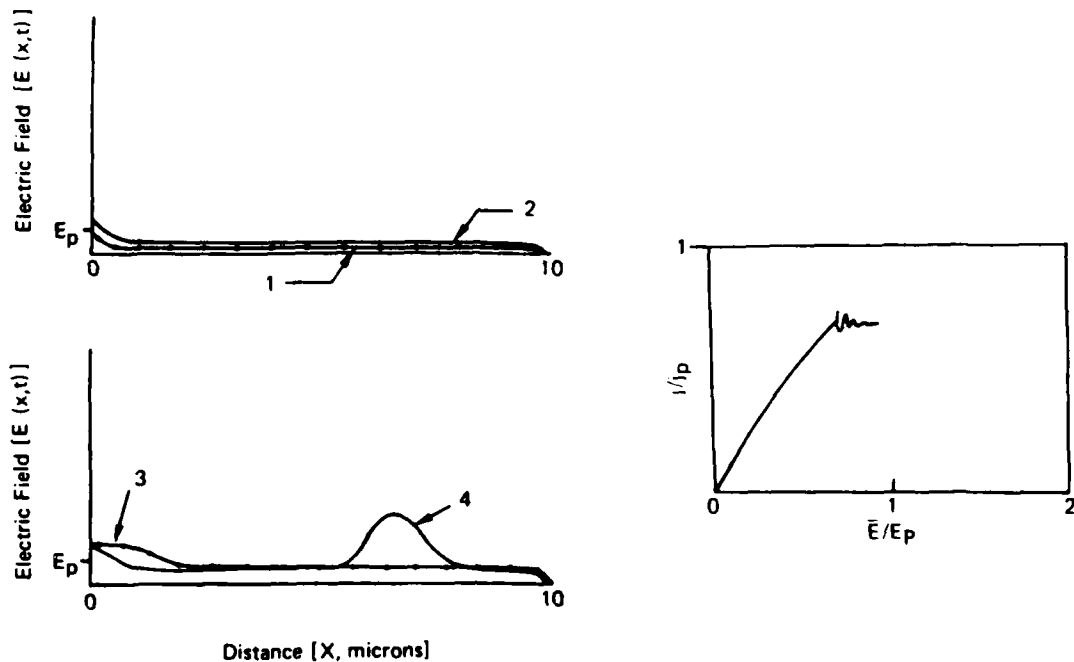


Fig. 6. Resistive circuit calculations for a 10 micron long element with $j_c(E_c)$ and $j_n(E_c)$ intersecting within the region of NDM. Curves 1, 2, and 3 denote pre-instability curves at increasing values of bias. Curve 4 denotes an instability at one instant of time. From Shaw et al. (1979). The current density versus average electric field curve for this element is shown in the graph on the right. From Grubin (1976b).

In Fig. 7b, we show the electric field versus distance profile at four instants of time. Also shown is the cathode conduction current density curve. We note that in the case of Fig. 6, the instability is dominated by the cathode contact and the frequency is determined by the transit time of the domain. In the circuit containing reactive components, the frequency here is determined primarily by the circuit elements (although this is not always the case). We note here that the oscillation appears to consist of a moving oversized dipole layer.

We show a similar set of calculations for a device in which the cathode conduction current density curve intersects the neutral curve further within the region of negative differential mobility, close to the region of velocity saturation. The results show a much weaker

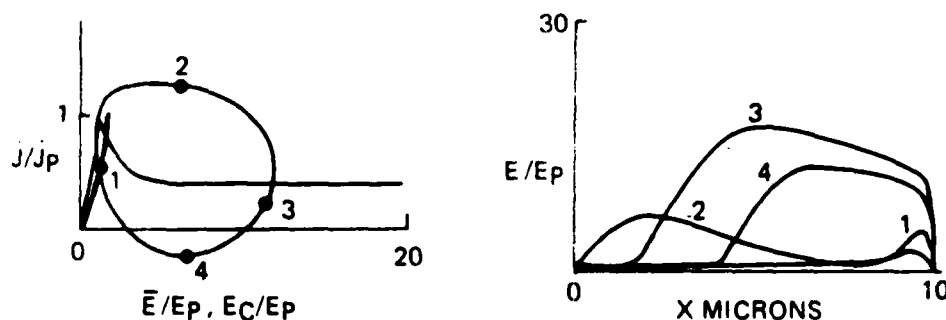


Fig. 7. Reactive circuit computations for a j_c curve that intersects j_n within the NDM region. From Grubin (1976b).

current oscillation. Indeed with cathode curves of this type, as they intersect further out we may expect the oscillatory activity to disappear. The current voltage curves for this device are shown in the inset (Grubin, 1976a) and we see a situation where the sublinearity is extreme enough to approach saturation. This excessive sublinearity is due to the large voltage drop in the vicinity of the cathode contact, as illustrated in Fig. 8.

The space charge profiles discussed above can be intuitively understood on the basis of some simple analytical concepts associated with the intersection of the neutral current density curves and the cathode conduction current density curve. There is another profile that occurs frequently in device operation that is less amenable to simple arguments. It occurs most often in devices whose cathode current density curves intersect the neutral curves at cathode field values $E_c \leq E_p$, and it manifests itself as a large voltage drop in the vicinity of the anode contact. This domain requires a region of NDM for its existence, but does not require the presence of any special anode property. The presence of these anode domains was first predicted by Shockley (1954). In resistive circuits its presence usually occurs at high bias levels and often accompanies the cessation of oscillations. In circuits containing reactive elements it usually manifests itself as a permanent and residual voltage drop in the vicinity of the anode as illustrated in Fig. 9. (In Fig. 9, rather than deal with the cathode conduction current curves of Fig. 2, we have simply set the cathode field to zero.) We show the lissajous figure for the oscillation as well as a multiple exposure of the electric field versus distance profile. This profile represents an accumulation layer that propagates toward the anode but never quenches at the anode. Instead there is always a residual space charge layer adjacent to the anode contact.

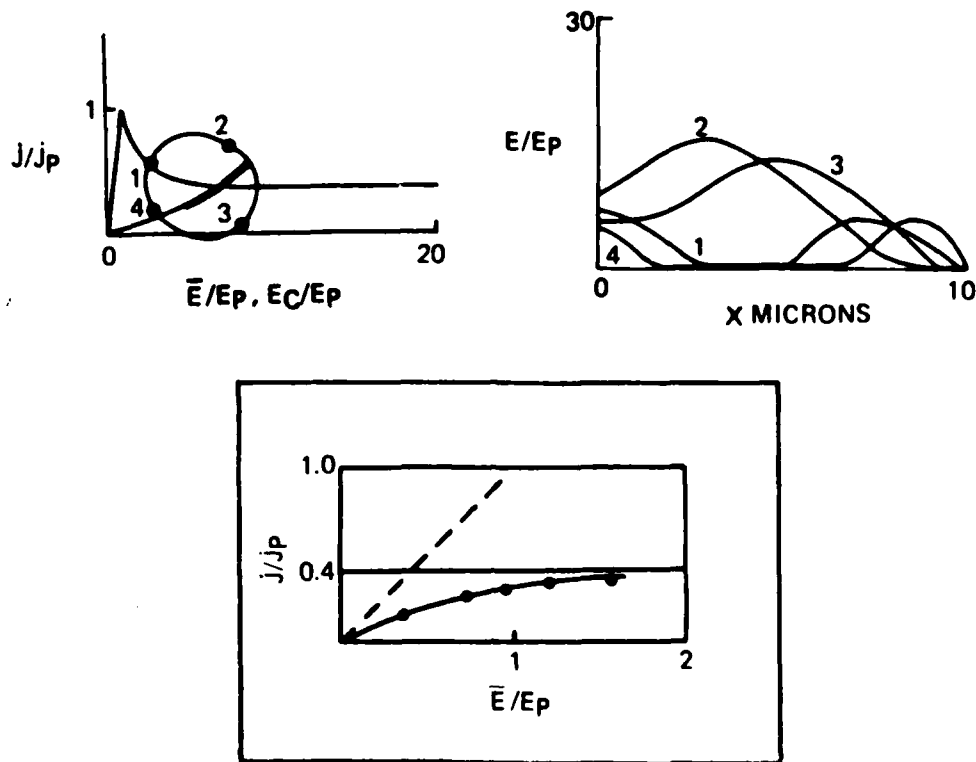


Fig. 8. As in Fig. 7, but for intersections within the region of saturated drift velocity. From Grubin (1976n). The inset shows the current density versus average electric field. From Shaw et al. (1979).

Each of the above calculations was carried out for a simulated gallium arsenide device that had an active region length of 10 microns and a doping density of $10^{15}/\text{cm}^3$. The space charge profiles were developed for a rather sophisticated model of the cathode. We point out, however, that the use of this model is not necessary for simulating the qualitative properties of the instability in GaAs. A far simpler model can be used to generate these results; one in which the cathode field, instead of being dependent on current density, is held fixed (Shaw et al., 1969). We have carried out simulations with this model for 10 micron long devices as well as 100 micron long devices. The cathode dependent results are qualitatively similar. We have also performed experiments and used the fixed cathode field model in their interpretation. The experimental results are shown in Figs. 10 through 12; and the summary of the gallium arsenide results is shown in Fig. 13.

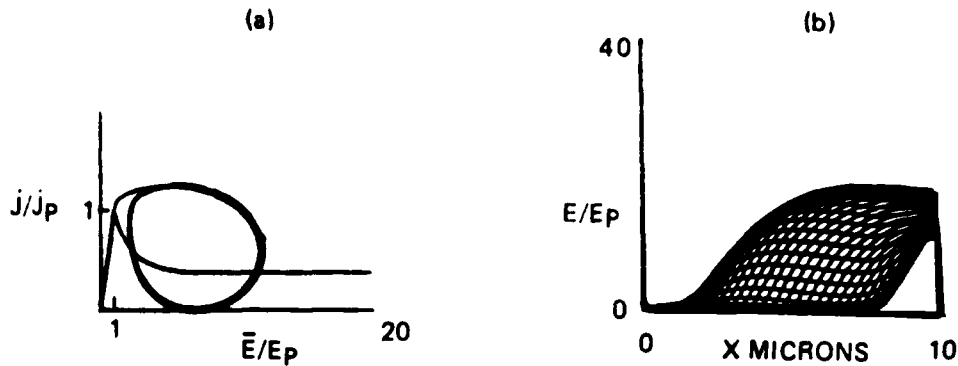


Fig. 9. Reactive circuit computations showing the presence of a permanent residual voltage drop in the vicinity of the anode contact. (a) Current density versus average electric field, (b) multiple exposures of the electric field versus distance profiles. From Grubin (1976b).

The experimental results were obtained for GaAs samples cut from bulk, doped Monsanto n-GaAs wafers and homegrown epitaxial specimens. The Monsanto wafers had quoted Hall mobilities usually between 4000 and 5000 $\text{cm}^2/\text{V}\text{-sec}$ and carrier concentrations between 5×10^{14} and $10^{16}/\text{cm}^3$. The contacts were either tin/nickel/tin or gold/germanium/nickel.

Figure 10 shows experimental current voltage and voltage versus distance profiles for a sample whose active region boundary field was below the threshold field for negative differential mobility (Solomon *et al.*, 1975). To assure this we took the expedient approach of removing the active region from the influence of the metal contact by substantially reducing the cross sectional area of a large region between the contacts. This sample and samples of this type, when in a resistive circuit, exhibited oscillatory characteristics that were more closely related to doping inhomogeneities than to the transit-time between the contacts.

Figure 11 shows experimental results for a device that sustained a transit-time oscillation. We see the enhanced sublinearity in the current versus voltage relation. This sublinearity, prior to the instability is due to the increased voltage drop at the cathode as the bias is increased. This increasing voltage drop is revealed in the probe measurements. We estimate a cathode field prior to an instability of approximately 6.2 kV/cm .

In Figure 12 we show measurements for a device that did not exhibit any time dependent behavior. Here one notices extreme saturation in

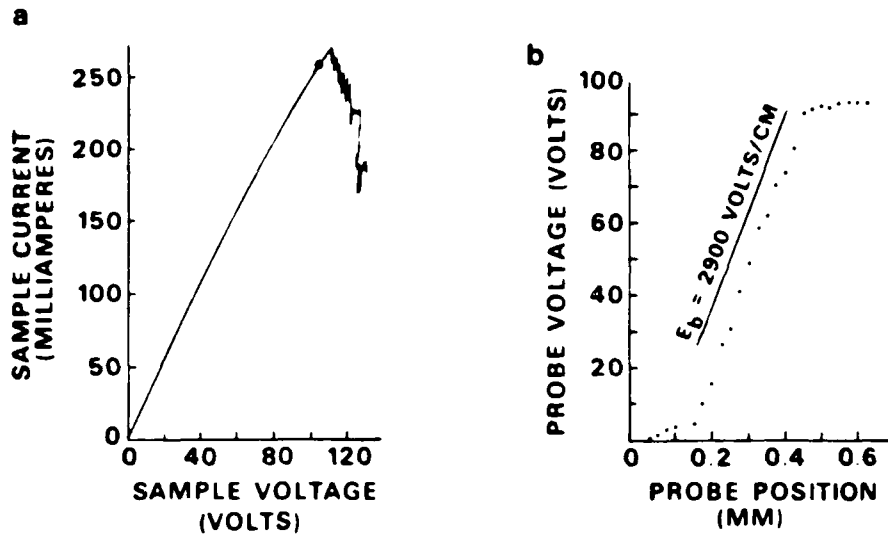


Fig. 10. (a) Current versus voltage for a low cathode boundary field GaAs sample. The probing point is indicated by the closed circle, (b) the probed voltage versus distance measurements. From Solomon et al. (1975).

current at high bias levels, while at low bias levels the current voltage relation is linear. The voltage versus distance measurements show a very large cathode voltage drop and a cathode field which we estimate to be greater than 60 kV/cm. We show measurements in both polarities to offer evidence that the large voltage drop is not a consequence of a high resistance cathode region. In both polarities we see that there is not a large anode voltage drop.

The results of the cathode boundary dependence of two terminal negative differential mobility devices is summarized in Fig. 13. Here for the same device parameters we plot current density versus average electric field (sample voltage/sample length) for different fixed values of cathode field. We superimpose the equilibrium drift velocity versus electric field relation. The properties of the instability fall into three categories. At low E_c (curve A), the j - E curve is essentially linear up to the field at peak velocity. At this point several things may occur. The possibilities depend in a detailed way on the characteristics of the GaAs and the circuit. Domains may be nucleated at large doping fluctuations in the bulk and lead to transit-time oscillations. A more interesting possibility is that after a domain is nucleated and reaches the anode it may remain there in a stationary field configuration and the current will saturate. In a resonant circuit the field may oscillate at the resonant frequency. For E_c within the shaded region, the current

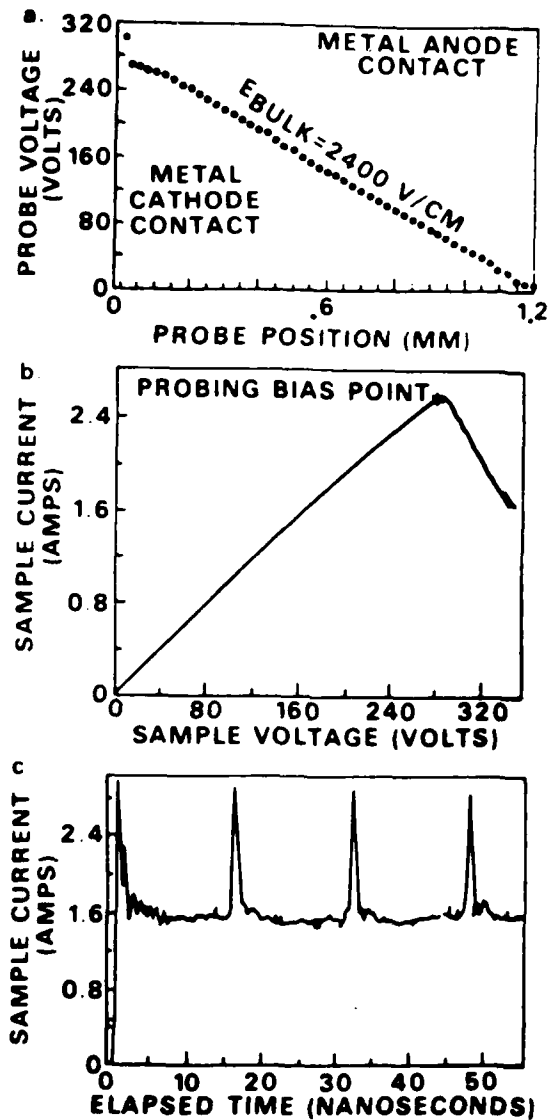


Fig. 11. Probed sample voltage versus distance for and intermediate cathode boundary field, at the bias point indicated in (b). (b) Current versus voltage, (c) instability current versus time response. From Solomon et al. (1975).

shows a departure from linearity due to the appearance of a large cathode voltage drop. At threshold the current switches along the load line. Threshold is controlled by the cathode field and not by the threshold field for negative differential mobility. Threshold occurs before the bulk enters the region of negative differential

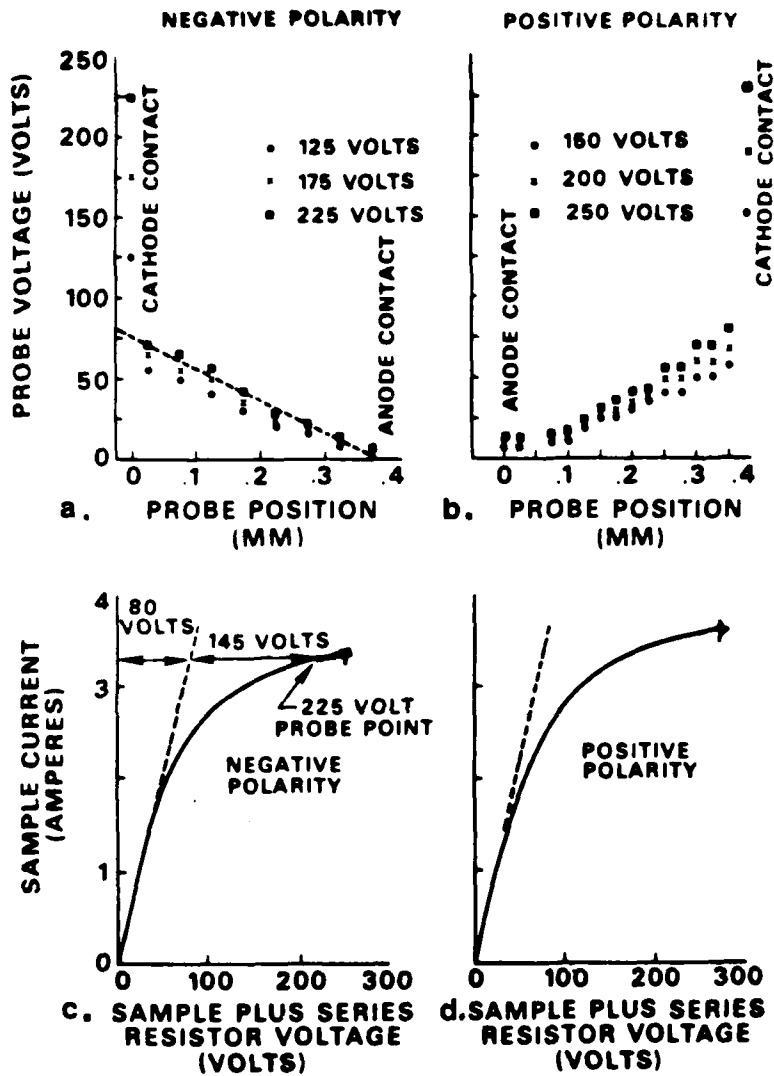


Fig. 12. Probed sample voltage versus distance for a high cathode field sample in (a) negative and (b) positive polarities. Current versus voltage curves for (c) negative and (d) positive polarities. From Solomon et al. (1975).

mobility. For high values of cathode field the current voltage characteristic is linear only at low bias. At high bias the curve saturates at the current density $j_s = N_0 e v_s$. The departure from linearity corresponds to the appearance of a large cathode voltage drop and transit-time oscillations in a resistive circuit do not occur. In a resonant circuit the sample may sustain some oscillatory activity for a certain range of boundary field. We note that in all cases where an oscillation occurs, stable domain propagation requires

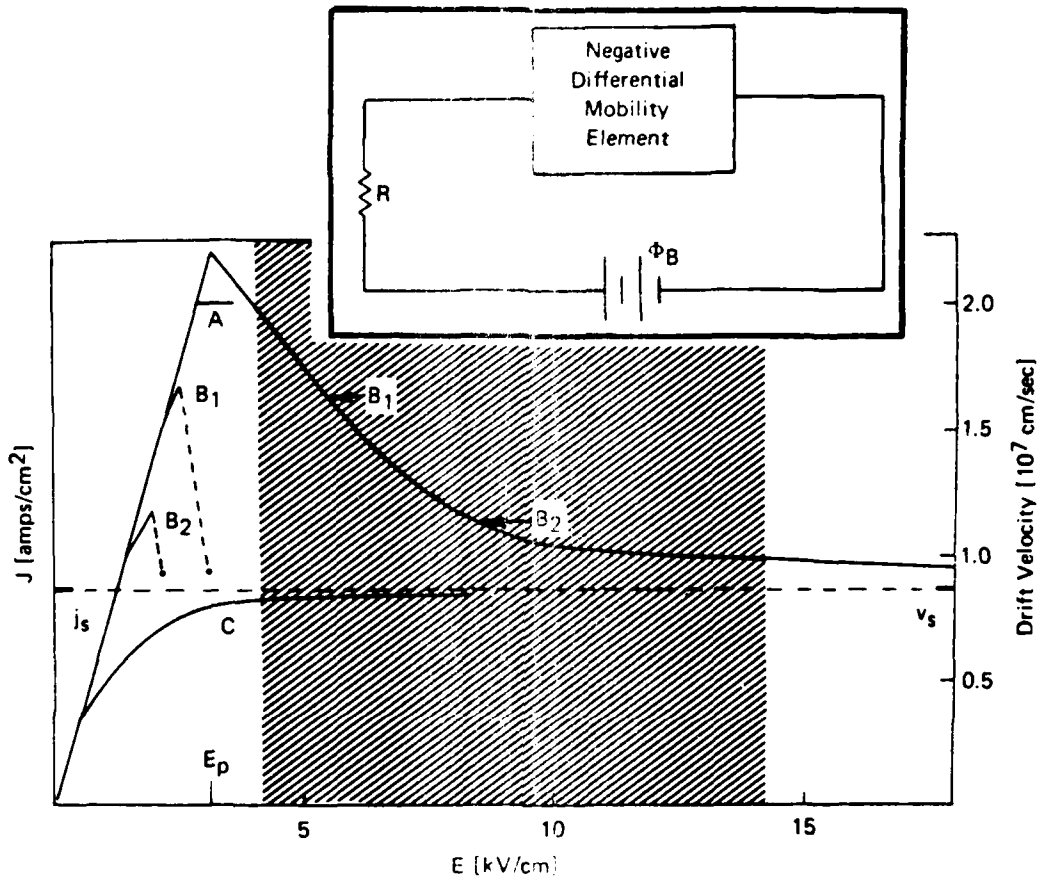


Fig. 13. The equilibrium velocity electric field curve and the computer simulated current density versus average electric field curve for various fixed values of cathode boundary field E_c . For the simulation the NDM element is in the circuit shown in the inset. For curve A, $E_c = 0.0$. The values for curve B_1 and B_2 are indicated by the arrows. For curve C, $E_c = 24 \text{ kv/cm}$. The simulated element had an active region length of 100 microns and a doping level of $10^{15}/\text{cm}^3$. The right and left hand ordinates are related by $j_n = N_0 v$ and $v_s = 0.8 \times 10^7 \text{ cm/sec}$. From Shaw et al. (1969).

that the current level exceed the saturated drift current, sometimes referred to as the sustaining current.

The above discussion appears to present a rather complete phenomenological description of the contact and circuit dependence of gallium arsenide two terminal devices. The model has also been applied to

the indium phosphide device. Here the presently known contact behavior is somewhat richer than that for gallium arsenide and while (2) and (3) can be used to simulate the InP behavior, the fixed cathode field approximation is in some cases inadequate. In particular, while a number of classes of devices can be explained with contact curves represented by Figs. 3 through 5, the appearance of very high efficiency oscillations (Colliver *et al.*, 1973) with prethreshold current voltage curves similar to that of Fig. 8, requires $j_c(E_c)$ curves similar to that of #4 in Fig. 2 for its simulation. This curve is qualitatively different from the curves discussed earlier, for as the range of current oscillations the cathode conduction current is approximately constant, while the cathode field can almost freely move about. A plot of the electric field profiles during the course of the oscillation is shown in Fig. 14. We note that immediately downstream from the cathode contact the electric field profile is approximately uniform. We now turn to the subject of three terminal devices.

THREE TERMINAL DEVICES

We are interested in the hot electron contributions to the operation of gallium arsenide field effect transistors (FET). The FET in its simplest form is a semiconductor slab with three terminals. Two of these are usually low resistance contacts, while the third is either a Schottky contact or a PN junction with an accompanying region of charge depletion. For a unipolar conduction device, operation is based on modulation of the depletion region which is usually accomplished by changes in the gate bias. Small and large signal (Colliver *et al.*, 1973) gain are possible. Figure 15 is a sketch of the device and connecting lumped elements, whose operation we have simulated. Our (two dimensional) numerical simulations and experiments (Grubin *et al.*, 1979) demonstrate that the GaAs FET can be placed in one of two groups as determined by the ratio

$$K = \frac{\text{Gate voltage at cutoff}}{\text{Drain voltage at the onset of current saturation for zero gate voltage}} \quad (7)$$

Devices with K greater than unity sustain current oscillations, whose origin lies in the presence of negative differential mobility in the semiconductor. Those with K approximately equal or less than unity are electrically stable. We point out that in the original FET discussion, as given by Shockley (1952), K was necessarily equal to unity. The situation with K greater than unity is summarized in Fig. 16a, while that for K approximately equal to unity is summarized in Fig. 16b (Grubin, 1977). In Fig. 16 we sketch the current voltage relation for a gallium arsenide FET with the parameters listed in the caption. For reference we have drawn the velocity electric field

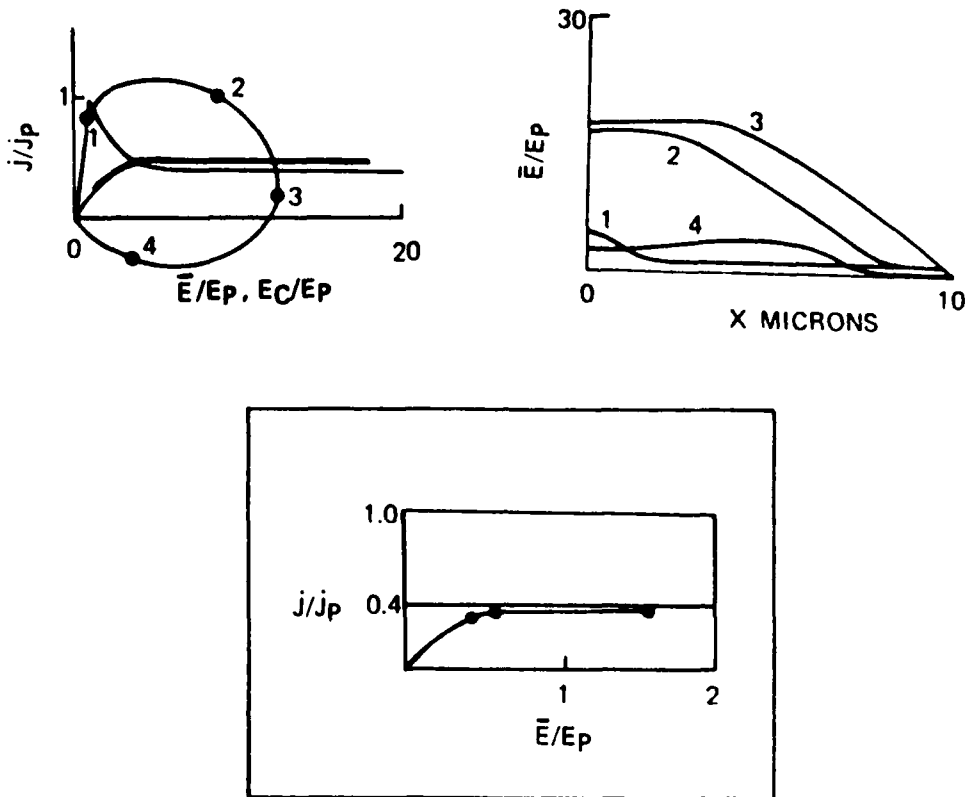


Fig. 14. Reactive circuit calculations for the cathode conduction current curve #4 of Fig. 2. The inset shows the pre-instability current density versus average electric field curves for the element in a resistive circuit. From Shaw et al. (1979).

relation for GaAs scaled to the current and voltage parameters. The first point to note is that the current levels do not approach the peak current associated with GaAs. This is a consequence of the additional resistance supplied by the gate region as well as velocity limitations. We recall from our earlier discussion of two terminal GaAs devices that sublinearity in the GaAs I-V relation is often accompanied by a current instability. For the wider channel device shown in Fig. 16 similar behavior occurs. The instability is represented by the dashed part of the I-V curves of Fig. 16a. The x's in the diagram represent average current and voltage values for the instability, and the presence of negative conductance is due to the dynamic propagating domain. The closed circles in Fig. 16 represent stationary, time-independent points, and we note that when there is an instability it is surrounded by regions of nonzero gate and drain

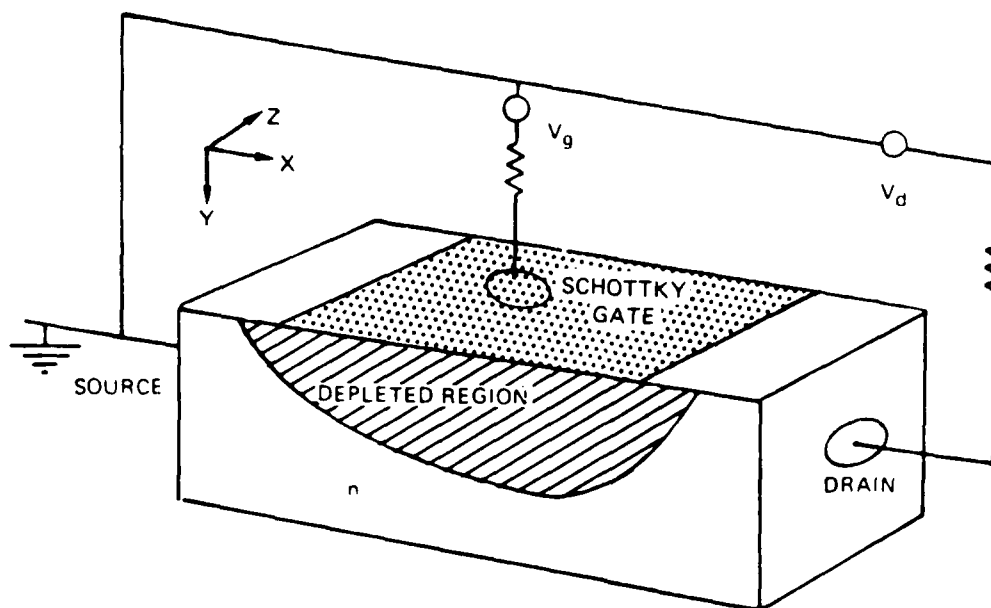


Fig. 15. Schematic representation of a Schottky - gate field effect transistor.

bias for which there is no time-dependent behavior. We now illustrate the space charge distribution associated with the x's and closed circles.

The internal distribution of charge and current associated with the current and potential levels '1' and '2' of Fig. 16a are shown in Fig. 17 (Grubin and McHugh, 1978). Column a shows a set of current density streamlines through the device. The length of each streamline is proportional to the magnitude of the vector current density at the point in question. The maximum length of the individual x and y components before overlap is $j_p = N_0 e v_p$ where v_p is the peak carrier velocity. We see in both cases that the current density is greatest under the gate contact as required by current continuity. For the higher bias case, the current density under the gate region is at least as great as j_p and velocity limitation introduces carrier accumulation. The density of charge particles in the FET is generally nonuniform and column b of Fig. 17 is a projection of this distribution as it may relate to the current density profile of column a. We point out that the particle density increases in the downward direction. The first frame shows a region of charge depletion directly under the gate contact. The second frame shows the formation of a weak stationary dipole layer under the gate contact. We see from these diagrams that the x-component of electric field has reached the NDM threshold field value at the drain edge of the gate contact. We point out that an analysis of the potential distribution

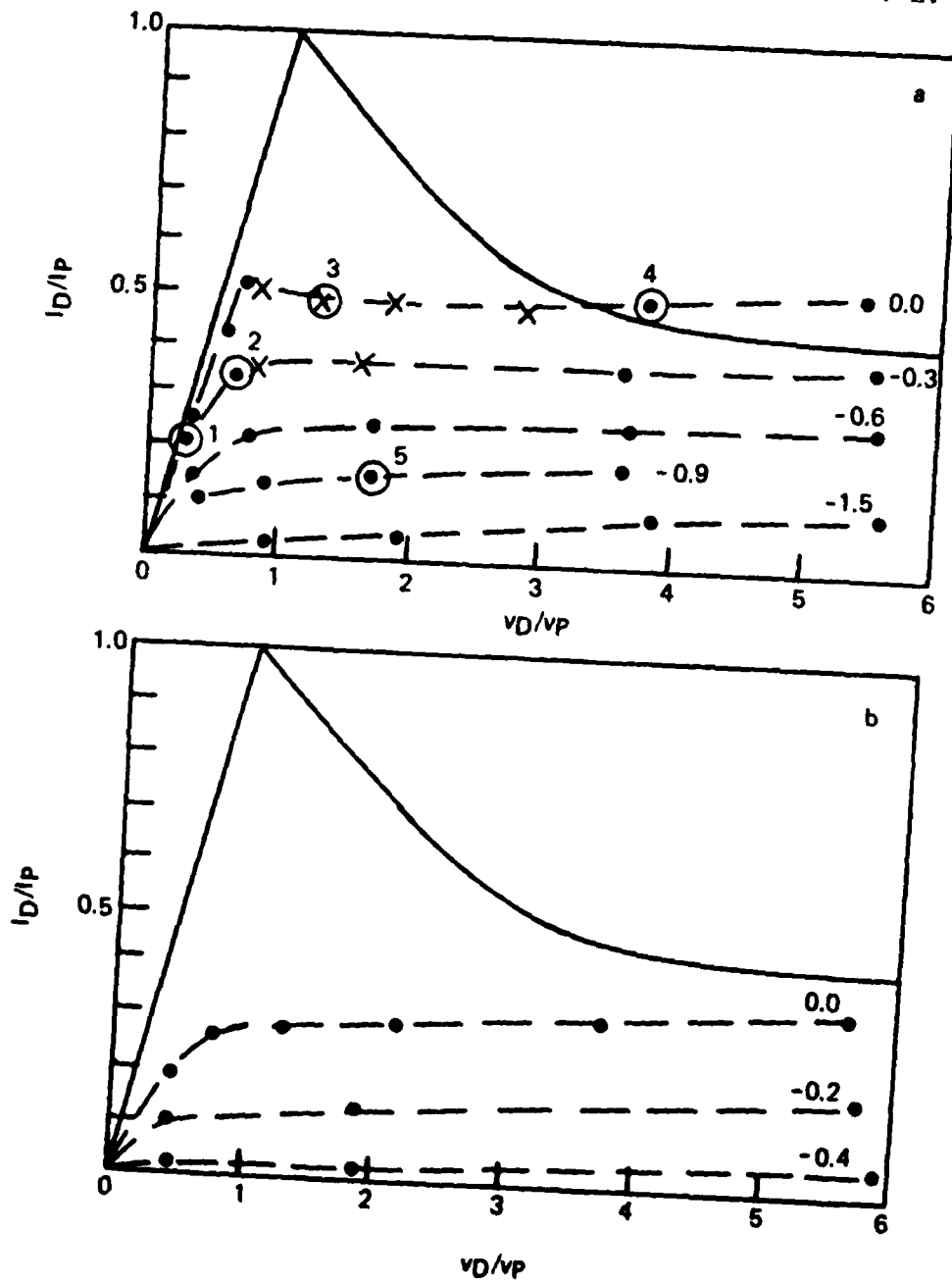


Fig. 16. Drain current - drain voltage relation. Circles denote computed points, x's denote averages of the current during an oscillation. For the calculations the doping of the active region was $10^{15}/\text{cm}^3$. Thus a wide channel device as represented in (a) had a channel height of 2.24 microns. The narrow channel device as represented by (b) had a channel height of 1.22 microns. From Grubin (1977). Note: $I_p = N_0 e v_p A$, $v_p = E_p L$.

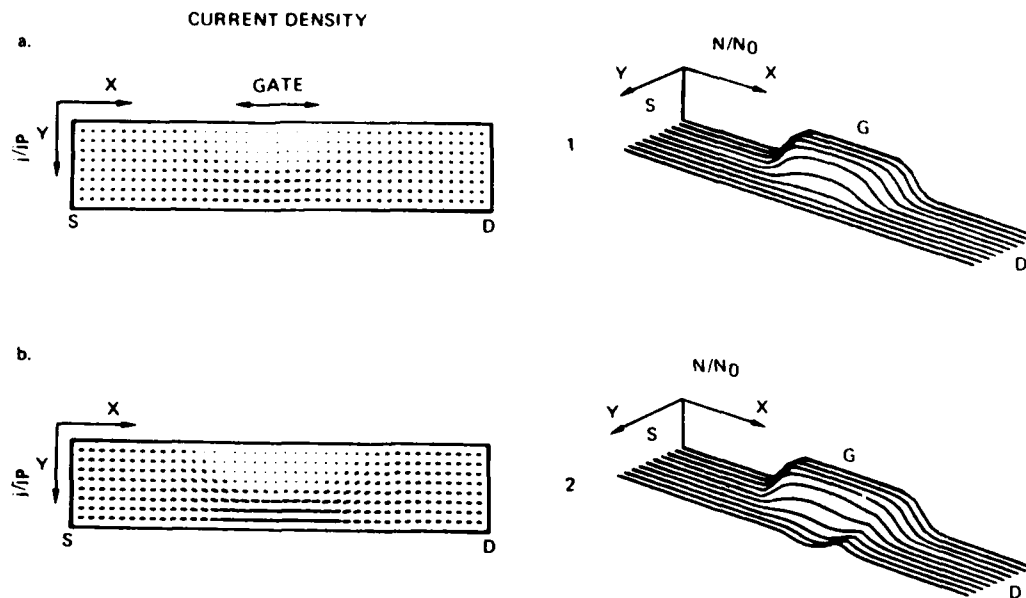


Fig. 17. The internal distribution of current and charge corresponding to the current and voltage levels represented by numbers '1' and '2' of Fig. 16. Note that the particle density surrounding the nonuniform distribution is uniformly distributed within the source-gate region and the gate-drain region. From Grubin and McHugh (1978).

shows that at the high bias levels most of the potential drop is under the gate contact.

We now consider the presence of an instability (Grubin and McHugh, 1978). We recall that for two terminal devices the instability was determined by the value of electric field at the cathode boundary region and that the threshold current density for the instability could be anywhere between j_s and j_p , where j_s is the current density associated with the high-field saturated drift velocity. In three terminal devices, the initiation of a domain instability generally occurs under the gate contact. The instability occurs at a value of current density approximately equal to j_p . Figure 18 provides a dramatic representation of the FET instability, where we see the nucleation, propagation and recycling of a high field domain. The sequence of events associated with the instability is as follows: Domain growth under the gate is accompanied by an increase in potential across the device. A corresponding decrease in current occurs throughout the device and circuit, as constrained by the dc load line. As the current decreases, carriers with velocities below that of the peak velocity enter the accumulation layer which subsequently

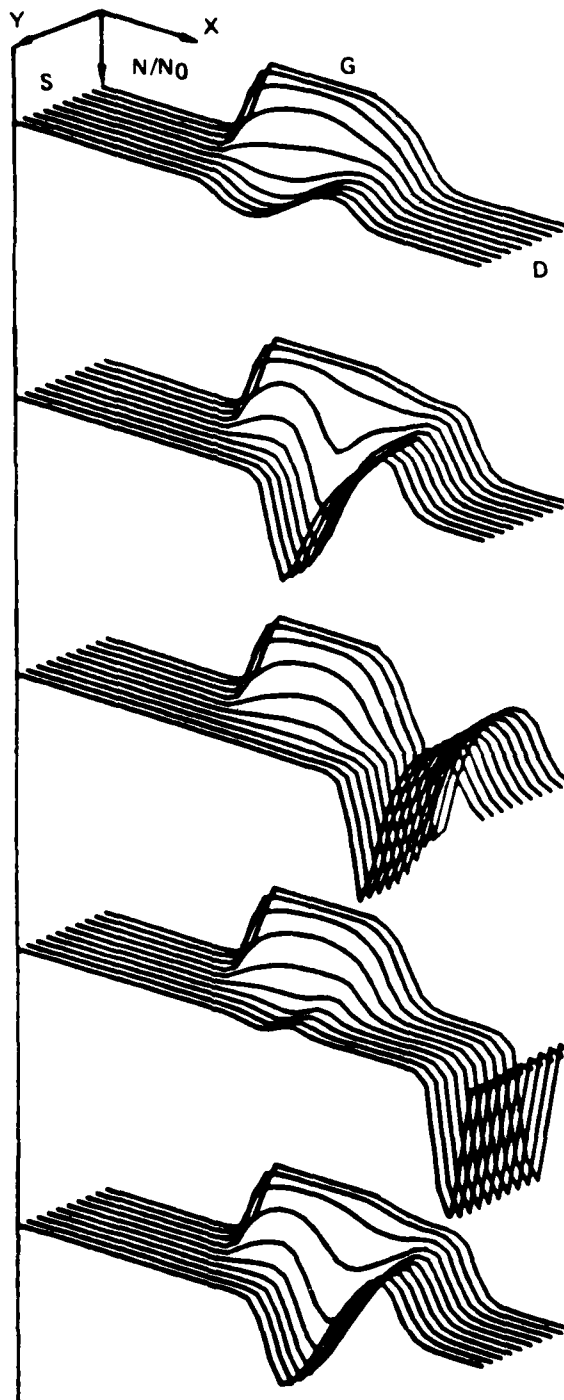


Fig. 18. Projection of the time dependent particle density when an instability occurs. The parameters at which this occurs are represented by the number '3' in Fig. 16. From Grubin and McHugh (1978).

begins to detach. The domain spreads as it leaves the gate region and it settles into a value of current density somewhat in excess of that associated with the saturated drift velocity of the electrons. Prior to reaching the drain contact the domain dynamics appear to be one dimensional.

The numerical situation at high drain bias levels and zero gate bias is similar to that of two terminal devices. Namely the oscillations cease and are accompanied by the presence of an accumulation layer extending from the gate to the drain contact. This is illustrated in Fig. 19. The region of space charge accumulation is accompanied by a large nonuniform potential drop in the gate to drain region with resulting high values of electric field and electrons traveling at their saturated drift values. This region of space charge accumulation is qualitatively similar to the anode-adjacent domain discussed in connection with Fig. 9.

Our discussion of two terminal devices indicates that large values of cathode boundary fields limit the downstream carrier velocity to values below the saturated drift value. Instabilities, if present, are damped. An analogous situation occurs with three terminal devices when a large negative bias is applied to the gate contact. For this case the depletion layer moves toward the bottom of the channel and the source-drain current is low (Grubin and McHugh, 1978). A large potential drop is present under the gate contact resulting in the formation of a high field domain. As seen in Fig. 20, the domain consists of an accumulation region surrounded by a depletion zone.

The experimental situation with regard to hot electron contributions to the FET may be summarized by turning to Fig. 21 (Grubin and McHugh, 1978) where we show the dc current voltage characteristics for a device whose parameters are listed in the caption and for which $K > 1$. The cross hatched region shows the range over which current oscillations were observed as detected by a spectrum analyzer. Oscillations were detected over a range of 6 to 40 GHz. In all of our experiments in which oscillations were observed, the instability occurred beyond the 'knee' of the current voltage relation. Prior to the oscillation the drift velocity in the gate to drain region was approximately equal to or greater than the saturated drift velocity of the carriers. Saturation in current occurred when the average field within the conducting channel under the gate contact was approximately equal to the threshold field for negative differential mobility (Grubin, 1977). The instability was suppressed either by going to a sufficiently high drain bias or by going to a sufficiently large and negative gate bias, such that in the latter case the gate to drain channel current density was below j_s .

The above discussion demonstrates that in wide channel devices hot electron effects in three terminal devices are similar to that of

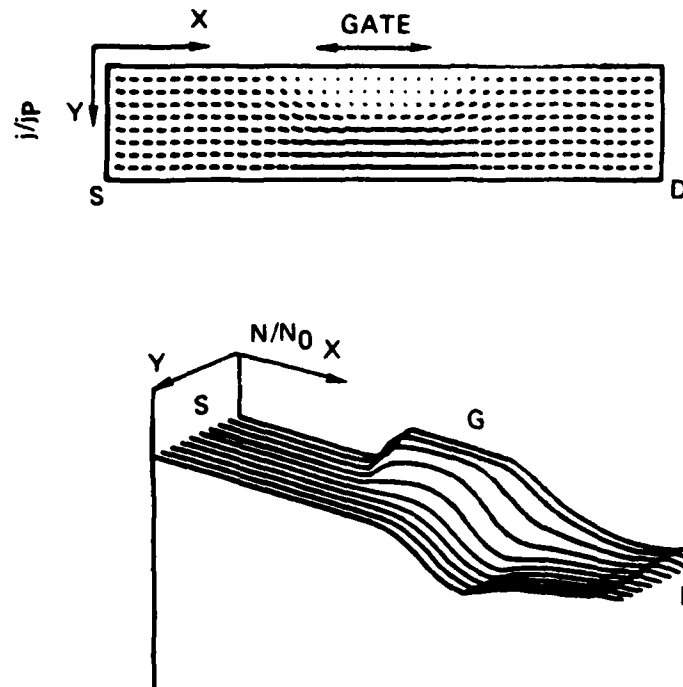


Fig. 19. Distribution of current and particle density for the case represented by '4' of Fig. 16. The instability has ceased. Note that the current density within the gate to drain region, where there is particle accumulation, is accompanied by current density levels that are approximately equal to the saturated drift current. From Grubin and McHugh (1978).

two terminal devices. A simple intuitive picture of this commonality arises after making a one-to-one correspondence between the potential drop in that portion of the conducting channel that is under the gate contact and a phenomenological cathode boundary for two dimensional devices.

The situation with narrow channel devices is somewhat less dramatic from the point of view of domain instabilities. Generally because of the nonlinear distribution of potential under the gate contact, very thin devices sustain current densities significantly below j_s in the region between the gate-to-drain contact. As in two terminal devices, this is sufficient to prevent an instability.

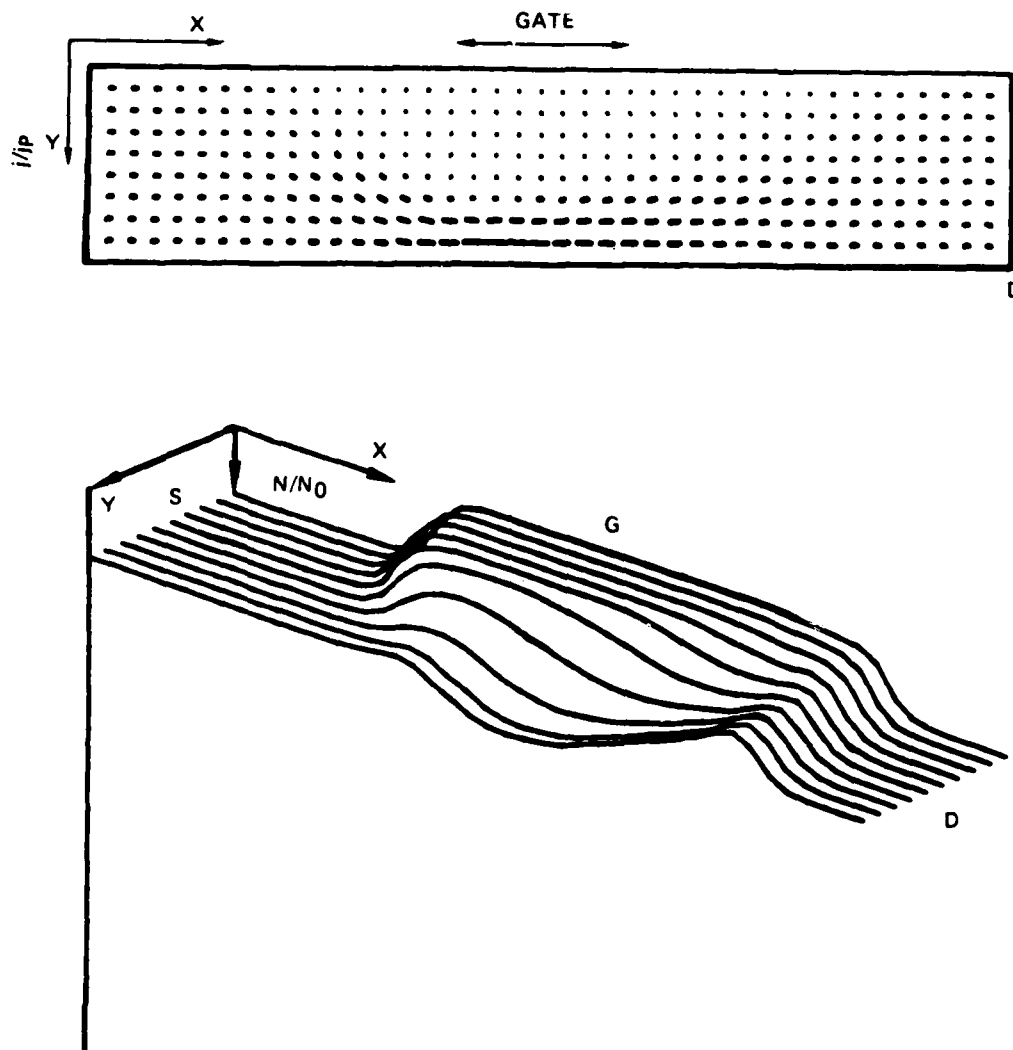


Fig. 20. Distribution of current and particle density for the case represented by '5' in Fig. 16. The instability has ceased. Note the large dipole layer within the vicinity of the gate contact, and the fact that the current density between the gate and drain region is very small. From Grubin and McHugh (1978).

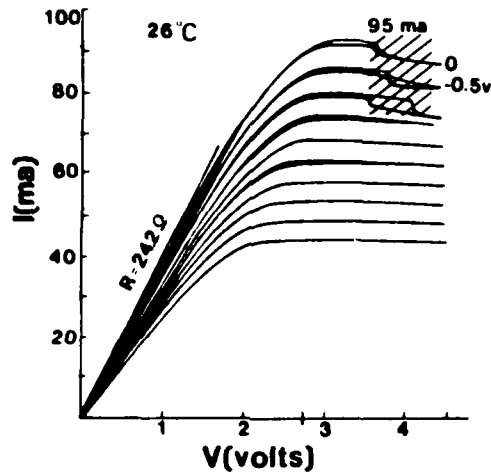


Fig. 21. Measured dc current voltage data for a gallium arsenide field effect transistor. The device had a nominal doping level of $10^{17}/\text{cm}^3$, and epitaxial layer thickness of $3000 \pm 500 \text{ \AA}$, a source-drain spacing of approximately 8.5 microns and a gate length of 3.0 microns. The mobility measured from adjacent samples varied from 3000 to 4000 $\text{cm}^2/\text{v-s}$. The cross-hatched region of the figure denotes the bias range for the instability, as detected by spectral analysis. Details of the experimental results are discussed in Grubin et al. (1979), from which this data is taken.

BIBLIOGRAPHY

- Colliver, D.J., Gray, K.W., Jones, D.J. Rees, H.D., Gibbons, G., and White, P.M., 1973, in "Proceedings International Conference on GaAs and Related Compounds," Inst. of Phys., London.
- Grubin, H.L., 1976a, J. Vac. Sci. Techn. 13:786.
- Grubin, H.L., 1976b, IEEE Trans. Electron Dev. ED-23:1012.
- Grubin, H.L., 1977, in "Proceedings 6th Biennial Cornell Electrical Engineering Conference," Cornell University.
- Grubin, H.L., 1978, IEEE Trans. Electron Dev. ED-25:511.
- Grubin, H.L., 1979, this volume.
- Grubin, H.L., and McHugh, T.M., 1978, Sol.-State Electr. 21:69.
- Grubin, H.L., Ferry, D.K., and Gleason, K.R., 1979, Sol.-State Electr., in press.
- Gunn, H.B., 1964, IBM J. Res. Develop. 8:141.
- Kroemer, H., 1968, IEEE Trans. Electron Dev. ED-15:819.
- Rideout, V.L., 1975, Sol.-State Electr. 18:541.
- Shaw, M.P., Solomon, P.R., and Grubin, H.L., 1969, IBM J. Res. Develop. 13:587.
- Shaw, M.P., Grubin, H.L., and Solomon, P.R., 1979, "The Gunn-Hilsum Effect," Academic Press, New York.

- Solomon, P.R., Shaw, M.P., Grubin, H.L., and Kaul, R.D., 1975, IEEE Trans. Electron Dev. ED-22:127.
- Shockley, W., 1952, Proc. IRE 40:1365.
- Shockley, W., 1954, Bell Sys. Tech. J. 33:799.
- Thim, H.W., 1968, J. Appl. Phys. 39:3897.

Reprinted from:

PHYSICS OF NONLINEAR TRANSPORT IN SEMICONDUCTORS (1980)
Edited by David K. Ferry, J.R. Barker, and C. Jacoboni
Book available from: Plenum Publishing Corporation
227 West 17th Street, New York, N.Y. 10011

HOT ELECTRON EFFECTS IN SEMICONDUCTOR DEVICES

H. L. Grubin

United Technologies Research Center
East Hartford, Connecticut 06108

INTRODUCTION

The original impetus for much of the hot electron work that has taken place in the last decade was the need to understand the contributions of hot electrons to semiconductor devices. The turning point in this area of study occurred when Gunn (1964a) published his results showing the presence of spontaneous and coherent oscillations in gallium arsenide and indium phosphide two terminal devices. Today, of course, hot electron phenomena are being studied for their own interest, and with ends that are ostensibly independent of device considerations. But, in fact, the two areas cannot be separated. Rather the emphasis is different, with hot-electron-device studies concentrating on situations where the electric field sustains large and fast transients and where the field is highly nonuniform.

Typically, when it is of interest to find an experimental situation that best illustrates hot electron device effects, the results of Gunn's early studies are shown. In Fig. 1, we display results (Gunn, 1964a) of a current instability in gallium arsenide. Here we show sampled current - voltage characteristics of a device thirty-six microns long. Mathematically, these results are plots of current as a function of voltage with time held constant. At low voltages the I-V relationship is nearly linear. At higher voltages the dc conductance first decreases slightly; then at some value of voltage there occur wide differences in current between successive samples. This appears as a large scatter of dots representing individual samples. In a subsequent series of experiments Gunn (1964b) established that these fluctuations in current were consequences of coherent oscillations associated with a moving distribution of potential within the semiconductor.

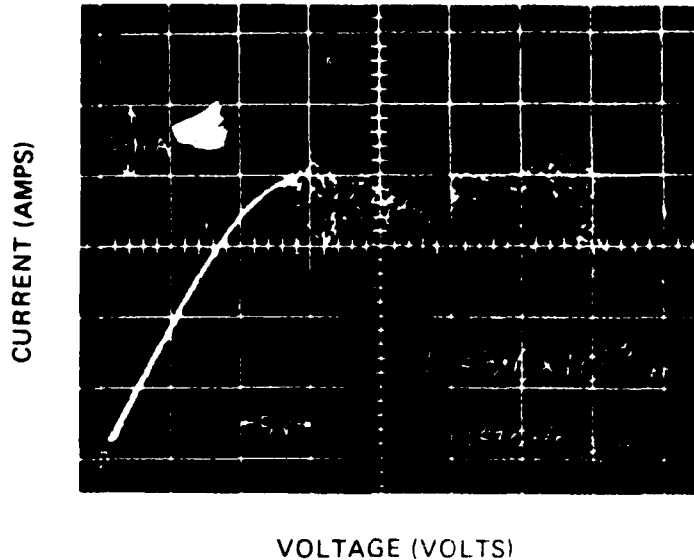


Figure 1. Sampled current-voltage characteristics of an n-type GaAs specimen. The active region lengths and scales are shown in the figure. From Gunn (1964a) with permission.

Gunn's experiments demonstrated that the semiconductor gallium arsenide was capable of converting dc to ac power. Our present explanation (Kroemer, 1964) for this conversion is that, through the mechanism of electron transfer (Ridley and Watkins, 1961) from the central to satellite valleys of the conduction band, gallium arsenide possesses a region of negative differential mobility (Hilsum, 1962) (see Fig. 2). As discussed by Ridley (1963), the presence of negative differential mobility can lead to unstable localized space charge regions. The observations of Gunn are then explained as arising from the periodic nucleation and disappearance of traveling space charge domains (Kroemer, 1964).

Figure 2, which is the drift velocity versus electric field curve for gallium arsenide (Butcher, 1967), represents what most device physicists regard as the basis of hot-electron transport effects in devices. Indeed, very sophisticated numerical programs have been designed around this curve and used to model the spatial and time-dependent dynamics of electrons in devices. Remarkable agreement with experiment has been obtained that has also included explanations of fine details of observations. I will illustrate some of these in a following chapter. Perhaps the most noteworthy point is that the velocity field curve, as represented by Fig. 2, derived

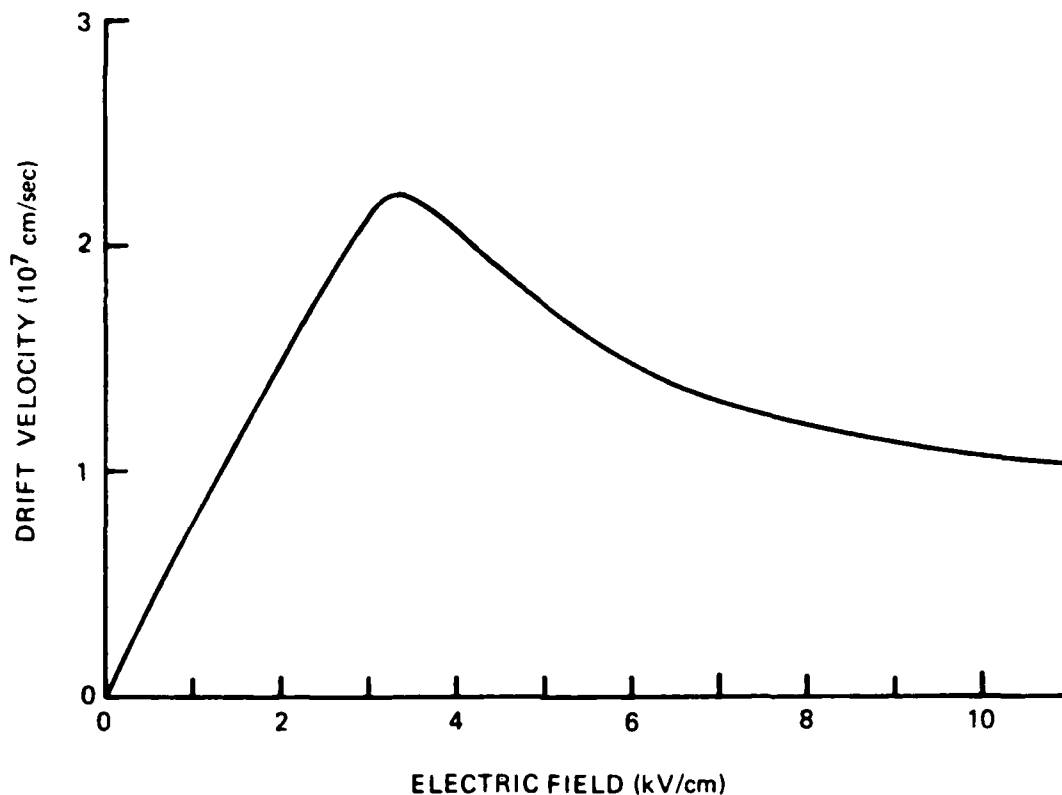


Figure 2. Calculation of the steady state drift velocity versus electric field curve for gallium arsenide. From Butcher (1967) Figure 3, with permission.

under steady-state conditions and spatially-uniform fields, is often used to explain transient phenomena and highly nonuniform situations. It is this latter use that is currently the subject of increased scrutiny and will occupy the rest of the current discussion. These topics properly come under the heading of transient hot-electron effects in semiconductor devices.

Before beginning the discussion we must lay a few ground rules. We will provide a microscopic description of carriers in a semiconductor device in terms of a displaced Maxwellian

$$f(\vec{p}_1, T_1) = A(n_1/T_1^{3/2}) \exp[-\hbar^2(\vec{k}-\vec{p}_1)^2/2m_1k_0T_1] \quad (1)$$

The dynamics of the particles are then obtained from moments of the Boltzmann transport equation in the form (Bosch and Thim, 1974)

$$a_i \frac{\partial n_i}{\partial t} = - \frac{n_i}{\tau_{n_i}} + \frac{n_j}{\tau_{n_j}}, \quad (2)$$

$$\frac{\partial n_i \vec{p}_i}{\partial t} = - e n_i \vec{F} - \frac{n_i \vec{p}_i}{\tau_{p_i}}, \quad (3)$$

$$\frac{\partial}{\partial t} \left\{ \frac{n_i p_i^2}{2} + \frac{3 n_i k_o T_i}{2} \right\} = \frac{-e n_i \vec{F} \cdot \vec{p}_i}{m_i} - \frac{n_i k_o T_i}{\tau_{E_i}} + \frac{n_j k_o T_j}{\tau_{i_j}}. \quad (4)$$

In the above, a_i represents the number of equivalent satellite valleys, n_i , p_i and T_i are respectively the number density, the momentum and temperature of the i th valley. Further, we have ignored the spatial contributions to the moment equations. The τ 's in the above equation are scattering times for intervalley and intra-valley transfer and significant effects arise because of important differences between the energy and momentum relaxation time. Fig. 3 shows a set of scattering times for gallium arsenide calculated in 1974 by Bosch and Thim (1974). These calculations are for the Γ -X ordering in gallium arsenide in which the number of equivalent satellite valleys is equal to 3. Calculations for the Γ -L ordering with four equivalent satellite valleys have not yet been published, although several groups are pursuing the problem. We note that at room temperature, the momentum scattering time for the central valley is significantly smaller than the energy scattering time. The significance of this will emerge below in connection with overshoot velocity.

TRANSIENT HOT ELECTRON EFFECTS IN SEMICONDUCTOR DEVICES

Velocity Overshoot

If a system of electrons is subjected to the combined influence of an electric field and scattering centers, ignoring for the moment electron transfer as a scattering mechanism, then the drift velocity of the particles asymptotically approaches the steady state value

$$v = -e \langle \tau \rangle F / m^*. \quad (5)$$

$\frac{1}{\tau_{n1}}$, $\frac{1}{\tau_{n2}}$: PARTICLE SCATTERING
$\frac{1}{\tau_{p1}}$, $\frac{1}{\tau_{p2}}$: MOMENTUM SCATTERING
$\frac{1}{\tau_{E1}}$, $\frac{1}{\tau_{E2}}$, $\frac{1}{\tau_{12}}$, $\frac{1}{\tau_{21}}$: ENERGY SCATTERING

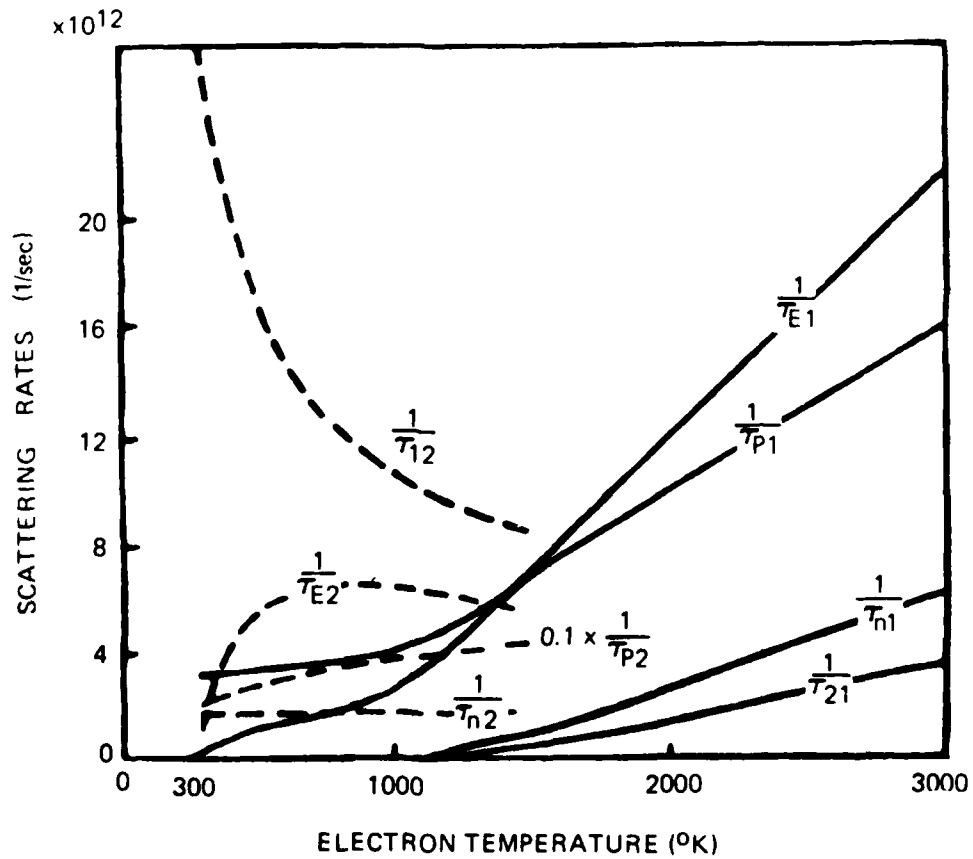


Figure 3. Calculated relaxation frequencies ($1/\tau$) of GaAs versus the respective electron temperature. The symbols are listed in the figure. From Bosch and Thim (1974), with permission.

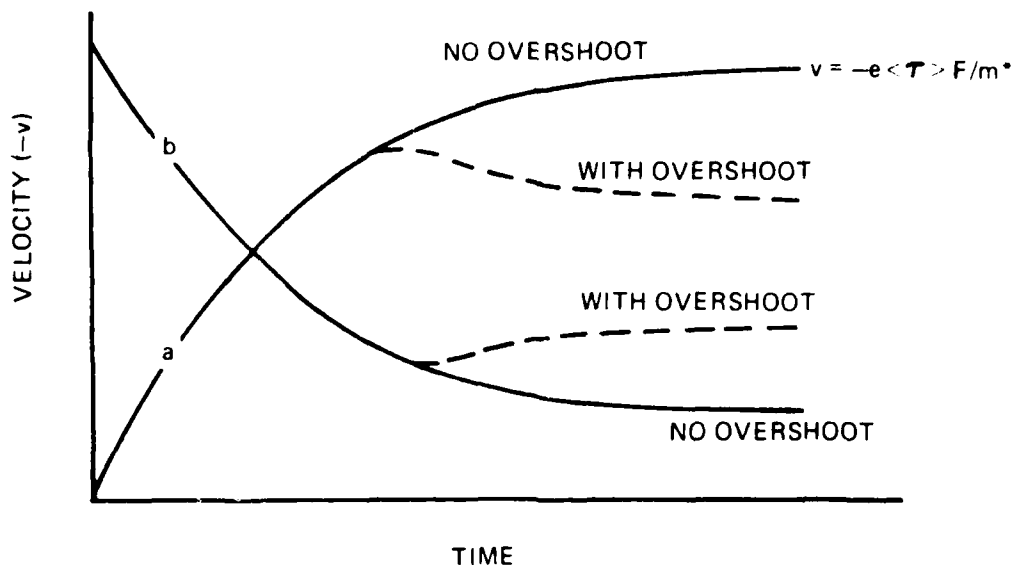


Figure 4. Approach to steady state, with and without transient relaxation effects. Part a denotes increasing velocity and part b denotes decreasing velocity values.

If we were just to consider the momentum balance equation, (2), we could be satisfied that the particles would approach this value in a time approximately equal to $2\langle\tau\rangle$ seconds, as illustrated in Fig. 4. But considering the momentum balance equation alone would give us an incomplete picture of events. Energy balance tells us that the electron temperature increases with increasing electric field and departs significantly from room temperature when the electric field exceeds a threshold value. The effect of the increasing electron temperature is to decrease the average collision time and to decrease the steady-state velocity, given by (5). Now, if the momentum and energy scattering times are similar in value then both momentum and energy will follow changes in electric field at approximately the same rate and the solid curve of Fig. 4 describes the approach to steady-state. On the other hand if the energy scattering time is significantly longer than the momentum scattering time, the average velocity of the carriers will find its value continually 'corrected' until steady state in the energy distribution is reached. The velocity will then relax in the manner shown by the dashed curve. A similar situation may be expected when the electric field is decreased, for here it also takes a finite time for the electric field to decrease and for the electron temperature to decrease.

We may now ask: where do we expect the overshoot transient effects to become significant? On the basis of the above discussion, substantial overshoot effects occur when the momentum scattering time is much shorter than the energy scattering time. Thus we would expect to detect these effects when the time rate of change of electric field falls somewhere within the limits

$$\frac{F_{th}}{\tau_p} \gtrsim \frac{dF}{dt} \gg \frac{F_{th}}{\tau_E} \quad (6)$$

We are interested in the upper bound of the inequality and for this case we take τ_p to be represented by the momentum scattering time for LO intravalley phonons. Intervalley scattering is important as the electron temperature is elevated, and will reduce the momentum scattering time. For LO phonon intravalley scattering (Conwell, 1967),

$$\frac{1}{\tau_p} \approx \frac{F_0 e}{(2m^* k_B T_p)^{1/2}} \quad (7)$$

For the central valley of GaAs, with $F_0 = 5.6 \times 10^3$ V/cm (Butcher, 1967),

$$\frac{1}{\tau_p} \approx 4 \times 10^{12} / \text{sec} \quad (8)$$

which is consistent with the more complete calculations of Fig. 3

($\frac{1}{\tau_{pi}} \approx 3.5 \times 10^{12} / \text{sec}$ for temperatures below 1000 K). Transient overshoot effects are then expected to be significant when the carriers experience changes in the electric field of the order of F_{th} (3kV at the doping levels of $10^{15} / \text{cm}^3$) occurring during a time interval of the order of; or somewhat larger than, τ_p .

In Fig. 5 we show (Rees, 1969) the response of the central valley velocity, the satellite valley velocity, the satellite valley population and the drift velocity, when the electric field is stepped down from 6kV/cm to 5kV/cm. The drift velocity is computed from the equation

$$v = \frac{\frac{n_c v_c + a n_s v_s}{n_c + n_s}}{\quad} \quad (9)$$

For gallium arsenide, the satellite valley scattering times are significantly shorter than the central valley scattering times and so the satellite velocity readjusts itself to the change in electric

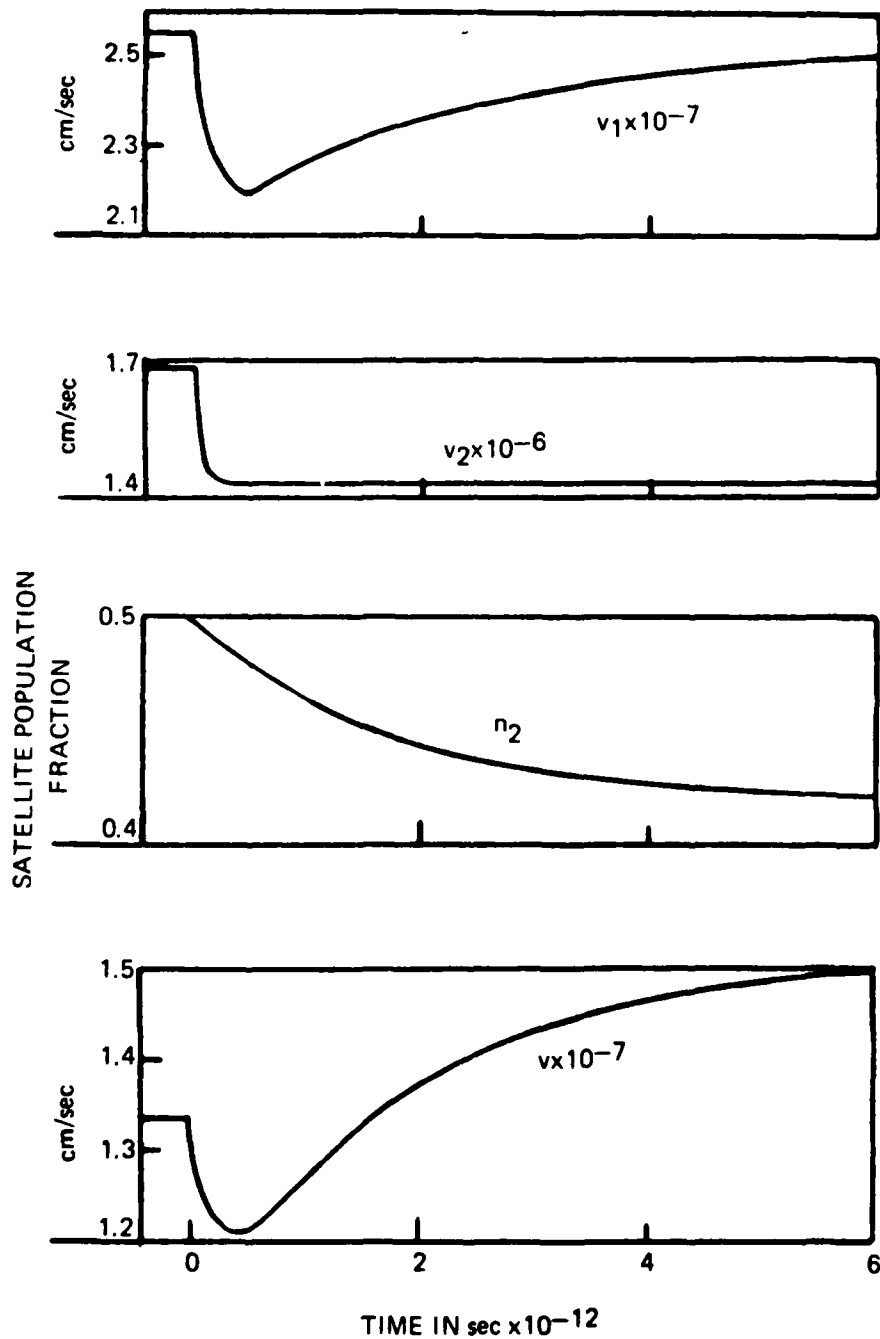


Figure 5. Response time of electrons to a field stepped down from 6 to 5 kV/cm at time $t = 0$. (a) and (b) are respectively the central and satellite valley velocities. (c) is the satellite population fraction. (d) is the drift velocity of the carriers. From Rees (1969) with permission.

field in less than 10^{-13} sec. The central valley velocity takes somewhat longer to reach its minimum value and to then recover. Here v falls for about 4×10^{-13} sec and then begins to recover over a period of approximately 5 picoseconds. The transfer of electrons from the central valley to the satellite valley is also slow. The net response of the drift velocity shows an initial drop due to the central and satellite valley velocities followed by a recovery due partly to the central valley velocity and partly due to differential electron transfer. The final velocity exceeds the initial velocity and illustrates the presence of negative differential mobility.

Transient calculations of the above type are important for determining the conditions under which a material like gallium arsenide will remain an active device. Rees (1969), using the results of Fig. 5, determined the frequency dependence of the differential mobility. These results are shown in Fig. 6. For this calculation, the Fourier transform of the drift velocity was taken, yielding $v(\omega)$. The mobility was defined as the ratio of $v(\omega)/5.5$ kV/cm (for a change from 6kV/cm to 5kV/cm); 5.5 kV/cm is the average of the initial and final values of the electric field. What we notice here, is that the real part of the mobility is *negative* at frequencies below 80 GHz. It is positive above 80 GHz, reflecting the short time response of the central valley electrons.

Spatial Dependence

The above arguments are for uniform fields. We can use this information to estimate the extent to which spatial changes in the electric field will affect the transient response of the carriers. To carry out this argument, we must first calculate the mean free path of electrons injected, with zero initial drift velocity, into a region of high electric field. The mean free path is calculated prior to thermalization assuming a scattering time given by (7). From the momentum balance equation, we have

$$v = p/m^* = -(e\tau_p/m^*)F \left[1 - \exp(-t/\tau_p) \right], \quad (10)$$

and in a time $t = 2\tau_p$, v will have reached approximately 87% of its peak value. During this time the drifting electrons will have travelled a distance

$$l_0 \approx (e\tau_p^2/m^*) F (1 - e^{-2}), \quad (11)$$

before thermalization occurs. We estimate that if the spatial variation in the electric field is such that large changes in the electric

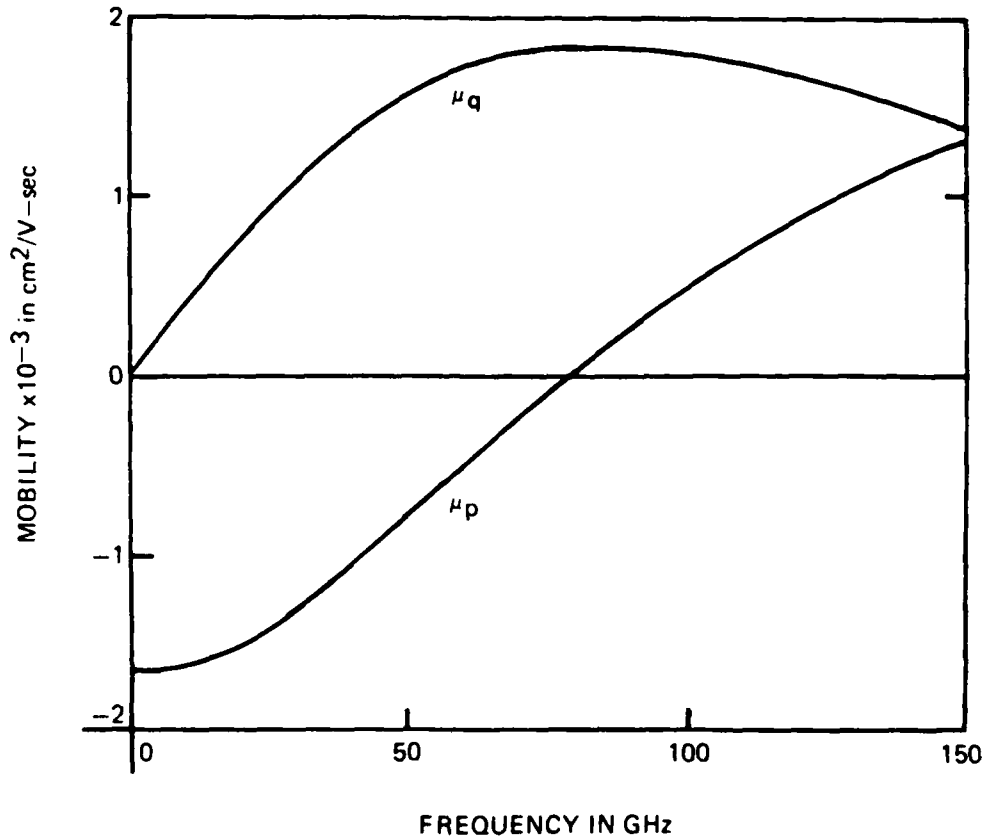


Figure 6. Frequency dependence of the differential mobility for a bias field of 5.5 kV/cm. μ_p and μ_q denotes respectively the components in phase and quadrature with the ac field. From Rees (1969) with permission.

field occur in distances less than that given by (11), then significant relaxation effects may be expected to take place. As an example, for an electric field of 5kV/cm and a cold mobility of 6500cm²/V-sec, electrons in the central valley will have attained a velocity of 2.8x10⁷cm/sec in a time 2 τ_p , and will have travelled a distance of approximately 0.1 microns before the steady state value is reduced by increases in the electron temperature. Figure 7 illustrates this situation (Ferry and Barker, 1979). Here the velocity response of electrons in GaAs is shown for a field of 5kV/cm. These calculations include intervalley transfer and contributions from the satellite valley, for a Γ -L ordering.

The above results suggest that transient overshoot effects will be important when the electric field undergoes a change of the order

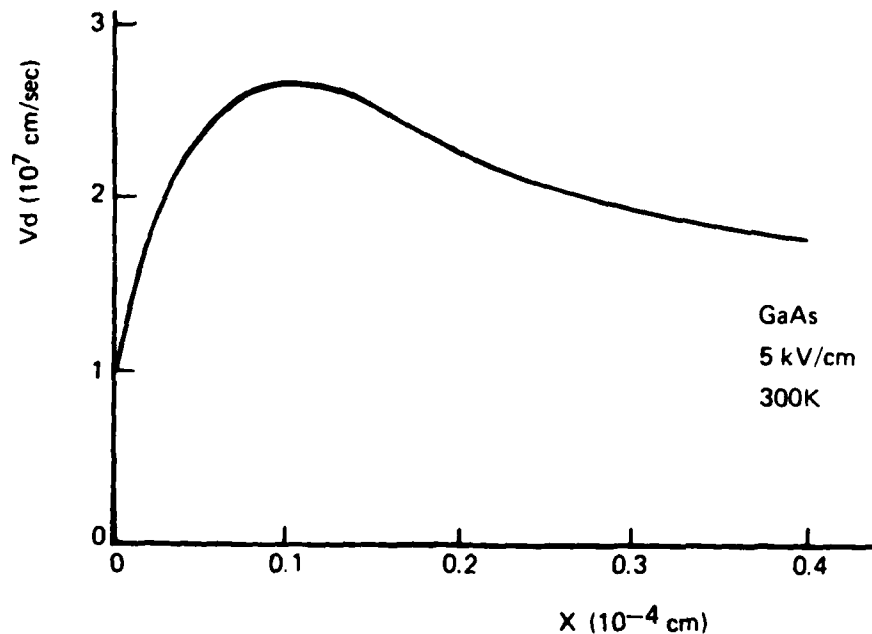


Figure 7. The velocity response of electrons in GaAs for an electric field of 5 kV/cm. From Ferry and Barker (1979), with permission.

of F_{th} (or greater) within a distance of ℓ_0 . In other words overshoot effects will be pronounced when

$$\frac{dF}{dx} \geq \frac{F_{th}}{\ell_0} \quad (12)$$

Using Poisson's equation this can be translated into the condition

$$\frac{N-N_0}{N_0} \geq \frac{\tau}{\tau_p} \quad (13)$$

where τ is the dielectric relaxation time. At $N_0 = 10^{15}/\text{cm}^3$, the right-hand-side of the above equation is equal approximately to 4. Thus, when the ratio of N/N_0 exceeds 5 we may expect relaxation effects to enter in an important way. In an early discussion, Butcher, *et al.*, (1967) estimated the maximum value of N/N_0 for the accumulation portion of a stable travelling domain. As is well

known from domain theory, as the outside field begins to decrease the domain increases in size and the accumulation portion of the domain increases dramatically. Butcher, *et al.*, (1967) found that when the outside field is below 2kV/cm, the accumulation ratio exceeds 5, and that for outside fields approaching the sustaining field the ratio is substantially higher. The implication is that a sizable portion of the accumulation layer is not accurately modeled by steady-state velocity-electric-field relationships. Rather, transient effects must be included for a complete picture. The degree to which this particular transient contribution will affect the output at the terminals of device has not yet been determined.

As we go to higher carrier concentrations, τ decreases and the criteria expressed by (13) becomes more restrictive. For example at 10^{17} cm^{-3} , accumulation layers in excess of 4% of N_0 will introduce significant relaxation effects.

Relaxation Effects Within a Travelling Accumulation Layer: The

Jones-Rees Effect

The discussion above for nonuniform fields was based on concepts derived from a uniform field analysis. While this approach is useful for estimating some of the relaxation contributions, it is not wholly satisfying. Jones and Rees (1973) have examined some of these limitations. For this discussion, we refer to the accumulation layer profile sketched in Fig. 8.

The accumulation layer profile consists of two regions, a high-field and a low-field region separated by a region of substantial charge accumulation. The downstream portion of the accumulation layer consists mainly of satellite electrons. In analyzing the propagation of the accumulation layer, Jones and Rees (1973) observed a phenomena that appeared in all of their simulations. The fall of the satellite electron density from the high-field region to the low-field region was quite sharp. This behavior was not expected. In the spatially uniform analysis in which the field decreased rapidly to a value below threshold, a large fraction of the satellite electrons was initially retained. About 5-10 psec was required for their thermalization (see Fig. 5). Since the layer velocity in their computer simulations was above the satellite electron velocity, a long trailing edge of satellite electrons was expected. But in fact this did not occur. Rather a time constant of the order of 1 psec represented the rate of transfer. The mechanism proposed by Jones and Rees (1973) to explain the differences between the relaxation time for uniform fields and nonuniform fields is described below.

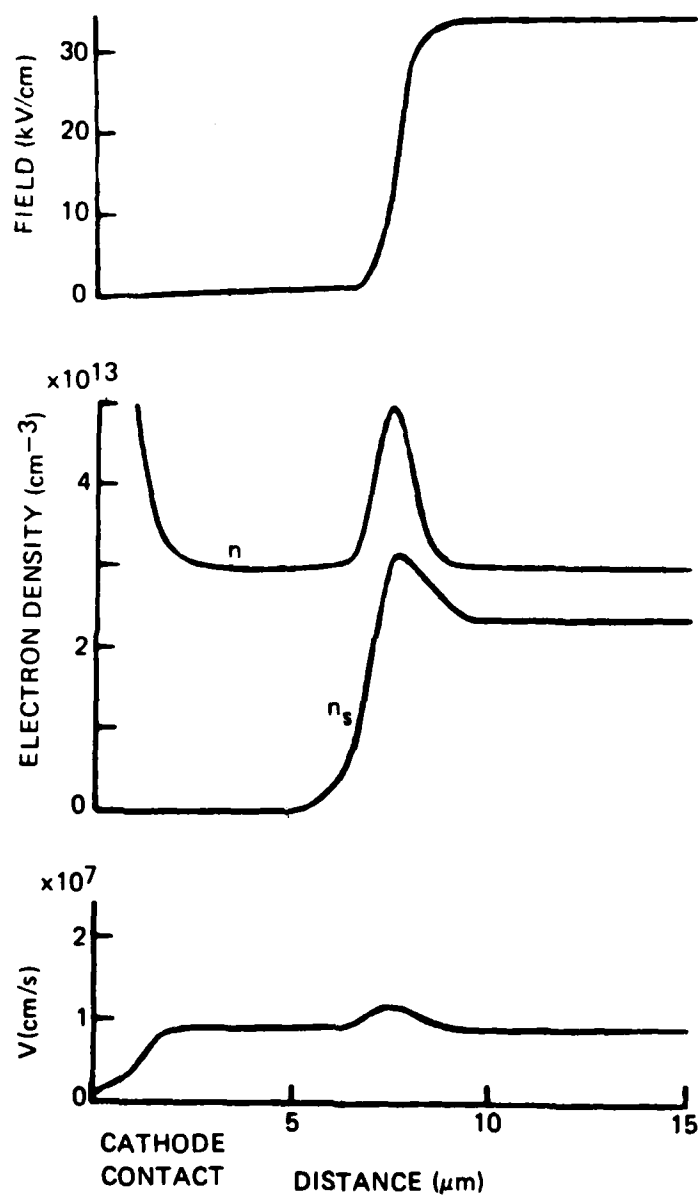


Figure 8. Profiles of electric field, total electron density and satellite valley density, and drift velocity for a mature propagating domain. From Jones and Rees (1973) with permission.

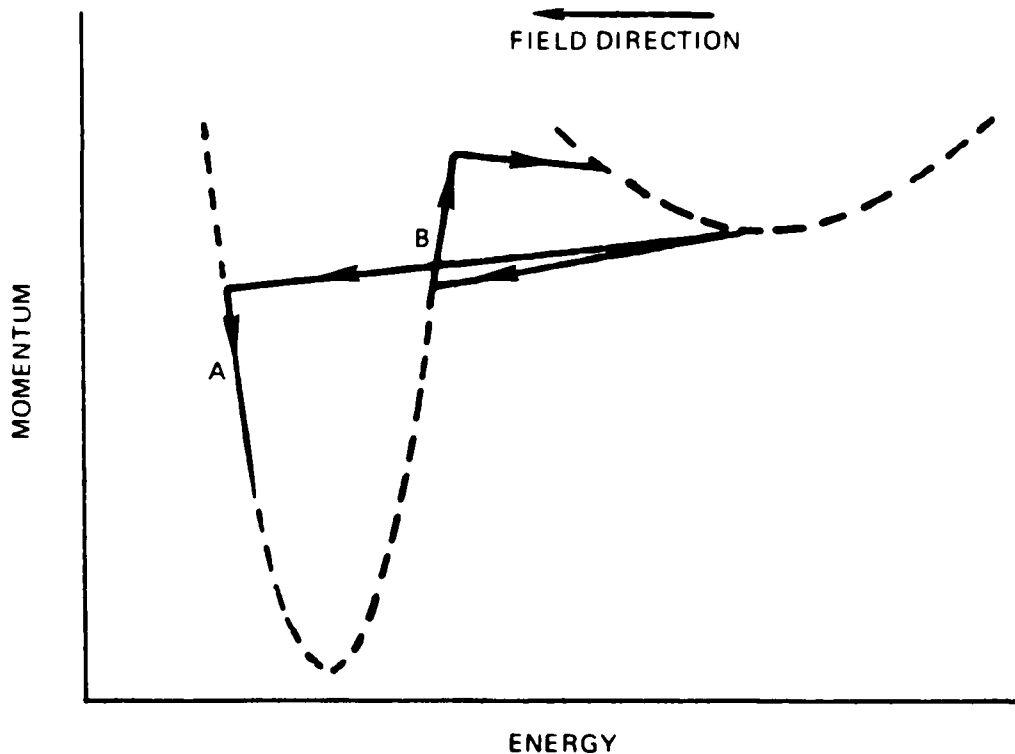


Figure 9. k-space representation of carrier cooling behind an accumulation layer. 'A' electrons scattered to Γ valley-backward momenta states lose energy and fall behind the layer. 'B' electrons scattered to Γ valley-forward momenta states gain energy and remain within the layer.

Figure 9 illustrates possible k-space trajectories for electrons initially within the layer. We will assume, for illustrative purposes, that the electrons are initially occupying the satellite valley states. These electrons rapidly scatter between the satellite and central valley states with high energy and momenta. Some of these electrons will scatter into k-states whose direction is opposite to that of the moving distribution. Those scattered electrons will lose energy and will not scatter back into the satellite valley. They are then concentrated behind the accumulation layer and account for the lower satellite valley population. In contrast, electrons scattered to high forward momenta states gain energy from the field and are concentrated in the front of the

accumulation layer. At least part of the propagating accumulation layer is due to this scattering mechanism. Thus the traveling accumulation layer segregates the electrons into two classes and, in leaving a cold distribution behind the layer, it overrides the tendency to leave electrons heated, which characterizes a rapid fall of field in a spatially uniform distribution.

CONCLUSIONS

In the above, I have outlined several hot electron transient effects in transferred electron device. As of this writing, it is not at all clear what role these specific effects will have on the operation and output of small electron devices. What is clear is that it is incorrect to try to discuss the behavior of very-small, highly-doped devices without examining transient relaxation phenomena.

BIBLIOGRAPHY

- Bosch, R., and Thim, H.W., 1974, IEEE Trans. Electron Dev. ED-21:16.
Butcher, P., 1967, Repts. Progr. Phys. 30:97.
Butcher, P.N., Fawcett, W., and Ogg, N.R., 1967, Br. J. Appl. Phys. 18:755.
Conwell, E.M., 1967, "High Field Transport in Semiconductors," Academic Press, New York. We use here (3.623) with the assumptions $\hbar\omega \approx k_0T_p$ and $\epsilon = m^*V^2/2 < k_0T_p$. Note the comment following (3.623) that the scattering time does not represent a relaxation time. In our discussion, we nevertheless use τ_p for intravalley optical scattering as though it were a relaxation time.
Ferry, D.K., and Barker, J.R., 1979, Sol.-State Electr., in press.
Gunn, J.B., 1964a, IBM J. Res. Develop. 8:141.
Gunn, J.B., 1964b, in "Proc. 7th Intern. Conf. Phys. Semiconductors," Dunod Cie., Paris, p. 199.
Hilsum, C., 1962, Proc. IRE 50:185.
Jones, D., and Rees, H.D., 1973, J. Phys. C. 6:1781.
Kroemer, H., 1964, Proc. IEEE 52:1736.
Rees, H.D., 1969, IBM J. Res. Develop. 13:537.
Ridley, B.K., 1963, Proc. Phys. Soc. (London) 82:954.
Ridley, B.K. and Watkins, T.B., 1961, Proc. Phys. Soc. (London) 78:293.

Switching Characteristics of Nonlinear Field-Effect Transistors: Gallium-Arsenide Versus Silicon

H. L. GRUBIN, MEMBER, IEEE

Abstract—A study of the switching properties of GaAs FET's and other nonlinear elements whose high field velocity saturates without negative differential mobility demonstrates that the high-bias switching times of GaAs are determined by velocity saturation. Silicon switches are also studied, and situations where GaAs and Si switching properties may be similar are discussed.

I. INTRODUCTION

THE SEMICONDUCTOR gallium-arsenide is a widely used field-effect transistor material. It is an unusual one in that it possesses a region of negative differential mobility (NDM) and two characteristic velocities: a peak velocity prior to the onset of NDM and a saturated drift velocity following the NDM region. The effects of NDM are currently being mapped out and it is developing that NDM separates devices into two categories: those that sustain spontaneous oscillations and those that do not [1]. Devices sustaining spontaneous oscillations, whose origin is due to transiting and recycling space charge layers, generally have cutoff voltages greater than the drain-voltage value at the onset of current saturation. Those that do not, possess cutoff voltages approximately equal to saturation drain voltage. The latter often yield low power and are useful as switching devices. In the last few years there has been an increasing interest in GaAs switches for integrated circuit applications. The advantages for gallium-arsenide are thought to be very high speeds and low-power-delay products. The purpose of this study is to examine these conclusions, and in doing so we highlight the roles that the low field mobility and the high field saturated drift velocity have on the switching times. To place the results in perspective we do similar calculations for the semiconductor silicon.

II. NUMERICAL SIMULATION MODELING

The switching calculations discussed below are for four different elements, including silicon. For the GaAs FET we examine only those devices that do not sustain spontaneous oscillations. To highlight the importance of the high

Manuscript received July 24, 1979; revised February 15, 1979. This work was supported by the Office of Naval Research.

The author is with the United Technologies Research Center, East Hartford, CT 06108.

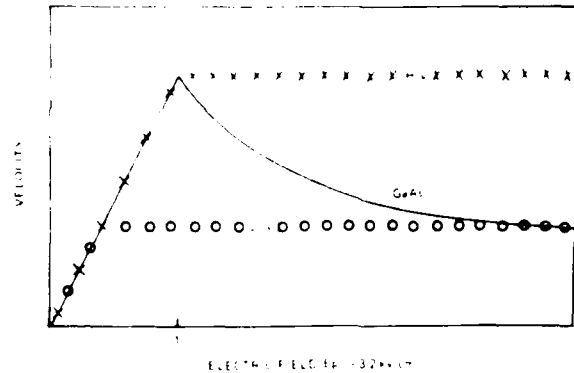


Fig. 1. Drift velocity versus electric-field relation used in the calculations. The gallium-arsenide results are taken from [7, fig. 3].

field drift-velocity values we also present results of calculations with nonlinear elements whose low field mobility is equal to that of gallium-arsenide but whose high field velocity saturates without NDM. In one case the drift velocity saturates to the saturated drift velocity of gallium-arsenide. In the second case it saturates to the peak velocity. The velocity electric-field characteristics for these calculations are displayed in Fig. 1, where we designate the high-saturated drift-velocity element HiV , and the lower saturated drift-velocity element LoV .

The calculations with the LoV and HiV elements are more than academic. It is now generally agreed that these nonlinear elements lead to dipole formation within the gate to drain region [2], [3] and that at large values of bias the electrons within this region are traveling at their saturated drift-velocity values. If this is the case then it has been argued that the saturated drift velocity is the primary factor at high-bias levels for determining the switching speeds.

In the following calculation we use an already developed [4] large-signal numerical simulation designed to determine the transient behavior of nonlinear semiconducting FET's. The simulation results in self-consistent solutions to Poisson's equation, the equation of continuity and the external circuit equations. The solutions are for two dimensions plus time with the electrons described by a specific drift velocity versus electric-field curve shown in Fig. 1 and a diffusion electric-field curve shown in Fig. 2.

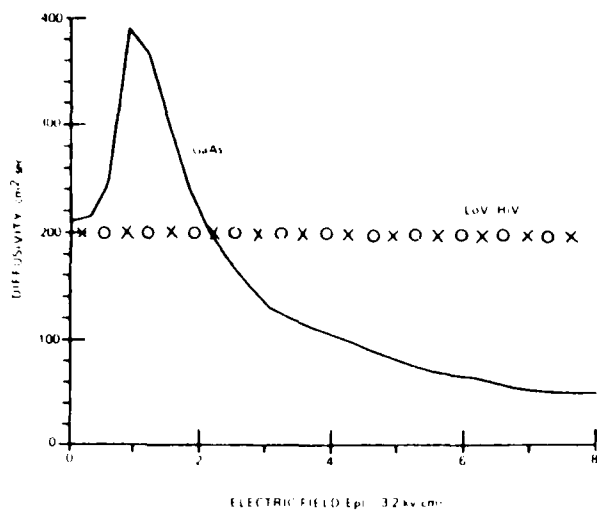


Fig. 2. Diffusivity versus electric field used in the calculations. The gallium-arsenide results are taken from [7, fig. 4].

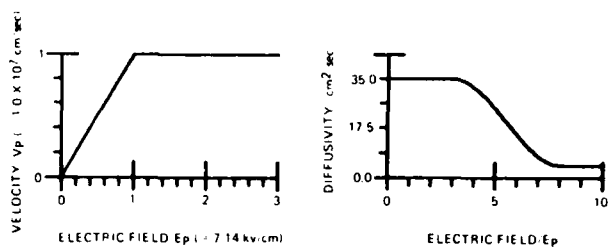


Fig. 3. Silicon parameters used in the calculation. The parameters are adapted from [5].

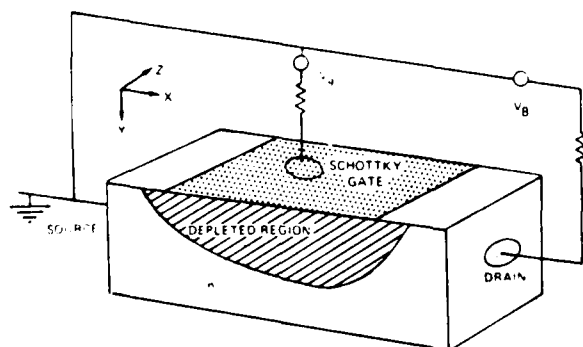


Fig. 4. Schematic representation of a Schottky gate field-effect transistor.

For the silicon calculations the velocity and diffusion field curves [5] are shown in Fig. 3.

The FET device circuit configuration is shown in Fig. 4 and the bulk of our calculations are for $N_0 = 10^{15}/\text{cm}^3$, with the exception of silicon, for which the calculations were done at $5 \times 10^{15}/\text{cm}^3$. The reason for this difference is discussed below. With regard to Fig. 4 we note that placement of the source and drain regions. In this configuration we concentrate on the physics associated with the space charge and avoid effects due to the geometrical

placement of the contacts. The length of the device chosen for the GaAs, LoV, and HiV calculations was $10 \mu\text{m}$.

The silicon parameters, which were different from those of the other three elements, were chosen in a way to make the environment as represented by the semiconductor equations, similar for electrons in gallium-arsenide and silicon. For this we concentrated on the equation for total current density for the carriers in the FET:

$$j = NeM\vec{E} + eD \text{grad}_x N + \epsilon \frac{\partial \vec{E}}{\partial t} \quad (1)$$

where M is the field dependent mobility ($|\vec{V}|/|\vec{E}|$) and D is the field dependent diffusivity, $N(X, Y, T)$ is the mobile carrier density and $\vec{E}(X, Y, T)$ the electric field, ϵ is the permittivity. We normalize [6] (1), writing it as

$$j = \frac{j}{N_0 e V_p} = n\mu \xi + \left(\frac{L_D}{L_0}\right)^2 \text{grad}_x n + \frac{\partial \xi}{\partial t} \quad (2)$$

where $t = T/\tau$, $\xi = X/L_0$, $\xi = E/E_p$, $\mu = M/M_0$, $L_0 = V_p \tau$, $n = N/N_0$, and

$$L_D = (D\tau)^{1/2} \quad (3)$$

which is a field dependent Debye length. τ is the dielectric relaxation time. At low values of electric field and for a doping level of $10^{15}/\text{cm}^3$, L_D is approximately equal to $0.14 \mu\text{m}$ for GaAs. Also, in (2), V_p is the peak electron velocity, which for GaAs is approximately $2.2 \times 10^7 \text{ cm/s}$ at $10^{15}/\text{cm}^3$, M_0 is the low field mobility, and E_p is the field at V_p . In our simulations we chose the ratio L_D/L_0 to be the same for GaAs and silicon. For this case, at least at low fields, the carriers would find the different semiconductor equations indistinguishable. Differences will occur at high bias levels where the effects of NDM and velocity saturation come into play.

If we use the Einstein relation $D = M_0 k_0 T_0 / e$ then the ratio $(L_D/L_0)^2$ is

$$\left(\frac{L_D}{L_0}\right)^2 = \frac{k_0 T_0}{\epsilon} \frac{N_0}{E_p^2} \quad (4)$$

and for GaAs at $N_0 = 10^{15}$, $E_p = 3.25 \times 10^3 \text{ V/cm}$, silicon with $N_0 = 5 \times 10^{15}/\text{cm}^3$, and $E_p = 7.14 \times 10^7 \text{ V/cm}$ we find

$$\left(\frac{L_D}{L_0}\right)^2 \frac{\epsilon}{k_0 T_0} = \begin{cases} 0.95 \times 10^8 / \text{V}^2 \cdot \text{cm} & \text{for GaAs} \\ 0.98 \times 10^8 / \text{V}^2 \cdot \text{cm} & \text{for Si} \end{cases} \quad (5)$$

We use these parameters in the simulation.

The normalization associated with (2) is an intrinsic normalization. But the equation for current flow is also subject to boundary condition at the source and the drain contact. To give the carriers the impression that the normalized sample lengths are the same it is necessary to require that the ratio L_{SD}/L_0 be the same for the silicon and gallium-arsenide device. (L_{SD} is the source-to-drain

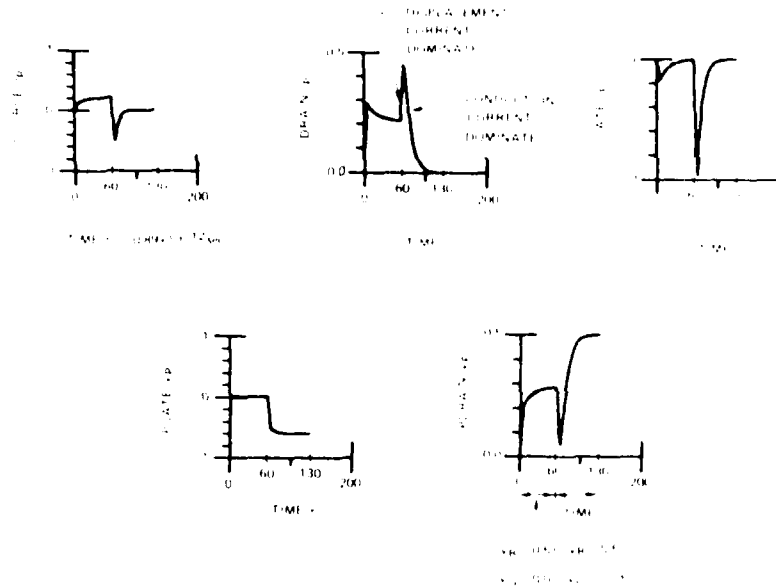


Fig. 5. Time evolution of the current and potential at the three contact for the GaAs FET. The normalization scheme is indicated in the test. Time is in multiples of the dielectric relaxation time

separation.) The ratio L_{SD}/L_0 is equal to

$$\frac{L_{SD}}{L_0} = \frac{L_{SD}}{V_p \tau} = \frac{L_{SD} N_0}{E_p} \left(\frac{e}{\epsilon} \right) \quad (6)$$

and in the simulation we have chosen $L_{SD} = 4.4 \mu\text{m}$ for silicon.

III. ILLUSTRATIVE CALCULATIONS

We begin the discussion with the gallium-arsenide element. The output of the simulation is illustrated in the next few figures. In Fig. 5 we display the evolution of the current at the three contacts and the potential at the gate and drain contacts for the situation where, at first the drain bias is increased to $0.5 v_p$ ($v_p = E_p L_{SD}$) and the gate bias is zero. For the second stage the gate bias is decreased relative to ground to the value $-0.6 v_p$. The bias changes at a finite rate to the values indicated in the figures. The sign conventions are as follows: positive source current denotes current flow into the device through the source contact; positive gate current denotes current flow out of the device through the gate contact; positive drain current denotes current flows out of the device through the drain contact. Thus from Fig. 5 an increase in drain bias results in an increase in drain and source current, with more current leaving the device through the drain current than entering through the source contact. There is a large displacement current with carriers building up on the gate contact. After the initial transient there is a significant conduction current contribution associated with the physical movement of the gate-depletion region until the steady state is reached. The subsequent decrease in gate bias from 0 to $-0.6 v_p$ results in an increase in potential on the drain contact. There is a further buildup of charge on the gate contact and a

movement of the depletion layer to the bottom of the device. This effectively cuts off the current flow out of the drain contact. The switching times are estimated from Fig. 5, and in going to the off-state are equal to the magnitude of the difference between the time of initial relaxation and the time at which the drain current reaches a negligible value.

The internal distribution of charge and current associated with the current and potential levels of Fig. 5 is shown in Fig. 6. In Fig. 6(a) we display a set of current density streamlines through the device. The length of each streamline is proportional to the magnitude of the vector current density at the point in question. The maximum length of the individual x and y component before overlap is $J_p = N_0 e V_p$. For the stationary state at 60τ s in Fig. 5 we see the current density to be greatest under the gate contact as required by current continuity. In Fig. 6(b) we show the current density for the situation where the drain current has been reduced to zero by virtue of the gate bias being set equal to $-0.6 v_p$. For these GaAs calculations $v_p = 3.2$ V. The density of charged particles within the device is generally nonuniform and Figs. 6(c) and (d) are projections of this distribution. We point out that the particle density increases in the downward direction, and we see the presence of the depletion layer. The position of the gate for these calculations are indicated.

Quantitative estimates of the particle density and potential for the steady-state case at 60τ s are illustrated in Fig. 7, where we display contour plots of these quantities. We note that most of the potential drop is under the gate contact. It is clear that the potential difference between the contours $0.105 v_p$ and $0.210 v_p$ are insufficient for the field to reach the threshold for NDM.

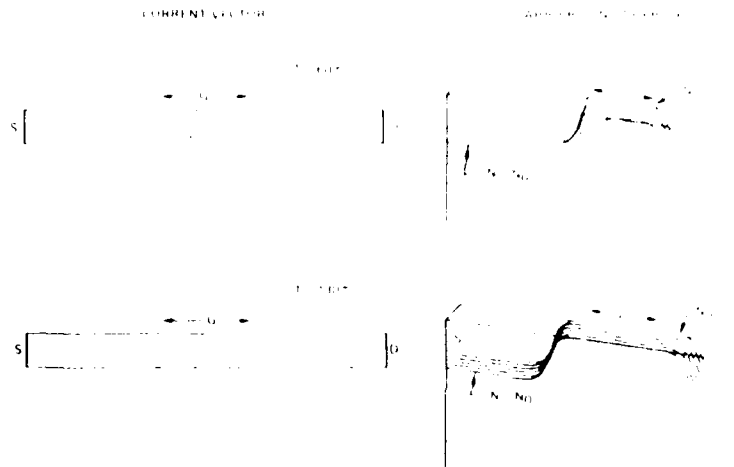


Fig. 6. The internal distribution of current and charge for the parameters of Fig. 5. The time is keyed to the computations of Fig. 5.

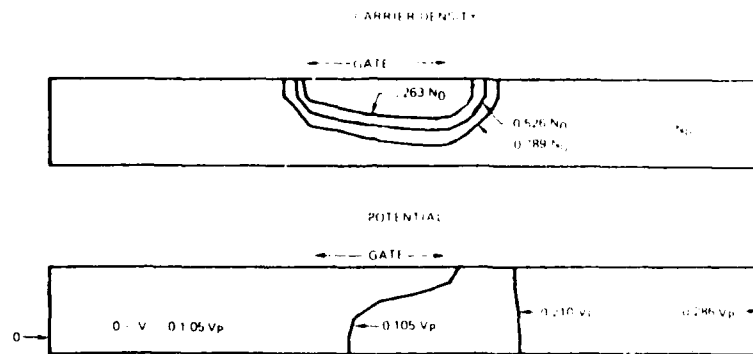


Fig. 7. Contours of charge density and potential for the 60τ s. Calculation of Fig. 5.

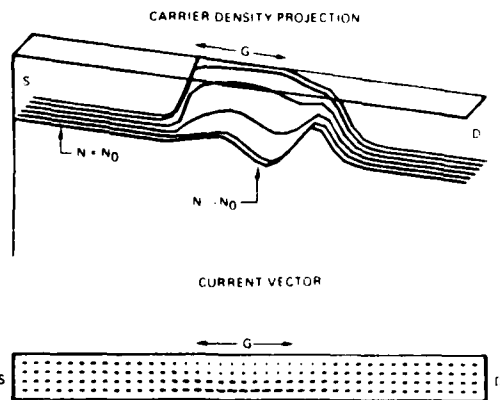


Fig. 8. Internal distribution of charge and current density for the situation where a dipole layer forms under the gate contact. Here $v_p = 1.0v_p$ and $v_G = 0.0$.

An increase in drain bias to v_p results in an increase in potential on the drain contact and a moderate increase in drain current. We are into current saturation. A dipole forms and grows under the gate contact, but there is no current instability. For a $10\text{-}\mu\text{m}$ long device there is about $2\text{ }\mu\text{m}$ of the device within the NDM region. Fig. 8

illustrates with the carrier density projection and current-density vector display. Fig. 9 illustrates with contour plots of potential and carrier density. We have also estimated the average field between the contours of constant potential and find that at the drain side of the gate contact the field exceeds the threshold field for negative differential mobility. The values are indicated in the figure.

As indicated in the introduction, calculations with materials with high field saturated drift velocities also show dipole formation. Fig. 10 illustrates this for silicon, where we show the contour plots of carrier density and potential. The average field under the gate is seen to exceed the critical field of 7 kV/cm . We also show the vector current density display. Here the lines begin to overlap when the current density exceeds $N_0 e V_p$, with V_p equal to $1.0 \times 10^7\text{ cm/s}$.

IV. SWITCHING CALCULATIONS

The above discussion presented the distribution of charge, potential, and current within a device. We next compute the switching properties of the device. We begin by presenting the current-voltage characteristics under zero gate bias conditions for the four simulated elements.

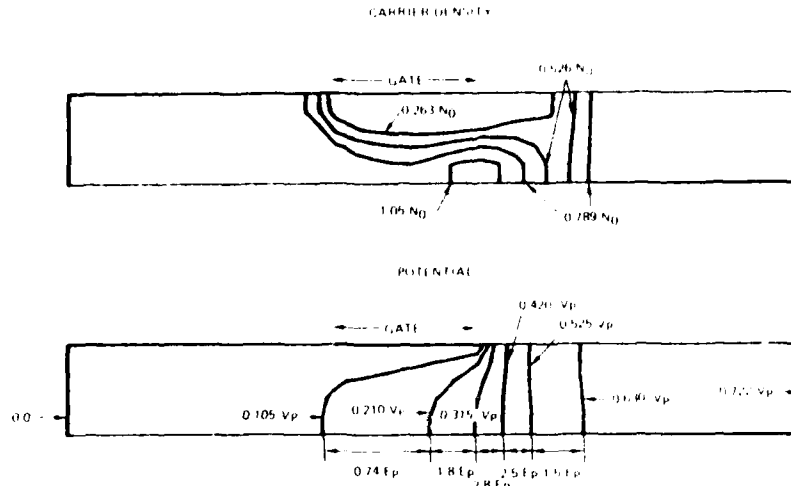


Fig. 9. Carrier density and potential contours for the calculation of Fig. 8. Also shown are estimate of the field between the contours.

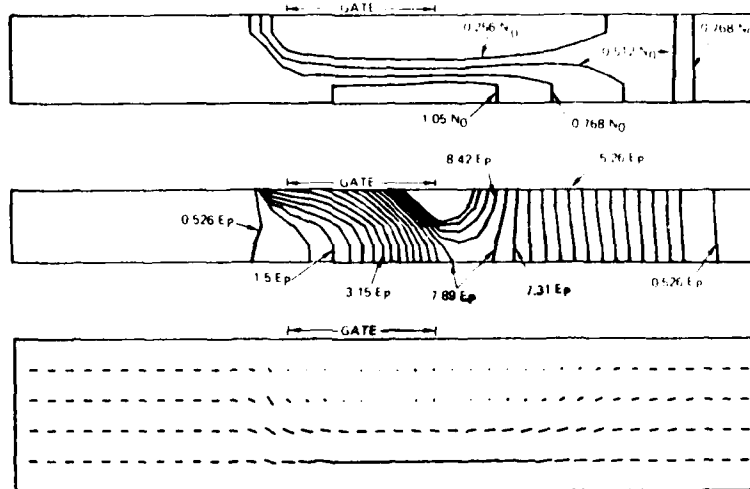


Fig. 10. Contours of carrier density, electric field, and current vector for a three-terminal silicon element showing the presence of a dipole layer under the gate. Here $v_g = 3.0v_p$, $v_c = 0.0$. The peak field at the bottom of the channel occurs between the $7.89E_p$ contours.

This is displayed in Fig. 11. The current-voltage relation for each element is normalized to I_p and v_p , where $I_p = N_0 e v_p A$ and $v_p = E_p L$. (A is the cross-sectional area in the Y - Z plane.) We note that the simulated points for GaAs are bracketed by those of HiV and LoV, while those for silicon are approximately equal to that for HiV.

In our calculations switching takes place between a point I_D, v_D at zero gate bias and a second point at a level of zero drain current. Both points lie on a dc load line. In the switching process an amount of energy

$$\delta W = \int_{T_1}^{T_2} v_D(T) I_D(T) dT \quad (7)$$

is transferred. We estimate δW by the power-delay product $(I_D v_D) (T_2 - T_1)$.

The results in Fig. 12 show the power-delay product for four elements with a load $R = R_0$, where R_0 is the characteristic resistance of each of the elements. We also show

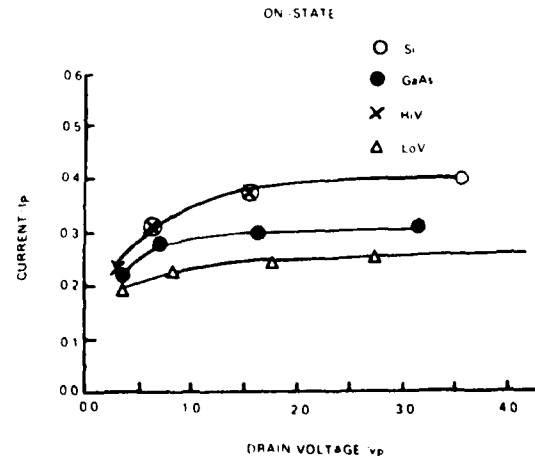


Fig. 11. On-state current-voltage relation for the four elements. Note $v_p = 3.2$ V for GaAs, LoV, and HiV. $v_p = 3.1$ V for silicon.

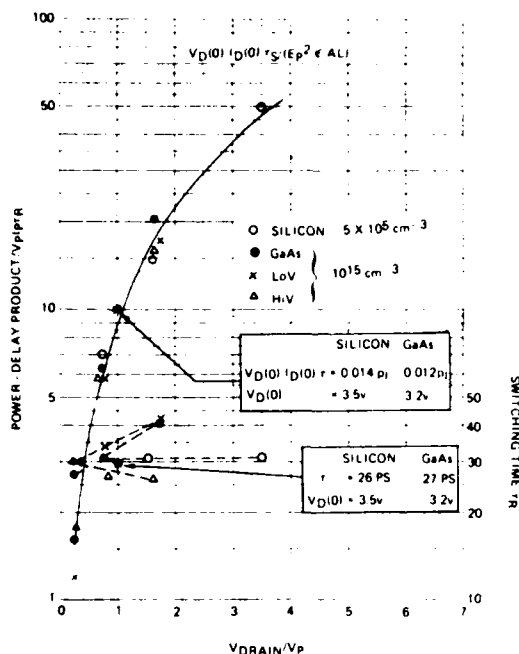


Fig. 12. Normalized power-delay product and normalized switching times versus normalized drain voltage for the four elements used in the calculation.

the switching times normalized to the dielectric relaxation time. Perhaps the most significant feature of this calculation is that GaAs, LoV, HiV, and the scaled silicon device all appear to have similar normalized characteristics as far as (7) is concerned. The differences appear in the normalized switching times, with the HiV being the fastest.

In examining these switching results two extreme situations should be considered: low- and high-bias levels. At the high-bias end the GaAs and LoV element show similar behavior, with both elements displaying longer delay times than that of HiV. This result provides strong evidence that saturation in the drift velocity of GaAs is the principle determinant of its high-bias switching speed. With regard to the scaled silicon device, its switching times and power delay product are similar to that of HiV, an element whose mobility is better than four times higher, and whose velocity at saturation is 2.2 times higher. In our calculations the high-bias switching times appear to be determined by the ratio \hat{L}/V_{sat} , where \hat{L} represents the length of the high field region. The silicon device has a gate-to-drain spacing that is approximately 1/2 that of HiV, which may account for the similar switching times.

At low-bias levels we may expect the switching properties to be adequately represented by the Shockley analysis [8] in which case the switching times are proportional to [8], [9] $\tau (L/a)^2$ where a is the channel height and τ is the dielectric relaxation time. This result teaches that materials with different mobilities can yield similar delay times, provided their "aspect" ratios and their dielectric relaxation times are similar. The scaling associated with (1)-(6) resulted in comparable values of τ and L/a for all four

nonlinear elements. Thus the low-bias switching speeds of all elements should be similar.

Generally, the net switching time of any bias level is composed of several contributions including transit and dielectric relaxation times, parasitic and dissipative load-time constants. It would appear that if the high-bias switching times are determined by velocity saturation and transit through high field regions, then so long as τ is less than the transit time, the value of the doping level will be important only insofar as it influences the field distribution and breakdown conditions. On the other hand, at low-bias levels the switching times will be more sensitive to doping as indicated in the above paragraph.

The above discussion clearly suggests that at high-bias levels similarly designed silicon and gallium FET switches should yield comparable delay times. There are, however, limits to which this result is valid. Continual reduction in the active region length to achieve shorter switching times, will begin to lead to nonequilibrium transient behavior. These transient effects lead to higher transient velocities in gallium-arsenide than in silicon, which should result in shorter switching times for the former. At low-bias levels, but for similar doping, silicon should yield a delay time longer than that of GaAs by the ratio of their mobilities. At intermediate bias levels GaAs should generally be faster than silicon.

With regard to the power-delay product in Fig. 12, it is normalized to the quantity

$$I_p v_p \tau = E_p^2 \epsilon L_x L_y L_z \quad (8)$$

Now for gallium-arsenide with $L_x = 10 \mu\text{m}$ and $L_y = 1.21 \mu\text{m}$

$$I_p v_p \tau = 1.28 \epsilon L_z \quad (\text{GaAs}) \quad (9)$$

For the scaling scheme we have used for silicon, with $L_x = 4.4 \mu\text{m}$ and $L_y = 0.536 \mu\text{m}$, the normalized products are approximately the same:

$$I_p v_p \tau = 1.20 \epsilon L_z \quad (\text{silicon}) \quad (10)$$

Thus for a device whose width is $L_z = 10 \mu\text{m}$, there is a power-delay product, at a normalized drain potential of v_p that for both is approximately equal to 0.012 pJ as indicated in Fig. 12. We note, however that for a silicon and GaAs switch of similar doping and dimensions, low-bias level switching should lead to higher power-delay products for silicon. At bias levels well into saturation they should be more nearly similar.

A recent compilation of data by Greiling [10] on similarly designed GaAs and Si switches shows silicon to have (low-bias) delay times six times longer than that for GaAs. At high-bias levels the switching times of both reflected the fact that the high field carriers were into velocity saturation. Further, at the high-bias levels GaAs was only within a factor of two faster than silicon.

V. CONCLUSIONS

The purpose of this study was to examine some of the switching properties of GaAs FET's and to compare them to silicon FET's. The results demonstrate that at high-bias levels the delay time of GaAs is determined by velocity saturation. Further so long as nonequilibrium effects may

be ignored, switching speeds for GaAs and silicon will be similar for comparably designed structures operated at high-bias levels. (This latter conclusion ignores differences in parasitic contributions.) At low-bias levels, scaling principles indicate the silicon delay times will be longer than those of gallium-arsenide by the ratio of their mobilities. Intermediate fields will result in shorter delay times for gallium-arsenide.

REFERENCES

- [1] H. L. Grubin, D. K. Ferry, and K. R. Gleason, *Solid-State Electron.*, vol. 23, p. 157, 1980.
- [2] D. P. Kennedy and R. R. O'Brien, *IBM J. Res. Develop.*, vol. 14, p. 95, 1970.
- [3] H. L. Grubin in *Proc. Sixth Biennial Cornell Elect. Eng. Conf.*, (Cornell University, Ithaca, NY), p. 399, 1977.
- [4] H. L. Grubin and T. M. McHugh, *Solid-State Electron.*, vol. 21, p. 69, 1978.
- [5] C. Jacaboni, C. Canali, G. Ottaviani, and A. Albergigi Quaranta, *Solid-State Electron.*, vol. 20, p. 77, 1977.
- [6] B. W. Knight and G. A. Peterson, *Phys. Rev.*, vol. 155, p. 393, 1967.
- [7] P. N. Butcher, *Rep. Progr. Phys.*, vol. 30, p. 97, 1967.
- [8] W. Shockley, *Proc. IRE*, vol. 40, p. 1365, 1952.
- [9] G. C. Dacey and I. M. Ross, *Bell Syst. Tech. J.*, vol. 34, p. 1149, 1955.
- [10] P. Greiling, private communication.

SPONTANEOUS OSCILLATIONS IN GALLIUM ARSENIDE FIELD EFFECT TRANSISTORS

H. L. GRUBIN

United Technologies Research Center, East Hartford, CT 06108, U.S.A.

D. K. FERRY

Colorado State University, Fort Collins, CO 80521, U.S.A.

and

K. R. GLEASON†

Naval Research Laboratory, Washington, DC 20375, U.S.A.

(Received 19 February 1979; in revised form 19 May 1979)

Abstract—We present results of experiments and numerical simulations designed to reveal the presence of spontaneous oscillations arising from negative differential mobility effects in gallium arsenide field effect transistors. The measurements include d.c. and pulsed current/voltage vs temperature characterization, sampling scope measurements, spectral analysis to 40 GHz and observation of light emission. The simulation is a time dependent large signal transient analysis arising from a fully two-dimensional solution of the self-consistent potential and charge within the device.

1. INTRODUCTION

The gallium arsenide field effect transistor has been around a long time [1, 2] showing promise of delivering high power while sustaining low noise levels. GaAs is, however, subject to hot electron effects that manifest themselves in the presence of highly nonuniform charge layers or "domains". And depending on device size and bias values, these domains are either trapped near the gate or drain contacts [3], or propagate between them.

The presence of trapped high field domains is expected to profoundly affect FET performance and is currently subject to much study [4-6]. However, with the exception of early empirical studies [2, 7] and recent numerical studies [3, 8, 10], the dynamic properties of the propagating domain, the conditions for their existence, and their influence on device performance has until recently [11-14] been largely ignored. The renewed interest arises from a need to determine the extent to which the occurrence of spontaneous oscillations in GaAs FETs [11-14] are a consequence of negative differential mobility (NDM). In the following we discuss the influence of trapped and propagating domains on FET operation. We also present evidence for the *highly probable* conclusion that the propagating domain is the origin of our observation of spontaneous oscillations in GaAs FETs.

The study reported here is in two parts: (i) numerical simulation and (ii) experiment. The numerical studies reveal the presence of *two qualitatively different trapped domains* and one traveling domain. The first trapped domain forms within the conducting channel and at the drain edge of the gate contact. [4-6]. Its formation is a direct consequence of velocity limitation in GaAs and its presence is responsible for current saturation at values of drain voltage significantly below that predicted by

Shockley [15]. The second trapped domain is qualitatively different and *forms in FETs capable of sustaining a current instability arising from (NDM)*. This domain forms *near the drain contact, at high drain and low gate bias levels and is coincident with the cessation of oscillatory activity in GaAs FETs*. (The extent to which it is removed from the gate region depends on the gate to drain spacing and the doping concentration of the epitaxial region.) The domain is qualitatively similar to the *high anode field* configuration in two terminal devices, where it is also responsible, in many cases, for the cessation of oscillation [16]. Each of the low and high drain bias trapped domains may pulsate in time and so enhance the noise existent in the FET. In the case of the traveling domain, it, as for some transferred electron logic devices (TELD) is launched at the drain side of the gate contact, propagates to the drain contact and then recycles successively. While the traveling domain need not be "stable" in the sense of two terminal NDM devices [16], its threshold and quenching conditions are similar to that for two terminal devices [3, 8].

The experimental studies reported below consist of pulsed and d.c. measurements performed as a function of temperature and under different circuit conditions. We have determined the spectral content of the oscillations when they occurred, and for pulsed measurements have sampled the current and voltage at different points within the pulse. The devices studied were empirically separated into two groups as determined by the ratio

$$K = \frac{\text{Gate voltage at cutoff } (= V_{co})}{\text{Drain voltage at the onset of current saturation } (= V_{ds})} \quad (1)$$

Devices with K greater than unity sustained current

†Present address: Textronix, Inc., Beaverton, Oregon.

oscillations, those with K approximately equal to or less than unity were electrically quiet. For those cases with K greater than unity oscillations began beyond the knee of current saturation. In each case the oscillations ceased at high values of drain and gate bias. In most of the electrically unstable devices the onset of the oscillation is marked by a drop in current. In all cases the instability appears to be initiated when the average field under the gate contact first reaches the NDM threshold field value. This result holds true under different ambient temperature conditions. An estimate of the carrier velocity in the channel between the gate and drain contacts indicates that prior to the oscillation the electrons are usually drifting at speeds in excess of the saturation drift velocity. When the oscillations ceased with increasing gate bias the carrier velocity dropped to values significantly below the saturation drift velocity. Each of the above results are consistent with an instability arising from the presence of negative differential mobility.

2. DEVICE CLASSIFICATION

The classification parameter K (see eqn 1) emphasizes differences between the GaAs and classical FET, where for the latter [15] V_{gs} and V_{ds} are equal. For GaAs, the very earliest experiments [1, 2, 7] showed K varying from unity to values significantly higher than unity. (Current devices [17] have not altered this situation). In those experiments [1, 2] when $K = 1$, no instability was reported. When K was at the high end of the scale, the studies in Refs [2] and [7] showed that the device no longer exhibited the classical characteristics, but instead sustained spontaneous oscillations for a range of bias values.

The results of the computer simulation corroborate the empirical classification. But, in addition relate stability to the material parameter τ , the electron saturated drift velocity. Specifically, the simulations show that a necessary condition for a current instability is that the current at saturation either exceed or be within a narrow band about the value

$$I_s = G_0 E_p L \quad (2)$$

In eqn (2), G_0 is the open channel conductance ($= \text{Area} / (L \times \text{Resistivity})$), $E_p = v_s / \mu$, L is the source to drain separation, and μ the low field mobility of the semiconductor. In two terminal device language, E_p is the sustaining field [16]. Summarizing: If IDSS denotes the zero gate bias current at saturation then

$$\begin{aligned} \text{IDSS} < I_s &: \text{Stable current-voltage characteristics} \\ \text{IDSS} > I_s &: \text{Unstable current-voltage characteristics.} \end{aligned} \quad (3)$$

The above conclusion is essentially similar to that of Yamaguchi *et al.* [8].

The results discussed above summarize the general features of the GaAs FET. The space charge distribution within the FET is responsible for these properties and will be discussed in the next section.

3. LARGE SIGNAL DYNAMIC MODELLING OF THE GAs FIELD EFFECT TRANSISTOR

3(a). Introduction

The following analysis is for devices in the configuration of Fig. 1(a) where the source and drain contacts are at parallel ends of the device. This configuration eliminates geometrical effects due to coplanar placement of the source and drain contacts. Coplanar contact calculations have been performed for the configuration shown in Fig. 1(b), which also include the presence of a substrate. And the results of these studies show injection into the substrate, with the instabilities still remaining. All of the calculations reported below are for elements with doping levels nominally equal to 10^{17} cm^{-3} , a value approx. 1.5 to 2 orders of magnitude below that of presently fabricated devices. This choice was made because the cost of computing the contributions of transiting domains increases monotonically with increased doping level [18]. However, a number of representative calculations have been performed at higher doping levels with similar results. We note that the results of Yamaguchi *et al.* [8] were at $3 \times 10^{16} \text{ cm}^{-3}$ and where there is overlap with our studies there is agreement. Also, the main results of the experiment confirm the conclusion developed at these lower doping levels.

3(b). Current-voltage characteristics and space charge distribution for FET with $K = 1$

The space charge distributions for a $K = 1$ device are displaced in Figs. 2-4. The inset of each figure shows its current-voltage characteristic with the lower case letters keyed to the space charge distribution. The current is normalized to the value

$$I_s = G_0 E_p L \quad (4)$$

where E_p is the electric field at peak velocity. And the voltage is normalized to

$$V_p = E_p L \quad (5)$$

The bold curve is the electron drift velocity electric field relation scaled to current and voltage. The closed circles denote computed points and each point is a stable time independent point.

For the space charge distribution the x -axis represents the longitudinal spatial dependence. The vertical charge distribution is along the y -axis. The source contact is in the $y-z$ plane at $x = 0$; the drain contact is at $x = L$. The gate contact is in the $x-z$ plane at the indicated points.

At low values of drain bias and zero gate bias (Fig. 2a), there is a region of charge depletion under the gate contact. The charge region spreads somewhat beyond the gate contact boundaries (enclosed rectangular parallelepiped), but pretty much the space charge distribution is what one would expect from classical arguments [15]. An increase in drain voltage to the knee of the current-voltage relation (Fig. 2b) leads to a domain, representing the first significant departure from the classical analysis. The domain consists of an accumulation layer, which

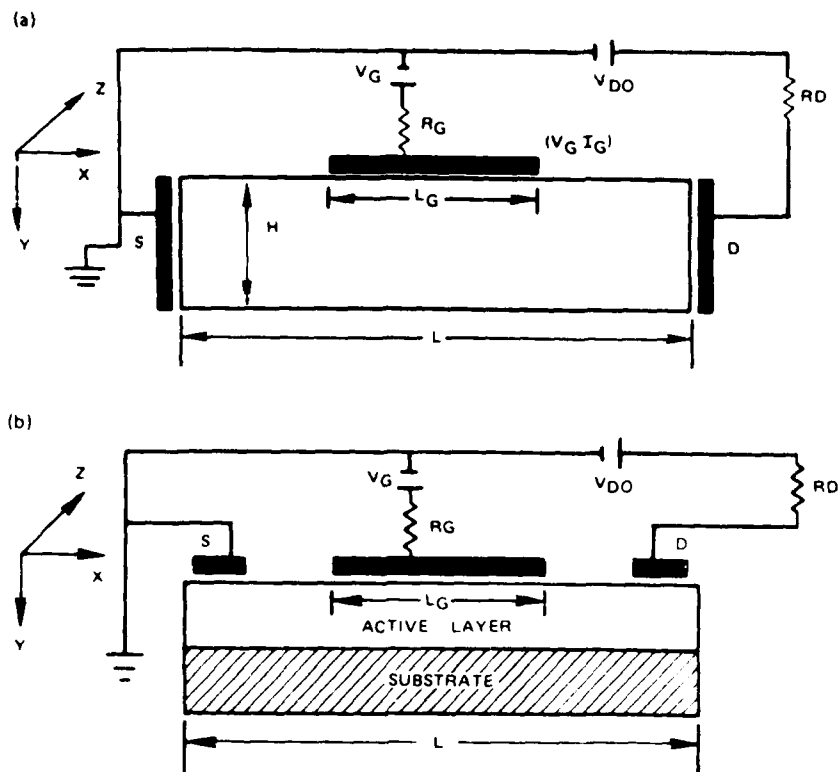


Fig. 1. Device-circuit configuration used in the FET simulations. (a) Parallel source and drain contacts. (b) Coplanar source and drain contacts. Substrate is included.

forms within the boundaries of the gate region and is followed downstream by a depletion layer. Domain formation is a consequence of current continuity and velocity limitation and occurs when the current density under the gate exceeds

$$J_p = N_{oe} v_p \quad (6)$$

where v_p is the maximum carrier velocity. Further increases in drain bias result in an increase in the amount of charge accumulated and a broadening of the domain (Fig. 2c). We point out that while the presence of a domain is necessary for a current instability, it is not sufficient. By analogy with two terminal devices the current density downstream from the dipole must exceed the sustaining current, J_s , where

$$J_s = N_{oe} v_s \quad (7)$$

(see also eqn 2). This criteria is approximately satisfied for the FET but is not as stringent. It suffices to state that the current density for the $K \approx 1$ devices is generally too low to sustain an instability.

The calculations of Fig. 3 are for finite values of gate bias. At low drain bias levels the depletion layer extends well beyond the gate boundaries. We see a region of local charge accumulation, although clearly there is a net depletion of carriers. However, increasing the drain bias results in a strong region of charge accumulation, fol-

lowed by significant depletion until the drain contact is reached where the boundary conditions require a significant increase in the charge density.

Two extreme conditions are displayed in Fig. 4. Here at low values of drain bias and a value of gate bias near cutoff we see the presence of a depletion layer broadly surrounding the gate region. At zero gate bias levels but very high drain bias levels we see the presence of a region of charge accumulation extending from the gate region to the drain contact.

We summarize the above results by stating that for a collection of ostensibly classical current-voltage curves the space charge distribution is far different in many circumstances from that developed originally for the FET [15]. Thus while the current-voltage relation does not provide us with detailed information about the distribution of space charge for the $K \approx 1$ device, we expect that the form of the distribution will affect the equivalent circuit element representations of the device [4,5].

3(c). Current voltage characteristics and space charge distributions for FETs with $K > 1$

For a given doping level and source drain spacing, the principle difference between devices with $K > 1$ and $K \approx 1$ is that the former have wider channels, therefore, lower open channel resistances, and for a given bias draw more current. For these devices the current density is usually high enough to sustain an instability. In our simulations the onset of the instability marked the onset

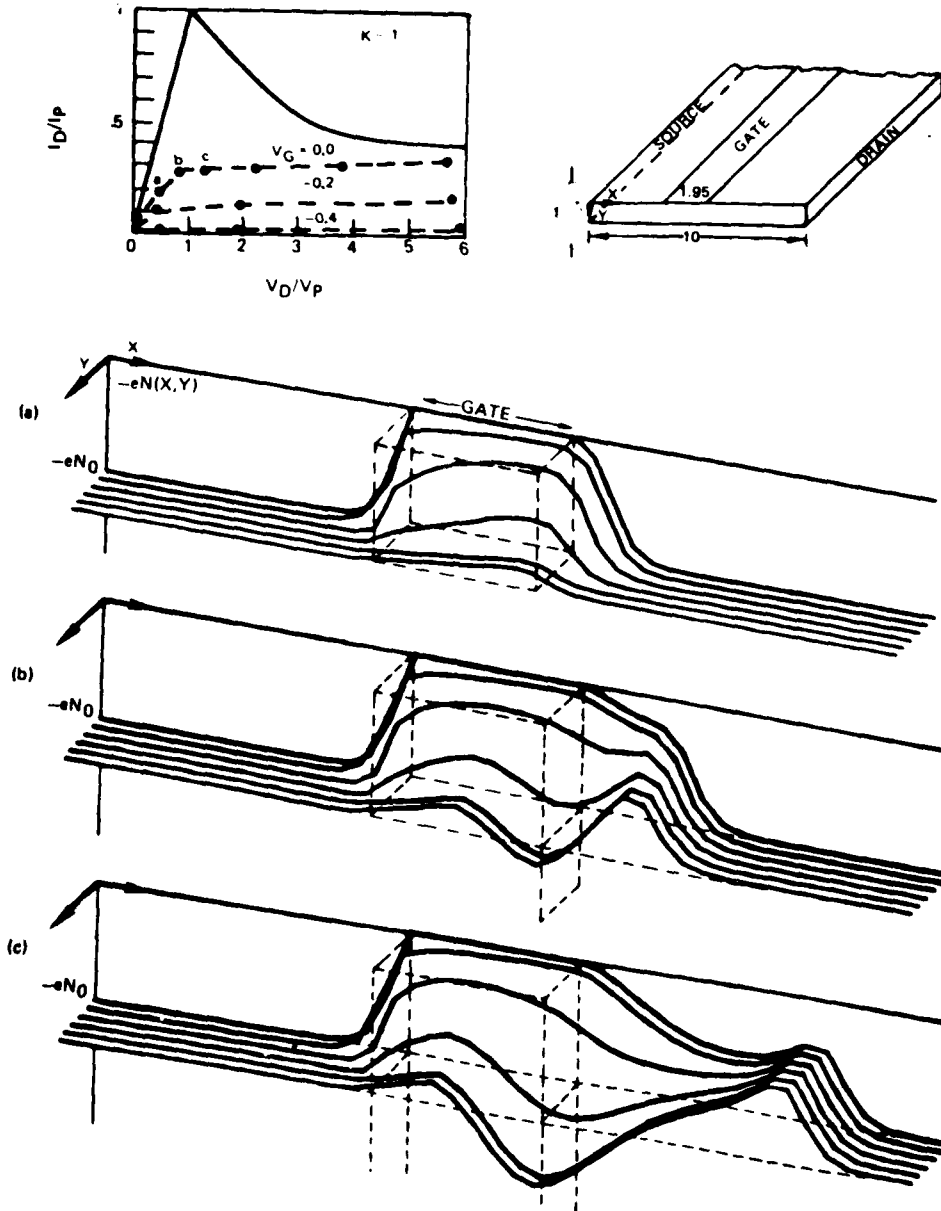


Fig. 2. Space charge configuration as a function of bias. Profiles correspond to indicated points on the current voltage characteristics. Solid line represents GaAs velocity vs electric field relation scaled to current and voltage. Device configuration is also shown, with dimensions in microns.

of current saturation. In our experiments, the instability occurs *after* the device enters saturation. The simulations for the wider channel device are displayed in Figs. 5 and 6.

Figure 5(a) shows the charge distribution at a bias level just below that necessary to launch a traveling domain. Within the gate boundaries there is charge depletion. But towards the bottom of the channel and just before the boundary there is a trace of an accumulation layer—implying that the current density is highest there. Coupling this result to the current value in the inset to Fig. 5, we have the result that within the gate boundary the

current density is approximately equal to J_p , while within the gate-to-drain region the current density exceeds J_p .

The above conditions are sufficient to launch a domain in two-terminal devices, and indeed here a slight increase in drain bias results in the launching of a domain (Fig. 5b). In this case further increases in bias result in the charge accumulation layer spreading toward the bottom of the channel (within the gate boundaries) and also toward the drain contact. The domain detaches from the gate region and periodic transit time oscillations occur. Figure 5(b) shows a "snapshot" of the domain at one instant of time during propagation. (Recycling domains

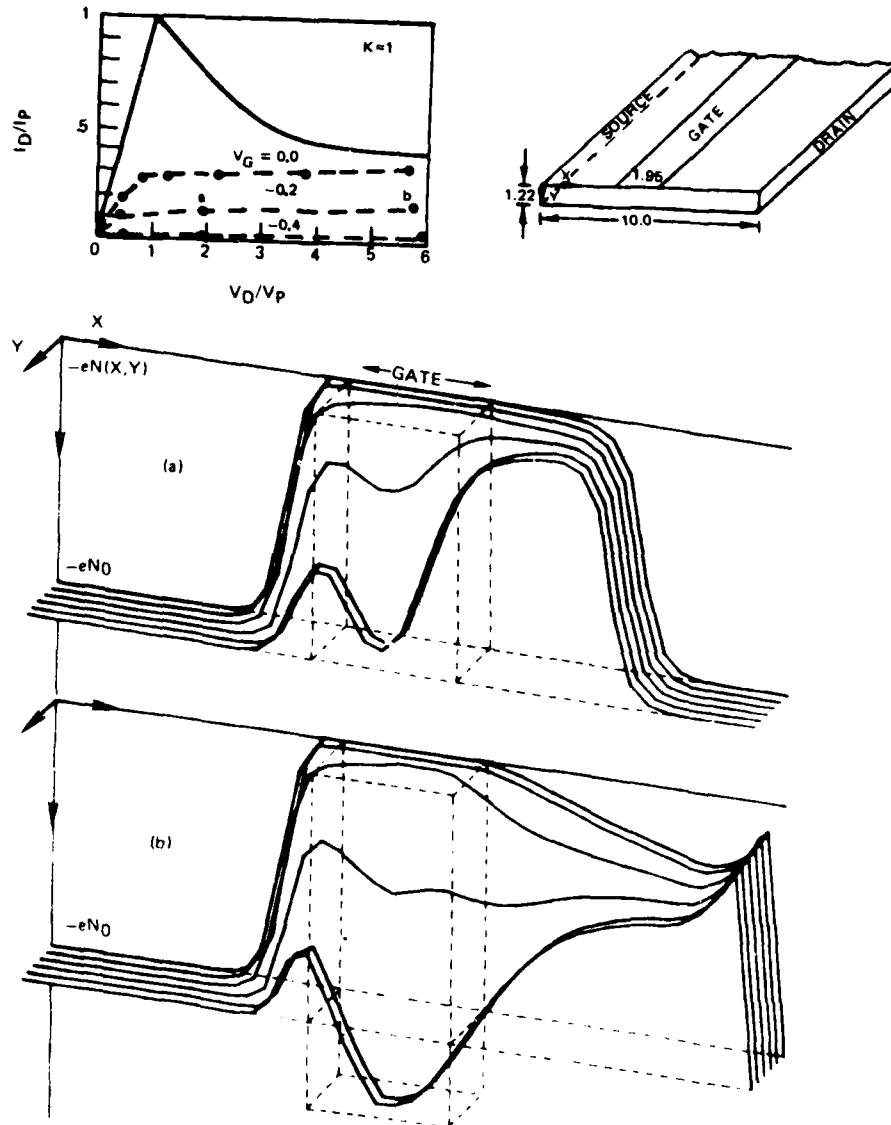


Fig. 3. As in Fig. 2, but for different bias values.

are illustrated in Fig. 5. Ref. [3].) The propagating and recycling domain can persist for a rather wide range of drain bias values. The amplitude of these resulting transit time oscillations are bias dependent as illustrated in Fig. 7.

Figure 7 contains plots of drain and source current vs drain potential at different times, with time eliminated between these. In Fig. 7(a) we plot drain current vs drain voltage for four different values of drain bias. The bold lines denote calculated results; the dashed lines are an estimate of the current vs voltage; the skew lines are the drain d.c. load lines. In each calculation displacement current contributions result in transient drain current values in excess of their steady state values. This is apparent for the bias levels of 1.4 and 1.6 V_p , where after steady state has been reached the displacement current

goes to zero and the system relaxes to the value denoted by the closed circle. When the domain is propagating the current oscillates along the load line. At a bias of 1.6 V_p the current oscillation amplitude is somewhere around 20% of its d.c. value. Further increases in drain bias result in an increase in the amplitude of the oscillation. The average current associated with these oscillations is denoted by the x 's. We note that the average-current-voltage relation for the range in which there are transit time oscillations, exhibits a region of negative differential conductivity (NDC). The NDC is, for these calculations dynamic in origin. The second part of Fig. 7 shows the source current vs drain voltage for the same calculation as that of 7(a). Here, in Fig. 7(b) we see the presence of superlinear current-voltage relations at low drain bias levels, followed by looping when domains are present.

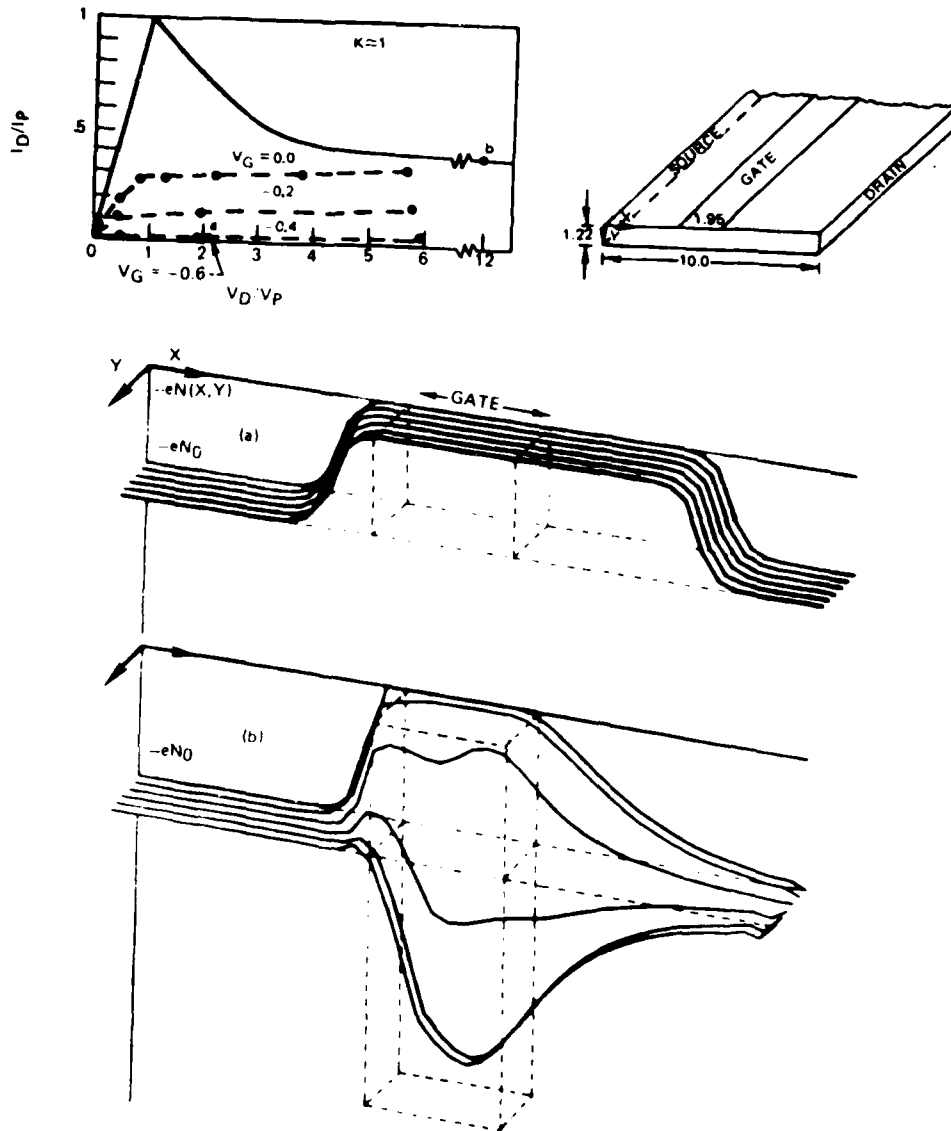


Fig. 4. As in Fig. 2, but for different bias values.

Both of these effects occur because of large transients through the gate contact.

With respect to transit time oscillations we point out that no experiment has yet been designed that provides unequivocal evidence for their existence in commonly fabricated GaAs FET's. In most common designs the gate to drain separation is somewhere between one-half and five microns, and for these values it is not clear that conditions exist for the propagation of "stable" domains [16]. The result is that the properties of these propagating domains are readily influenced by the external circuit and can in some cases be controlled by it. An example of this complex dipole-circuit interaction exists in two terminal devices (e.g. the quenched multiple dipole mode [16]). There is also the possibility that in place of the negative differential mobility induced oscil-

lations in GaAs FETs there are feedback circuit oscillations that are independent of any hot electron effects. However, in the experiments reported below we show that the evidence points to the oscillations as being negative differential mobility induced. Two additional space charge profiles are important in this regard and are discussed below.

The two profiles of interest are coincident with the suppression of transit time oscillations. In one case a significant increase in drain bias alone suppresses the instability. In the second case an increase in the magnitude of the gate bias is sufficient to suppress it. The space charge profile associated with the high drain bias suppression of the instability is displayed in Fig. 6(a). We see that an accumulation of charge forms downstream from the gate boundaries and extends towards the drain

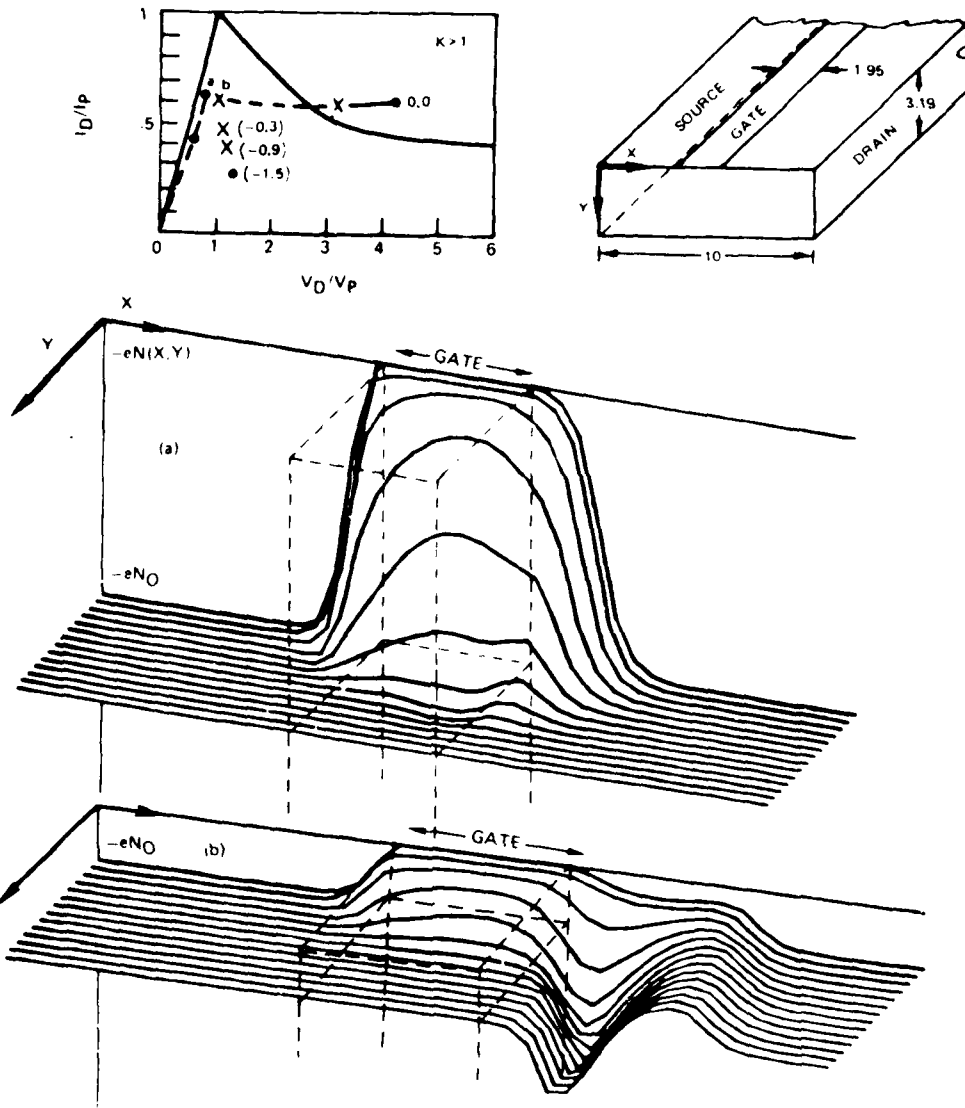


Fig. 5 As in Fig. 2, but for a different size device. X's denote transit time oscillations

contact. While this layer generally is not a static one but instead pulsates in time there are some broad features associated with it. For example, the profile forms at values of current density in excess of J , and at high values of drain potential. Most of the potential drop is across the gate-to-drain region (Ref [3], Fig. 7), where we may expect the electric fields to be well within the saturated drift velocity region. Thus the carriers within the gate-to-drain region are traveling at their saturated drift velocity values. This fact and current continuity with the current density exceeding J , are responsible for the region of charge accumulation. By way of analogy this solution is qualitatively similar to two terminal device solutions which show the presence of anode adjacent domains [16]. Further, in three terminal devices with long gate-to-drain spacings and high doping con-

centrations the anode adjacent domain has been experimentally probed [19].

The space charge profile associated with the high gate bias suppression of the instability is displayed in Fig. 6(b). This shows a snapshot of the space charge layer while undergoing a damped oscillation. This layer of charge also pulsates in time, but in contrast to the space charge layer of Fig. 6(a), this one forms at current density values that are less than J . Indeed for this case most of the potential drop falls under the gate contact and extends some distance downstream from the edge of the gate boundaries [3] (Fig. 8). As long as the space charge layer does not reach the drain contact the electric field downstream from the edge of the nonuniform space charge region will be less than the "two-terminal sustaining field" [16] (Fig. 1, μ). This situation is analogous

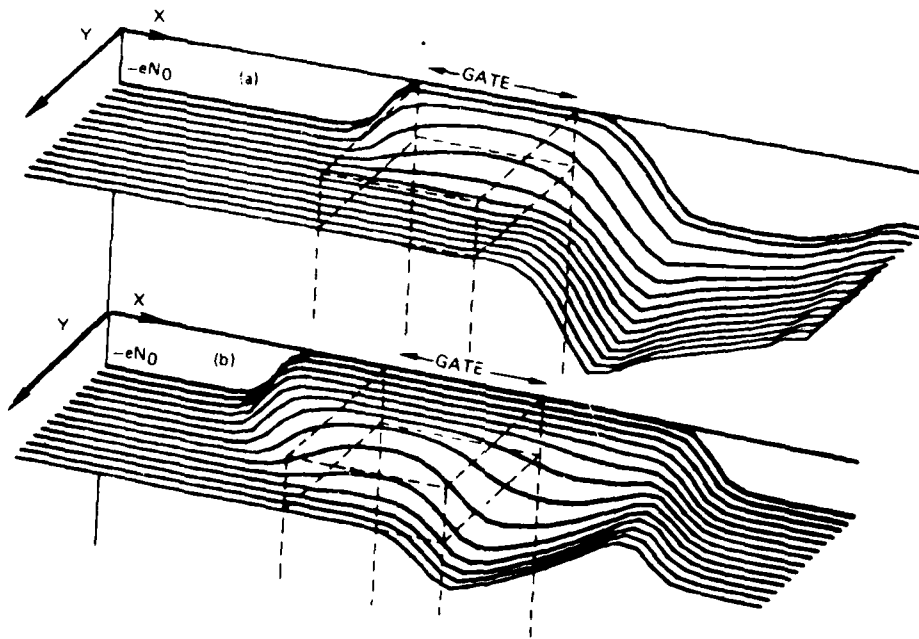
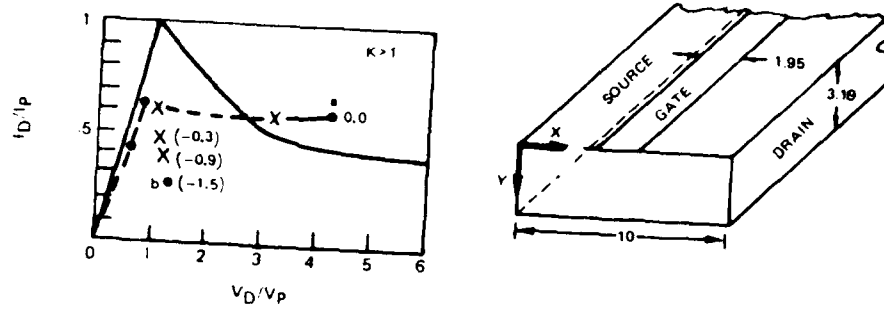


Fig. 6. As in Fig. 5, but for different bias values.

to the two terminal high cathode boundary field profiles[16].

3(d). Summary

To summarize, there are several key features associated with negative differential mobility induced instabilities in field effect transistors. These are:

(1) The instability occurs in devices with K greater than unity.

(2) The instability occurs at or beyond the "knee" of the current-voltage relation.

(3) A necessary condition for an instability is that the current density downstream from the gate boundary be greater than or approximately equal to J_c , or equivalently, that the drift velocity either exceeds v_c or is approximately equal to v_c .

(4) Saturation in current occurs when the average field within the conducting channel under the gate contact is

approximately equal to the threshold field for negative differential mobility.

(5) The instability can be suppressed by imposing a gate bias sufficiently high to reduce the current density downstream from the gate boundary to a value significantly less than J_c .

(6) The instability can be suppressed by imposing a sufficiently high value of drain bias.

Let us now turn our attention to how these instabilities manifest themselves in actual devices.

5. EXPERIMENTS WITH GALLIUM ARSENIDE FIELD EFFECT TRANSISTORS

5(a). Experiments with $K > 1$

Figures 8 and 9 display, respectively, temperature dependent, d.c. and pulsed drain current vs drain voltage characteristics for a GaAs FET. The source, drain and

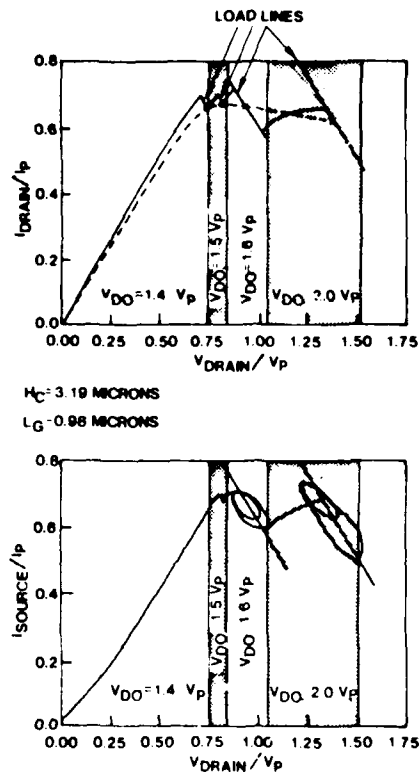


Fig. 7. Instantaneous current vs voltage for the device of Figs 5 and 6. (a) Drain current vs drain voltage. (b) Source current vs drain voltage.

gate contacts are coplanar with the source and drain contacts separated by approx. $8.5 \mu\text{m}$. The gate is more or less centrally placed with a length, L_g , equal to $3.0 \mu\text{m}$. The gate width, L_g , is $250 \mu\text{m}$. The epitaxial layer thickness, H , was $3000 \pm 500 \text{ \AA}$ with a nominal doping level of $10^{17}/\text{cm}^3$. The mobility measured from adjacent samples varied from 3000 to $4000 \text{ cm}^2/\text{V}\cdot\text{s}$. The cutoff voltage for this device was 8.9 V . This device sustained current oscillations as detected by a spectrum analyzer. All six criteria listed in the last section for NDM induced instabilities were satisfied. We discuss each separately below. Oscillation characteristics

(1) $K = V_{DO}/V_{DC} \approx (8.9 + 0.8 \text{ V})/2.5 = 3.9$, where the cutoff voltage includes as assumed built in potential of approx. 0.8 V .

(2) At each value of ambient temperature, the instability occurred beyond the knee of the current voltage characteristic.

(3) The velocity was computed from the relation

$$v = I/(N_0 e H L_g) \quad (8)$$

And the values prior to an instability are displayed as a function of ambient temperature in Fig. 10(a) where the error bars represent uncertainties in the value of H . In Fig. 10(a) the solid line corresponds to an estimate of the saturated drift velocity from Ruch and Fawcett[20] and Freeman and Hobson[21]. This data is available only to

12 kV/cm , and we have reduced these results by approx. 10% for higher fields. The closed circles in Fig. 10(a) are for the d.c. measurements; the Δ 's represent pulsed measurements ($1 \mu\text{sec}$ pulse lengths, 1% duty cycle). The pulsed results generally surround the solid line and are higher than the d.c. results. In general over the temperature range exceeding 150 K the pulsed measurements yield a velocity exceeding v_s .

(4) The average field under the gate boundary is estimated from the relation

$$E_g = V_{Tg}/L_g \quad (9)$$

where V_{Tg} is the longitudinal potential drop under the gate contact and is obtained from an equation that ignores contact resistance contributions

$$V_{Tg} = V_{Dg} - IR_{0g}I/L_g \quad (10)$$

where V_{Dg} is the drain voltage and I the drain current. $R_{0g} (= 1/G_{0g})$ is the open channel resistance and may be obtained from the measured drain current-voltage characteristics of the device via the relation

$$R_{0g} = R_d(V_{Dg}) \left(1 - \frac{(V_{Dg} - V_{DO})^2}{V_{DO}^2} \right) / \left(1 - \left[1 - \frac{I_{Dg}}{I} \right] (V_{Dg} + V_{DO}) \right) \quad (11)$$

where we have adopted the viewpoint of eqns (2) and (3) of Grebene[22]. V_{DO} in eqn (11) includes the built-in potential. The above expression for R_{0g} is expected to be valid at low values of drain bias. Assuming a built-in potential of 0.8 V and reading R_{0g} at $V_{Dg} = 0$ from the d.c. characteristics we compute R_{0g} . The values are listed in Table 1, where we have ignored the temperature variations in V_{Dg} and V_{DO} . We see that the average field under the gate is relatively insensitive to temperature, as is the threshold field for negative differential mobility[20]. An average field of 4.2 kV/cm is consistent with a mobility for $10^{17}/\text{cm}^3$ material of $4200 \text{ cm}^2/\text{V}\cdot\text{s}$.

(5) As shown in Fig. 10(b) the carrier drift velocity at the cessation of oscillations is below v_s .

(6) All oscillations cease at high drain bias levels.

The next set of data are displayed in Fig. 11 where we show d.c. and sampling scope data (taken 25 nsec into a 50 nsec pulse, with low duty cycle). The GaAs FET had a source to drain spacing of $3.5 \mu\text{m}$ and a gate length of $1 \mu\text{m}$. The cutoff voltage for this device was 3.0 V and the mobility was quoted at around $4500 \text{ cm}^2/\text{V}\cdot\text{s}$. With regard to the first two oscillatory criteria, $K \approx 4.8$ and the instability occurs just beyond the knee of the current vs voltage characteristic. The peak velocity just prior to the instability at 57 ma is computed from the equation

$$v = \mu IR_{0g}I \quad (12)$$

with $R_{0g} = 9.7 \Omega$ (from pulsed data) and $\mu = 4500 \text{ cm}^2/\text{V}\cdot\text{s}$. The result is $v = 0.68 \times 10^7 \text{ cm/sec}$, which falls approximately within the range of values of Fig. 10. An average threshold field of 4 kV/cm for a one micron gate

Table I. d.c. Data

T CASE	V_{DS} (v)	$I_0 \times 10^{-3}$ (a)	R_d (OHMS)	R_o (OHMS)	E_{av} (Kv/cm)
383°K	2.5	82	26.3	23.0	4.26
299°K	2.5	90	24.2	21.7	4.22
166°K	2.5	21.1	18.4	4.17	
77°K	2.5	115	20.0	17.5	4.00

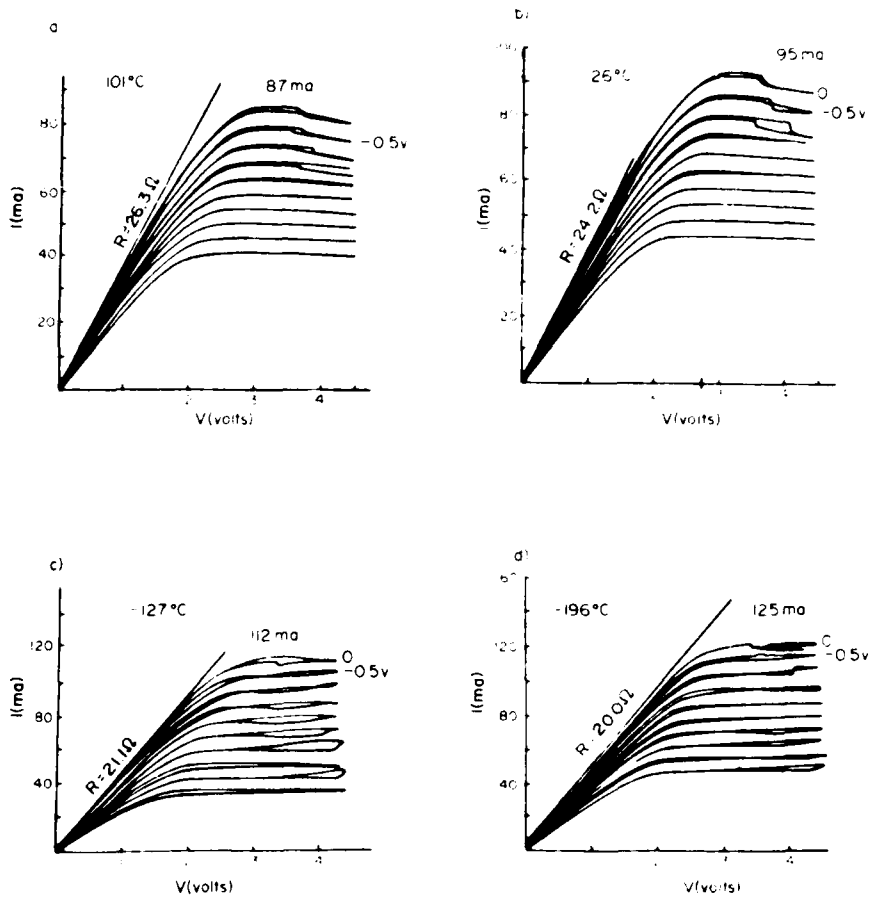


Fig. 8. Temperature dependent d.c. current-voltage data for a long gate FET. Device parameters are discussed in text.

is reached at a drain voltage of approx. 0.8 V; and it is here that we see substantial preinstability current broadening. The oscillations which are initiated at about 1.2 V are not suppressed until a sufficiently low value of current density is attained. The characteristic of the instability is suggestive of hot electron contributions richer than that discussed in the last section (see also Ref. [13]). However, consistent with the sixth criteria the oscillations are suppressed at high values of drain bias. This is displayed in Fig. 12 where we show sampling scope measurements at increasing drain bias for the device subjected a 1.5 μ sec pulse. We see the initiation

of oscillations at low drain bias levels with subsequent suppression at high drain bias levels.

4(c). Experiment with $K = 1$

The final set of measurements is for a device with K approximately equal to unity. These are pulsed measurements. The device has a cutoff voltage of approx. 1.8 V and no oscillations were detected on a spectrum analyzer over a range of 40 GHz. The device had a quoted doping concentration of $5 \times 10^{16} \text{ cm}^{-3}$ and an epitaxial thickness of 0.5 μm . These values were not

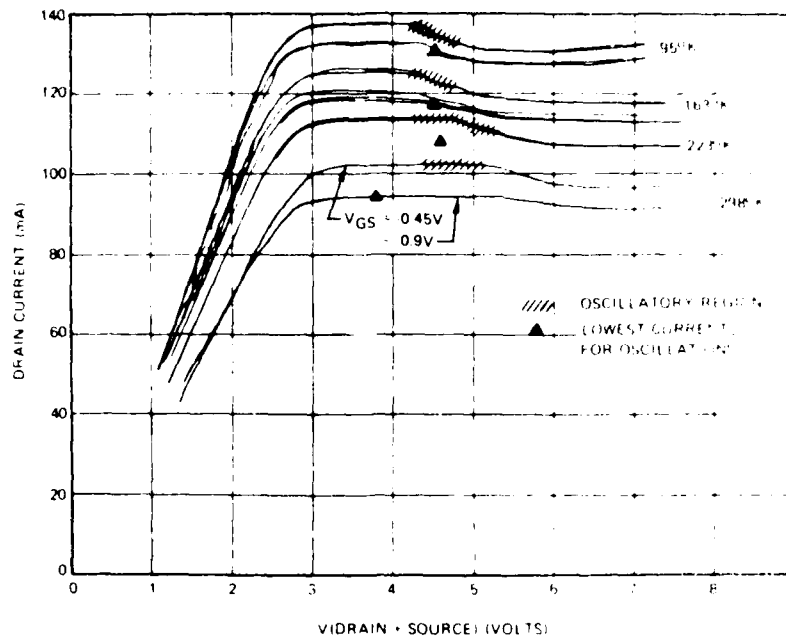


Fig. 9. Temperature dependent pulsed data for the device of Fig. 8. For these measurements a 500 μ H inductor was connected in series with the source from ground.

consistent with pinchoff values using the equation

$$V_{GS} = eN_0H^2/2\epsilon. \quad (13)$$

With a quoted value of $L = 360 \mu\text{m}$, eqn (8) yields a room temperature range of values of τ , associated with the product N_0H

$$\tau = 4.7 \cdot 10^{18} N_0H. \quad (14)$$

From eqn (14) with N_0H varying from $10^{12}/\text{cm}^2$ to $1.5 \cdot 10^{12}/\text{cm}^2$, τ varies from about $0.5 \cdot 10^{-7} \text{cm}^2/\text{sec}$ to $0.3 \cdot 10^{-7} \text{cm}^2/\text{sec}$. All values are too low for an instability to occur.

4(c) Discussion

The experiments discussed above provide evidence that the GaAs FET is capable of sustaining negative differential mobility induced current instabilities. These instabilities occur when the average field under the gate contact exceeds the NDM threshold field and when the current density at the onset of saturation is approximately equal to or exceeds the saturation drift current density for GaAs. There are several additional experimental aspects that should be highlighted. The d.c. measurements of Fig. 8 were characterized by a drop in current at the instability threshold; the pulsed measurements also show a drop in current. The d.c. measurements of Fig. 11 do not show a dropback in current; the sampling scope measurements do. There is hysteresis in the d.c. measurements of Fig. 8 with the instability persisting for increasing and decreasing values of drain bias. However on the decrease the instability persisted at drain bias levels somewhat below the instability threshold. This is a

characteristic of two terminal transistor devices. With regard to the sampling scope measurement of Fig. 11, we see some spreading of the current vs. voltage prior to the instability. This may correspond to a pulsating trapped domain near the gate contact as discussed in the earlier sections.

The oscillation properties reported here on a device using sampling oscilloscopes and spectrum analyzers. Spectral analysis was used on the devices of Figs. 8, 9 and 13. Sampling scope measurements were for the device shown in Figs. 11 and 12 and other devices not reported here. At first the spectrum analyzer was set up to detect frequencies to 18 GHz. In this set up, frequencies of 12, 16, 25 and 42 GHz were detected. These oscillations were bias dependent but ceased at drain bias levels in excess of 6 V. The oscillations ceased at substantially higher gate bias levels. Under the assumption that there were additional frequencies in excess of 18 GHz that were going undetected, and that by analogy to two terminal devices where the introduction of an inductor reduces the circuit frequency, we introduced a $\frac{1}{2}$ nH inductor in series with the source loop. The low frequency oscillations disappeared and in their place were instabilities at 13, 13.6 and 14.2 GHz. More detailed spectral analysis measurements were subsequently made with the spectrum analyzer open to frequencies to 40 GHz. The pulsed measurements were then analyzed, with the following details. Oscillations began at 3.5 V and persisted to just below 4.25 V. Oscillations were observed at 6.5, 13, 23, 30, 36 and 40 GHz. Higher frequencies could not be detected. The oscillations were strongest at 4.1 V where the 6.5 and 40 GHz signals dominated. At 4.25 V on the drain the oscillations ceased, at least up to 40 GHz. In the same measuring circuit and with the gate

AD-A108 140

UNITED TECHNOLOGIES RESEARCH CENTER EAST HARTFORD CT F/G 20/14
INFLUENCE OF CONTACT CONDITIONS AND THE CIRCUIT ON SHORT NEGATIVE-ETC(U)
AUG 81 H L GRUBIN N00014-78-C-0269

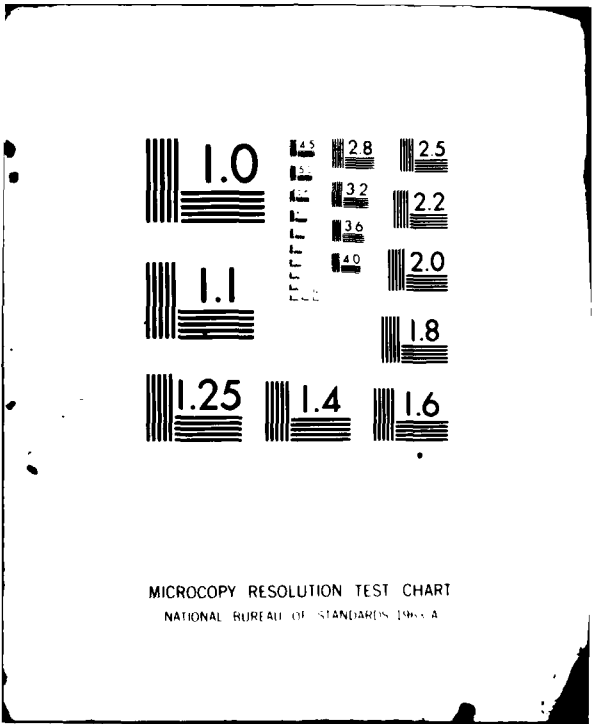
UNCLASSIFIED

ML

2-2
078 40



END
DATE
FILMED
8-82
NTIC



MICROCOPY RESOLUTION TEST CHART
NATIONAL BUREAU OF STANDARDS-1963-A

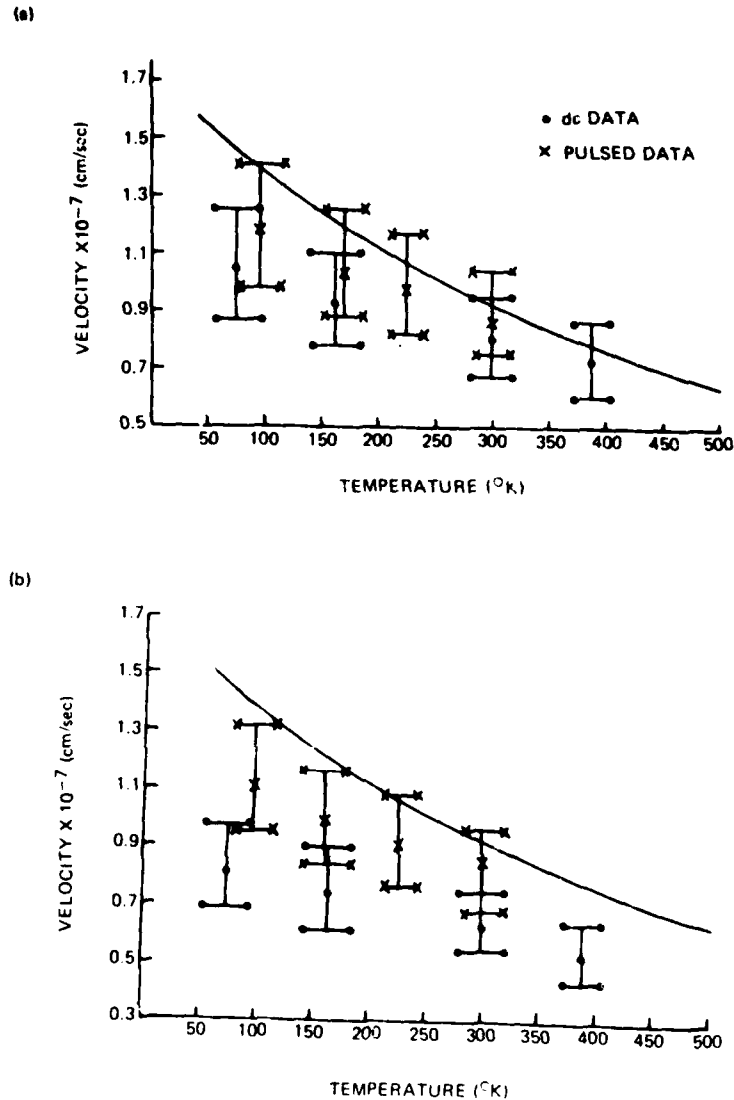


Fig. 10. Solid curve is an estimate of high field saturated velocity vs ambient temperature. (a) Velocity, from eqn 8, vs ambient temperature, prior to oscillations. (b) Velocity, from eqn 8, vs ambient temperature, at cessation of oscillations with application of a high gate bias.

wide open visible light was detected at 6.4 V on the drain. This was not accompanied by any oscillations whose frequency was below 40 GHz. An initial reduction in potential on the gate contact resulted in similar behavior but at -0.8 V on the gate, all oscillatory activity ceased, including the appearance of light. The electrical behavior of this device was measured at a variety of temperatures, with qualitatively similar behavior.

The oscillation frequencies reported above bear no clear relation to the transit-time oscillation frequency. As indicated in Section 3, the gate drain separation may be too short to guarantee stable domain propagation and so the oscillatory properties, including the frequency are likely to be determined by a complex device-circuit interaction. There is also the possibility that the oscillations we are observing are a consequence of feedback

between the gate and drain loop. While this situation cannot be ignored the evidence in terms of the six instability criteria given in the last section, including the suppression of oscillations at high drain bias levels, make this possibility small.

In the above paragraphs we reported the observation of light. Light was also observed under d.c. conditions. The details are as follows. Under d.c. conditions light was seen at the beginning of the current instability, became dimmer as the drain bias increased but remained while the device oscillated. The light was stronger at drain bias levels sufficient to eliminate the oscillations. At moderate gate bias levels faint light remained; but at sufficiently high gate bias levels large enough to eliminate the oscillations, all light activity ceased. The light, for all practical purposes was white. The observations of light is

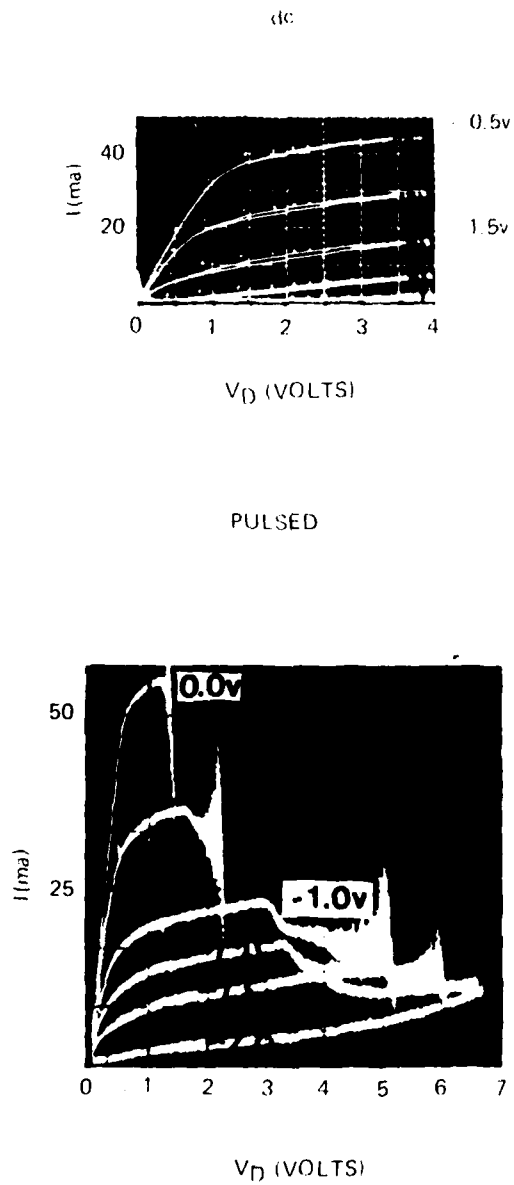


Fig. 11. (a) d.c. and; (b) pulsed sampling scope measurements of the current voltage characteristics for a short gate FET.

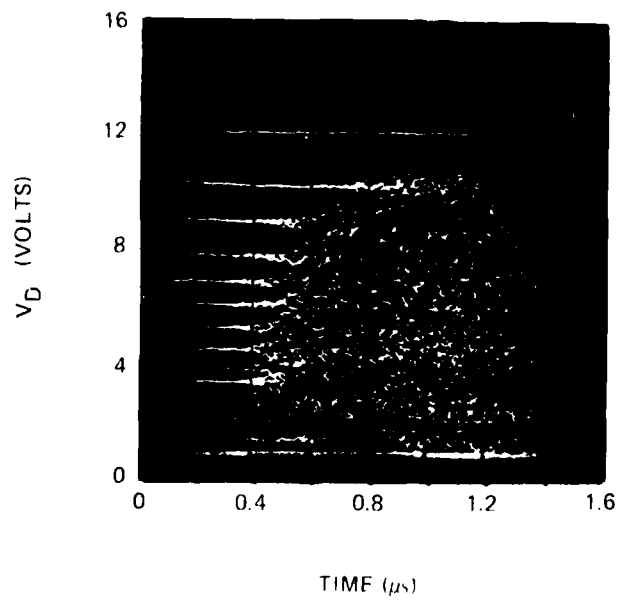


Fig. 12. Sampling scope pulsed drain voltage vs time as a function of drain bias for the short gate FET.

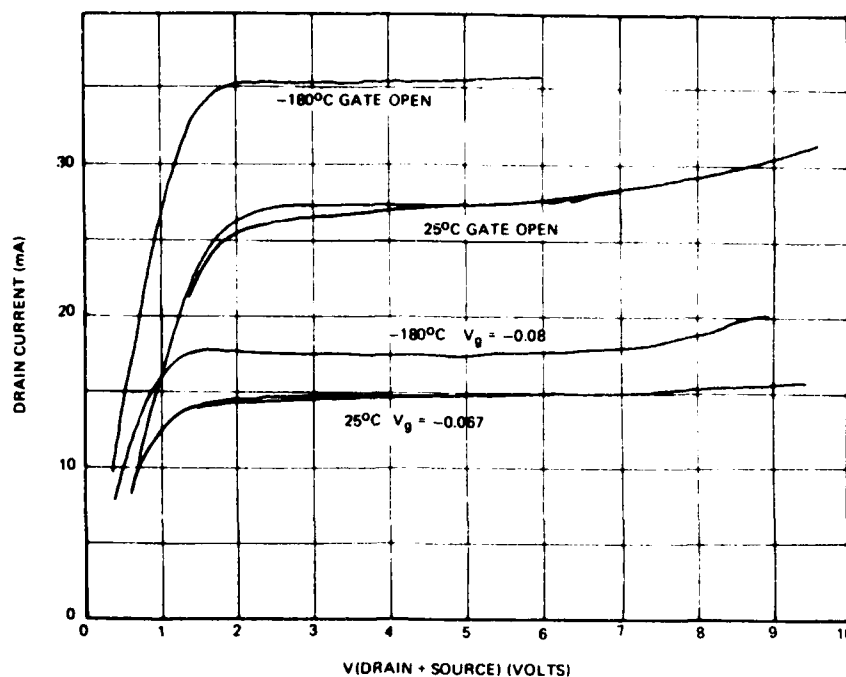


Fig. 13. Pulsed current vs voltage data for a device that did not exhibit any oscillations

compelling evidence for the presence of regions of high electric field and excess carriers. At low drain bias levels, the dimness of the light may be accounted for by the fact that the time averaged electric field at a given point within the sample is less for propagating domains than for the trapped domains. The latter occurs at high drain bias levels. The absence of light at high gate bias levels may possibly be due to the broad region of charge depletion in the vicinity of the gate boundary. The arguments for white light are somewhat uncertain. We recall, however, that the separation between the central portion of the conduction band and the valence band is within the infrared, while the separation between the satellite conduction and valence bands is within the ultraviolet. The entire visible spectra is within these two bounds.

We note that Mimura *et al* [23] on $10^{17}/\text{cm}^3$ GaAs FETs also observed visible white light at high drain bias levels. For devices with highly doped n^+ drain contacts light was observed at the n^+n interface; for devices without an n^+ drain contact radiation was observed at the drain metalization edge. Mimura *et al.* [23], attribute the radiation to impact ionization within a domain trapped at the drain contact. The intensity of this light was observed to increase with drain bias and decrease as the gate voltage was made negative. These results are consistent with our findings.

5. SOME MODELLING CONSIDERATIONS

The results of our analysis are consistent with the identity

$$IDSS \times R_0 = E_{out}L \quad (15)$$

where E_{out} is the longitudinal electric field in the source to gate region. In devices with K greater than unity, E_{out} will generally be at least equal to E_s ; and so for this case a lower bound for $IDSS$ exists:

$$IDSS \times R_0 \geq E_s L \quad (16)$$

For example, with the device reported in Figs. 8 and 9, the room temperature values of the l.h.s. of eqn (16) (from Table 1) is equal to 1.9 V. The r.h.s. side with $E_s = 2.2 \text{ kV/cm}$ is equal to 1.87 V. For the device whose properties are displayed in Figs. 11 and 12, $IDSS \times R_0 = 0.52 \text{ V}$, while $E_s L = 0.77 \text{ V}$. By way of comparison Shockley's study [24] teaches that

$$IDSS \times R_0 = V_{co}/3 \quad (17)$$

while more recently Shur [25] have concluded that

$$IDSS \times R_0 = E_s L_g \quad (18)$$

Equation (18) yields results significantly lower than observations, and less than eqn (16).

6. CONCLUSIONS

In conclusion, through analysis and experiment we have presented evidence for the presence of negative differential mobility induced current instabilities in GaAs FETs. We have listed six criteria that identify these NDM instabilities, paramount among these is the fact that the longitudinal electric field under the gate must be greater than the threshold field for negative differential mobility while the current density must exceed the sus-

taining current. The fact that the instabilities in some cases are delayed until higher values of bias are reached implies that the field must exceed the NDM threshold field for the instability. We have also presented corroborating experimental and theoretical evidence, consistent with the conclusions of Yamaguchi *et al.* [8], that devices whose current densities, within the source to gate region, are less than J_c will not go unstable. Those whose current densities exceed J_c will sustain instabilities.

Acknowledgements—We are grateful for the help of K. Siegler and A. MacPherson of the Naval Research Laboratory in the preparation and characterization of several devices. P. Greiling and C. Krumm of the Hughes Research Laboratory are thanked for the supply of several devices used in our experiments. We also benefited from conversations with G. O. Ladd, Jr., F. R. Rosenbaum and D. Lile. This work was partially supported by the Office of Naval Research (H.L.G.) and the Army Research Office (D.K.F.).

REFERENCES

1. C. A. Mead, *Proc. IEEE*, **54**, 307 (1966).
2. H. R. Winteler and A. Steinemann, *Proc. Int. Symp. GaAs* (1966), *Inst. of Phys. Conf. Ser.* 3, London, p. 228 (1967).
3. H. L. Grubin and T. M. McHugh, *Solid-St. Electron.* **21**, 69 (1978).
4. R. W. H. Engelmann and C. A. Liechti, *IEDM Tech. Digest* 351 (1975).
5. R. W. H. Engelmann and C. A. Liechti, *IEEE Trans. Electron. Dev.* **ED-24**, 1288 (1977).
6. H. A. Willing and P. de Santis, *Electron. Lett.* **13**, 537 (1977), *lised*.
7. R. Zuleg, *Proc. Int. Symp. GaAs* (1968), *Inst. of Phys. Conf. Ser.* 7, London, p. 181 (1969).
8. K. Yamaguchi, S. Asai and H. Kodera, *IEEE Trans. Electron. Dev.* **ED-23**, 1283 (1976).
9. S. P. Yu and W. Tantraporn, *Proc. 6th Biennial Cornell Electron Engng Conf.* Cornell Univ. Ithaca, p. 399 (1978).
10. H. L. Grubin and T. M. McHugh, *Proc. 6th Biennial Cornell Electron Engng Conf.* Cornell Univ., Ithaca, p. 409 (1977).
11. K. R. Gleason and H. L. Grubin, Unpublished results presented at 1978 Workshop on Compound Semiconductor Materials for Microwave Active Devices, San Francisco, C.A., 13-14 February 1978.
12. H. L. Grubin, D. K. Ferry and K. R. Gleason, Unpublished results presented at the 1978 Workshop on Hot Electron Phenomena in Semiconductors, Cornell University, 17-18 August 1978.
13. P. H. Wang, C. T. Li, D. Poulin, K. Richter and P. Froess, *IEDM Tech. Digest* 377 (1978).
14. Healy R. M. and B. S. Hewitt, Unpublished results presented at the 1979 Workshop on Compound Semiconductor Materials for Microwave Active Devices, Atlanta GA, 19-20 February 1979 (with permission of the authors).
15. W. Shockley, *Proc. IRE* **40**, 1365 (1952).
16. M. P. Shaw, H. L. Grubin and P. R. Solomon, *The Gunn-Hilsum Effect*. Academic Press, New York (1979).
17. J. V. DiLorenzo, *Proc. 6th Biennial Cornell Electron Engng Conf.* Cornell University, Ithaca, p. 1. (1977).
18. T. McHugh, H. L. Grubin and P. Kirchner, to be published.
19. Private communication.
20. J. G. Ruch and W. Fawcett, *J. Appl. Phys.* **41**, 3843 (1970).
21. K. R. Freeman and G. S. Hobson, *IEEE Trans. Electron. Dev.* **ED-19**, 62 (1972).
22. A. B. Grebene, *Proc. IEEE* **55**, 2031 (1967).
23. T. Mimura, H. Suzuki and M. Fukuta, *Proc. IEEE* **65**, 1407 (1977).
24. See e. g. R. S. C. Cobbold, *Theory and Applications of Field Effect Transistors*, p. 80. Wiley-Interscience, New York (1970).
25. M. S. Shur, *IEEE Trans. Electron. Dev.* **ED-25**, 612 (1978).

TRANSIENT EFFECTS IN SUBMICRON DEVICES - LOAD LINE DEPENDENCE

H. L. Grubin
United Technologies Research Center, East Hartford, Connecticut

D. K. Ferry
Colorado State University, Fort Collins, Colorado

J. R. Barker
University of Warwick, Coventry, England

ABSTRACT

We compute the transient response of gallium arsenide submicron two terminal devices and examine their load line dependence.

I

For the small device (SD) whose active region length is typically between a mean free path and two microns, the average electron drift velocity, V , cannot be represented as an explicit function of electric field. Rather, since the important time processes such as transit-time, momentum and energy relaxation time, are comparable, the carrier velocity must be calculated as a function of space and time (see, e.g., Ruch, reference 1). In a typical situation where the SD is connected to a power supply through a load, the velocity response will depend on the properties of the load. We demonstrate this dependence for a purely resistive load.

The study is numerical and involves solving the blocks of equations in figure 1. Blocks I and II are apparent. Block III contains the device physics. For example in the case of long GaAs devices the carrier dynamics have been successfully represented by explicit relations between field and velocity, and field and diffusion (see, e.g., reference 2). For the SD a more accurate description of the carrier dynamics is required and we solve the Boltzmann transport equation (BTE).

II

The solutions to the BTE are approximate. We assume that the electron distribution is Maxwellian, and peaks at a finite value of momenta. The distribution function has the

form

$$f(\vec{p}_i) = \left(\frac{n_i}{T_i^{3/2}} \right) \exp - \left(\frac{\hbar^2 (k - \vec{p}_i)^2}{2m_i k_B T_i} \right) \quad (1)$$

and is referred to as a 'displaced' or 'shifted' Maxwellian (see, e.g., Butcher, reference 3).

For multivalley semiconductors, such as GaAs, the subscript 'i' = 1,2,... identifies the specific valley. And for each valley, the carrier density, n_i , momenta, \vec{p}_i , and temperature T_i , must be determined. Each of these quantities have a space and time dependence, and vary as the field, F , varies. In the calculations below, we ignore spatial dependence and solve the homogeneous zero, first and second moments of the BTE (see, e.g., references 4 and 5). These are, respectively

(particle conservation)

$$\frac{\partial n_i}{\partial t} = \frac{-n_i}{\tau_{n_i}} + \frac{n_j}{\tau_{n_j}}, \quad (2)$$

(momentum balance)

$$\frac{\partial n_i \vec{p}_i}{\partial t} = -en_i F - \frac{n_i \vec{p}_i}{\tau_{p_i}}, \quad (3)$$

(energy balance)

$$\frac{\partial}{\partial t} \left(\frac{n_i p_i^2}{2} + \frac{3n_i k_B T_i}{2} \right) = \quad (4)$$

$$\frac{-en_i F \cdot \vec{p}_i}{m_i} - \frac{3n_i k_B T_i}{2 \tau_{E_i}} + \frac{3n_j k_B T_j}{2 \tau_{E_j}} \quad (5)$$

where a_i represents the number of equivalent valleys, m_i , the effective mass of the i th valley and ' $1/:$ ' represents density, momenta, and energy scattering rates. Table 1 identifies these rates. Table 2 lists the values of the relevant parameters used in this calculation. The consequences of varying these parameters will be discussed at a later time.

III

The calculation is performed for the situation where the SD is part of a resistive circuit. The SD is uniformly doped to N_0 particles/cc. Initially all carriers have zero velocity. A bias ϕ across the load and SD is then stepped from zero to a finite value. The time dependence of V and the potential across the SD are constrained by the load line equation

$$\phi_0 = \phi_{SD} + RN_0 eV(t)A \quad (6)$$

where A is the cross sectional area of the SD and

$$N_0 V(t) = n_1 p_1 / m_1 + a_2 n_2 p_2 / m_2 \quad (7)$$

is the net drift velocity. The subscripts '1' and '2' denote respectively, the central and satellite valleys. The solutions to the above equations along with those represented by blocks I and II of figure 1 result in a uniform time dependent change in field and velocity across the SD. Because of the assumption of uniformity, carriers at the anode, as well as at other points in the SD, have the same velocity as carriers at the cathode. Apart from the artificial nature of this assumption, the calculated velocity can be used to determine the time T , for a carrier with a zero initial drift velocity to travel a distance L , in a time varying field:

$$L = \int_0^T V(t) dt \quad (8)$$

The uniform field calculations are relevant to transit-time considerations.

Examples of the calculations are shown in figures 2 through 4 for different values of the ratio R/R_0 . Here $R_0 = L/(N_0 e \mu_0 A)$, where μ_0 is the low field mobility of the central valley corresponding only to LO phonon intravalley scattering. Also, recalling for GaAs with doping levels not exceeding $10^{16}/cc$, that the equilibrium velocity electric field relation differs only marginally from that for zero impurity scattering, we perform the calculation for zero impurity scattering.

IV

Figure 2 shows $V(t)$ for two values of R/R_0 . The value of ϕ exceeds the threshold field for negative differential mobility (NDM) and we see the familiar overshoot effects. With respect to the influence of the load we see that the peak velocity is higher and the relaxation time shorter for the $R/R_0 = 0.01$ circuit. The major contribution to this difference is the larger potential drop across the SD for the lightly loaded circuit. We point out that it is possible to find a particular pair of values for ϕ and R/R_0 for which the response times for light and heavily load circuits are similar. From another point of view the load may play a more significant role. This is shown in figure 3 and 4 where we display the velocity versus electric field relation as a function of SD length.

The calculations show the length and load dependence of the NDM slope for the two terminal SD. In our calculations NDM arises only from electron transfer. The shortest device exhibits the highest velocities and the weakest NDM region (off scale), both features reflecting the fact that the transit times are considerably shorter than the thermalization times (see also reference 1). With regard to the load line dependence we see, for a SD of given length, the presence of a 'softer' NDM region and somewhat higher velocities when situated in the more heavily loaded circuit. The consequences of this result are somewhat difficult to predict at this time, insofar as the only detailed device analysis concerned with the influence of NDM slopes and velocities comes from studies on longer devices. In these earlier studies we find that shallow NDM regions lead to broad domains, a feature important to device stability as well as gain when operated as a two terminal amplifier. On the other hand, the NDM slope is less significant than the ratio of the 'peak' and 'valley' drift velocities when the device is operated as a uniform field oscillator (see reference 2). For two terminal SD the consequences of the load line dependence must await further studies which include both reactive circuit elements and nonuniform fields.

In conclusion, through solutions of the Boltzmann transport equation, the circuit and Poissons equations, we have demonstrated that the transient characteristics, including the drift velocity versus electric field relation are dependent on the properties of the external circuit.

The authors thank P. Kirschner and P. Wochomurka for their assistance. This study was supported by the Office of Naval Research, to whom we are grateful.

References

- (1) J. G. Ruch, IEEE Transactions on Electron Devices, ED-19, 652 (1972).
- (2) M. P. Shaw, H. L. Grubin, P. R. Solomon, "The Gunn-Hilsum Effect", Academic Press, N.Y. 1979.
- (3) P. N. Butcher, Repts. Prog. Phys. 30, 97 (1967).
- (4) R. Bosch and H. W. Thim, IEEE Transactions on Electron Devices, ED-21, 16 (1974).
- (5) K. Blotekjar, IEEE Transactions on Electron Devices, ED-17, 38 (1970).

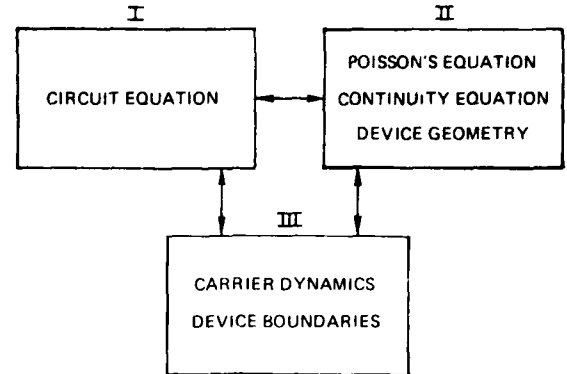


Figure 1. Summary of device simulation.

TABLE 1 SCATTERING PROCESSES : (CV) CENTRAL VALLEY, (SV) SATELLITE VALLEY		
$1/\tau_{n1}$, $1/\tau_{E1}$		CV to all SV
$1/\tau_{n2}$, $1/\tau_{I2}$		All SV to CV
$1/\tau_{p1}$		Intravalley CV and CV to all SV
$1/\tau_{p2}$, $1/\tau_{S2}$		Intravalley SV and SV to remaining SV and one SV to CV
$1/\tau_{S1}$		CV to one SV

TABLE 2 PARAMETERS USED IN CALCULATION			
PARAMETERS	$\Gamma(000)$	X(100)	COMMON
Number of equivalent valleys	1	3	
Effective mass (m_e)	0.067	0.40	
Γ -X Separation (ev)			0.36
Lattice Const. (a_A)			5.64
Density (gm/cm^3)			5.37
POLAR OPTICAL SCATTERING			
Static Diel. Const.			12.53
High Freq. Diel. C			10.82
L0 phonon (ev)			0.0354
Γ -X Scattering			
Coupl. Cons. (ev/cm)			0.621×10^9
Phonon energy (ev)			0.0300
X-X Scattering			
Coupl. Const. (ev/cm)		1.064×10^9	
Phonon energy (ev)		0.0300	
Acoustic Scattering			
Deform. Pot (ev)	7.0	7.0	
Acoustic Vel. (c/s)			5.22×10^5

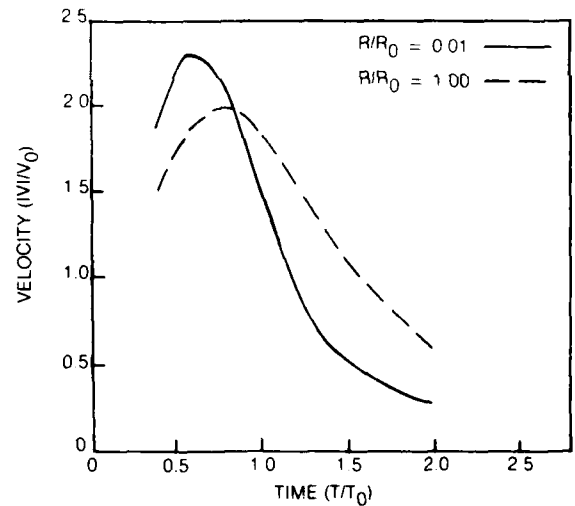


Figure 2. Magnitude of drift velocity versus time for different resistive loads. Here the bias field is 25 kv/cm $V_0 = 3.68 \times 10^7$ cm/sec and $T_0 = .315$ psec.

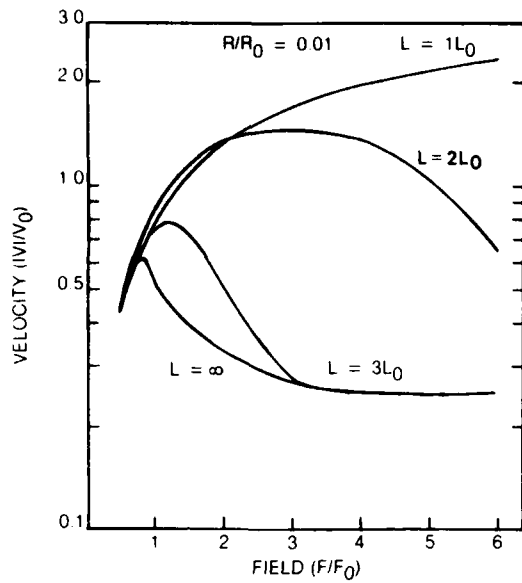


Figure 3. Magnitude of drift velocity versus electric field versus device length. Here $F_0 = 4.44$ kv/cm, $L_0 = .116$ μ m, $V_0 = 3.68 \times 10^7$ cm/sec, and $R/R_0 = 0.01$.

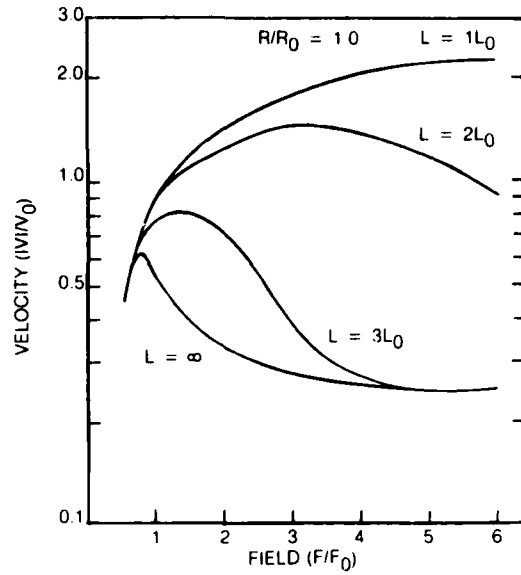


Figure 4. As in figure 3 but with $R/R = 1.0$.

IV. NUMERICAL CODES, PARTIALLY SPONSORED BY
ONR, CONTRACT N00014-78-C-0269

- GAAS (1): BOLTZMANN TRANSPORT EQUATION (BTE) SCATTERING INTEGRALS.
- GAAS (2): UNIFORM FIELD BTE TRANSIENT EQUATIONS.
- GAAS (3): ONE-DIMENSIONAL NONUNIFORM FIELD BTE SPATIAL AND TEMPORAL TRANSIENTS.
- GAAS (3) 1: BTE INTEGRALS FOR THREE-LEVEL TRANSFER.
- GAAS (4): TWO-DIMENSIONAL NONUNIFORM FIELD BTE SPATIAL AND TEMPORAL TRANSIENTS.
- GAASFET: FIELD EFFECT TRANSISTOR SIMULATIONS

V. REFERENCES

1. Butcher, P. N., and C. J. Hearn: Electronics Letters, 4, 459 (1968).
2. Rees, H. D.: IBM J. Res. Develop. 13, 537 (1969).
3. Ruch, J. G.: IEEE Trans. Electron Devices ED-19, 652 (1972).
4. Maloney, T. J., and J. Frey: J. Appl. Phys. 48, 781 (1977).
5. Kratzer, S., and J. Frey: J. Appl. Phys. 49, 4064 (1978).
6. Hill, G., P. N. Robson, and A. Majerfeld: Electronics Letts. 13, 235 (1977).
7. Grubin, H. L., D. K. Ferry, G. J. Iafrate, and J. R. Barker: Microstructure Science and Engineering/VLSI, 2 (1981). Academic Press, N.Y.
8. Rees, H. D.: Sol. State Commun. 26A, 416 (1968); J. Phys. C 5, 64 (1972), and Jones, D., and H. D. Rees, J. Phys. C 6, 1781 (1973).
9. Blotekjar, K.: IEEE Trans. Electron Devices ED-14, 38 (1970).
10. Grubin, H. L., D. K. Ferry and J. R. Barker: Proc. 1979 IEDM. (IEEE Press, N.Y.), 394 (1979).
11. Bosch, R., and H. Thim: IEEE Trans. Electron Dev. ED-21, 16 (1974).
12. Cheung, P. S., and C. J. Hearn: Electron Letts. 8, 79 (1972).
13. Shur, M. S. and L. F. Eastman: IEEE Trans. Elec. Dev., ED-26, 1677 (1979), and IEEE Electron Devices Letts. EDL-1, 147 (1980).
14. See, E. G., S. Laval, C. Bru, C. Arnodo, and R. Castagne: Proc. 1980 IEDM. (IEEE Press, N.Y.), 626, (1979).
15. See, E. G., N. Hollis, N. Dandekar, L. F. Eastman, M. Shur, D. Woodard, and C. Wood: Proc. 1980 IEDM (IEEE Press, N.Y.), 622 (1980).
16. Zuleg, R.: IEEE Electron Device Letts., EDL-1, 234 (1980).
17. Frohlich, H.: Proc. Royal Soc. A188, 521 (1947); and Frohlich, H. and B. V. Paranjape: Proc. Phys. Soc., B69, 21 (1956).

REFERENCES (Cont'd)

18. Butcher, P. N.: Rept. Prog. Phys., 30, 97 (1967).
19. Grubin, H. L., and T. M. McHugh: Solid State Electronics, 21, 69 (1978).
20. Greiling, P.: Private Communication.
21. Kromer, H.: Solid State Electronics, 21, 61 (1978).

VI. FIGURE CAPTIONS

1. Flow diagram representing motivating disciplines in device physics.
2. Scattering rates for the parameters of Table 1. Integrals are from Ref. 18. CV refers to the central valley and SV to the staellite valley.
3. Field profiles for a high field propagating domain. Dotted curve is obtained from the mobility equations. Solid curve is obtained from moment equations. From Ref. 12.
4. Schematic representation of a coplanar two-dimensional device with a cathode notch.
5. For $N_0=10^{17}/\text{cm}^3$ and $\tau_0=.3\text{ps}$, transient central valley behavior. (a) Momentum versus time, (b) Temperature versus time, (c) momentum density versus time.
6. As in Fig. 5, but for satellite valley.
7. Mean velocity, from Figs. 5 and 6. Here $\sqrt{2m_c k_B T_0} = 3.7 \times 10^7$ cm/sec.
8. Time dependent bias field used to show rise time dependence of transient velocity. For all of these calculations $F_{OM} = 21.5$ kV/cm and $F_{Om} = .43$ kV/cm.
9. For this pulse $t_1 = 500/\tau_0$, $t_2 = 600/\tau_0$, $t_3 = 1200/\tau_0$. $\tau_0 = .3\text{ps}$. (a) Mean velocity versus field ($F_0 = 4.3$ kV/cm), (b) central valley population versus time, (c) central valley temperature versus time.
10. As in Fig. 9. Here $t_1 = 50/\tau_0$, $t_2 = 60/\tau_0$, $t_3 \approx 110/\tau_0$.
11. As in Fig. 9. Here $t_1 = 5/\tau_0$, $t_2 = 10/\tau_0$, $t_3 = 15/\tau_0$.
12. Self-excited oscillation, for the circuit displayed in Fig. 13. $N_0 = 10^{15}/\text{cm}^3$. Oscillation frequency is 78 GHz.
13. Maximum frequency for self-excited oscillations.
14. Length dependence of negative differentail mobility.
15. Schematic representation of device and circuit configuration for submicron homogeneous field profiles. Inhomogeneous doping profile is treated as a "jellium" distribution.
16. (a) Fractional central valley population versus distance, (b) Central valley temperature versus distance, (c) Staellite valley temperature versus distance. Computation occurs at time $t/\tau_0 = 4$. τ_0 is the LO phonon internally scattering time and equals 0.32 ps. T in this figure is room temperature. The gradient of N is zero at the boundaries. All nonuniformities are due to the notch.

VI. FIGURE CAPTIONS (Cont'd)

17. (a) Mean velocity versus distance, (b) Field versus distance, (c) Free carrier density versus distance at time $t/\tau_0 = 4$.
18. As in III 13, but at $t/\tau_0 = 16$.
19. As in III 14, but at $t/\tau_0 = 16$.
20. Boundary Condition approximations to one- and two-dimensional problems.

TABLE 1

PARAMETERS USED IN CALCULATION

Parameters	$\Gamma(000)$	X(100)	Common
Number of Equivalent valleys	1	3	
Effective mass (m_e)	0.067	0.40	
Γ -X Separation (ev)			0.36
Lattice Const. (a_A)			5.64
Density (gm/cm^3)			5.37
POLAR OPTICAL SCATTERING			
Static Diel. Const.			12.53
High Freq. Diel. C.			10.82
LO phonon (ev)			0.0354
Γ -X Scattering			
Coupl. Cons. (ev/cm)			0.621×10^9
Phonon energy (ev)			0.0300
X-X Scattering			
Coupl. Const. (ev/cm)			1.064×10^9
Phonon energy (ev)			0.0300
Acoustic Scattering			
Deform. Pot (ev)	7.0	7.0	
Acoustic Vel. (c/s)			5.22×10^5

FIG. 1

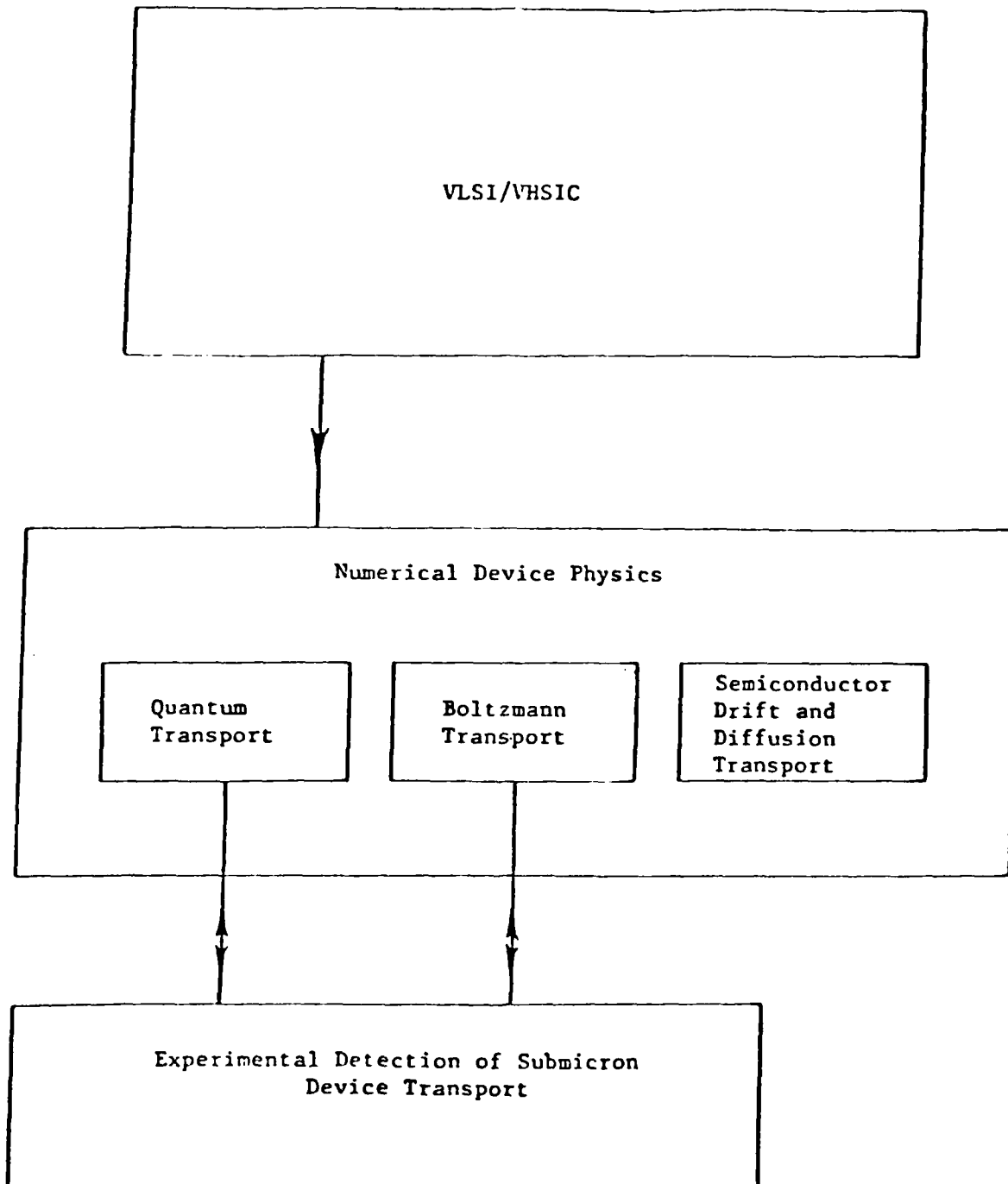


FIG. 2

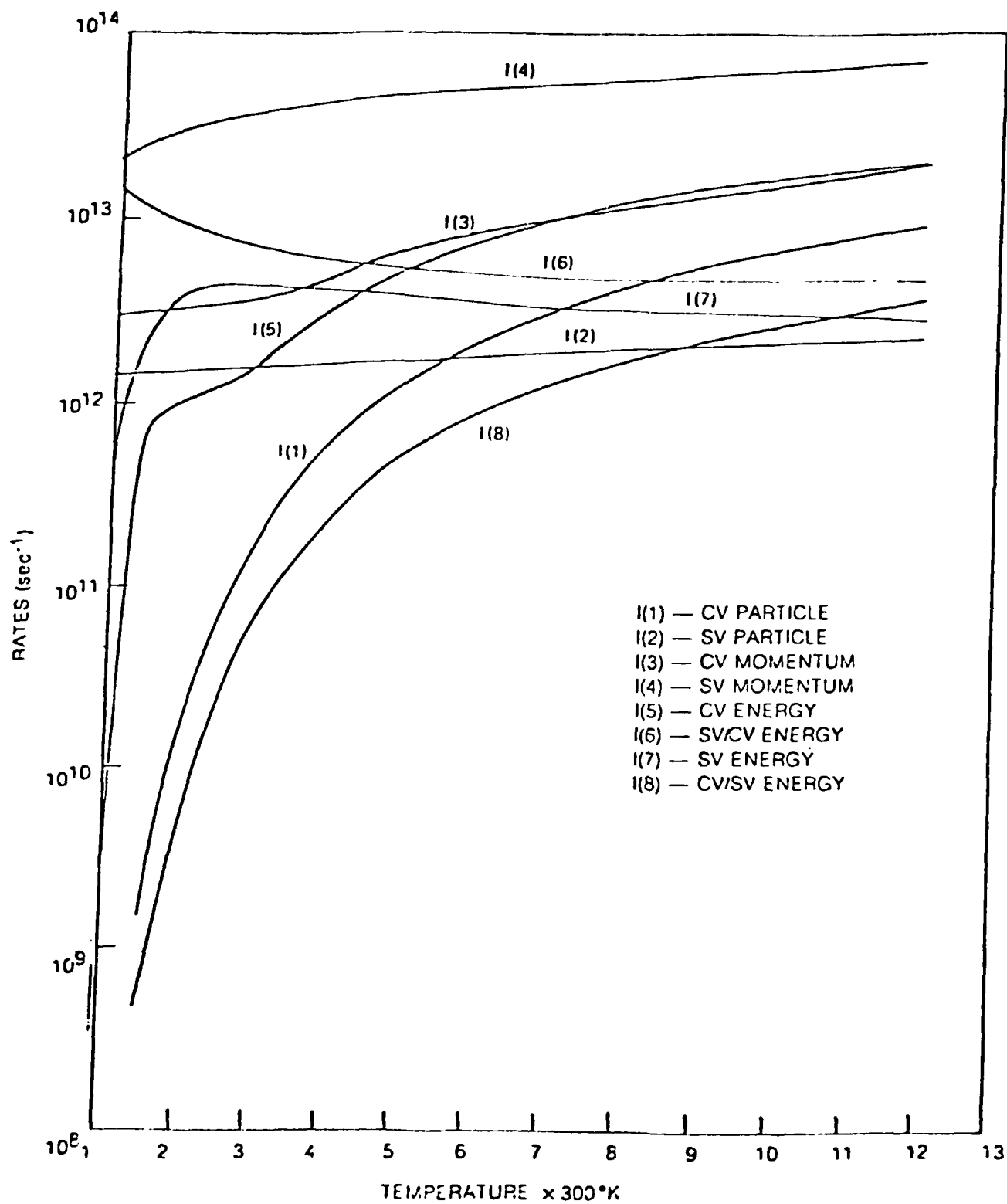


FIG. 3

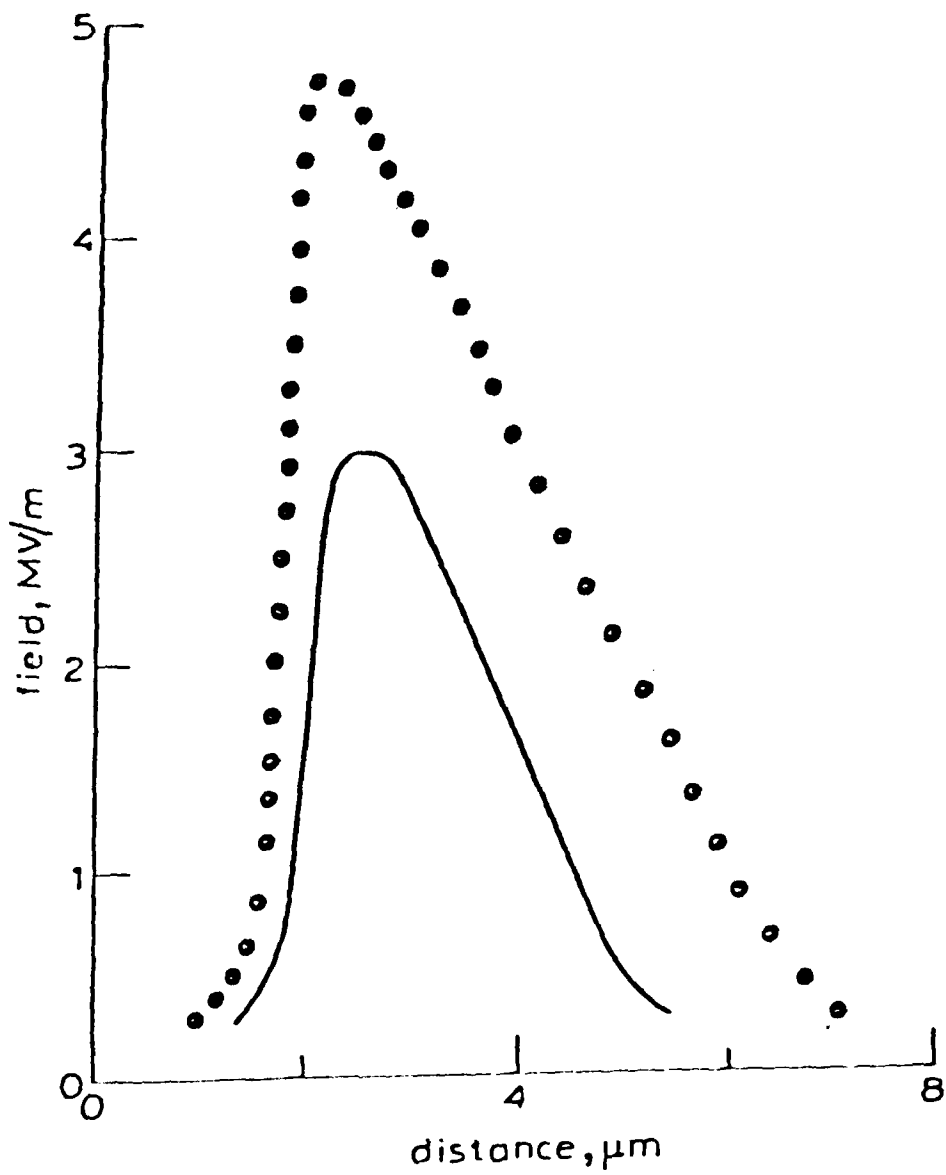


FIG. 4

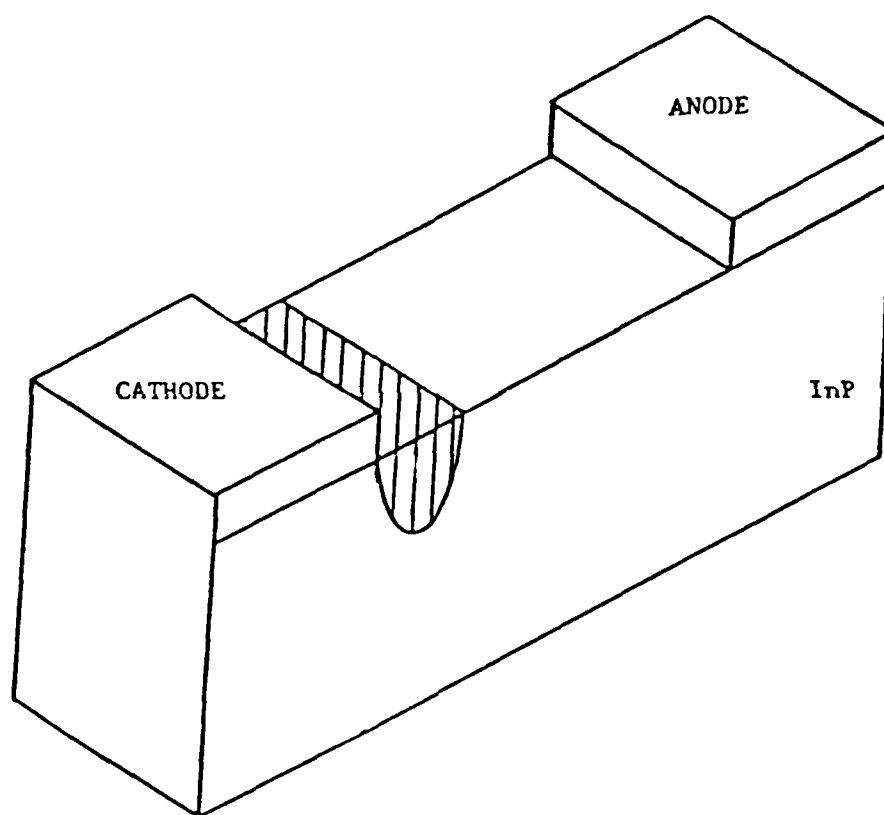


FIG. 5

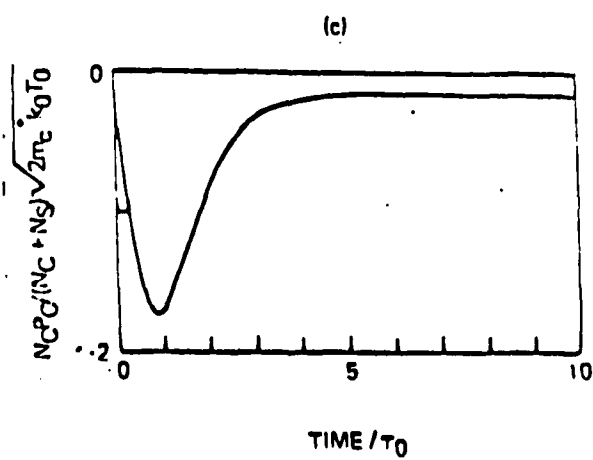
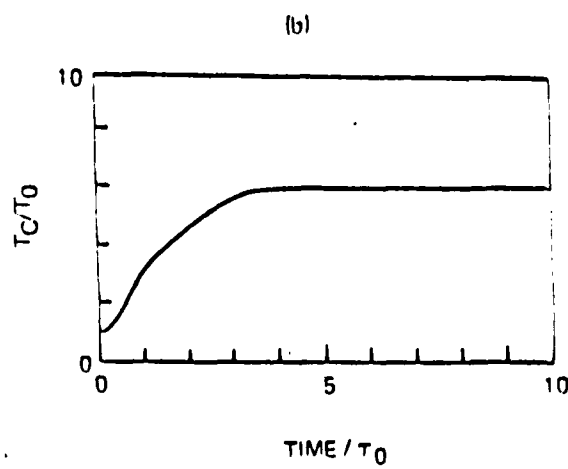
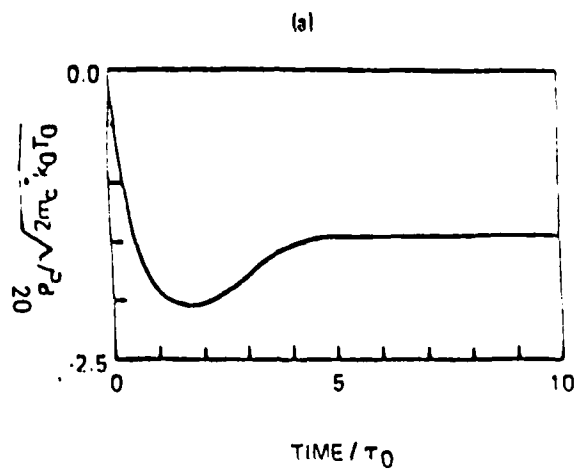


FIG. 6

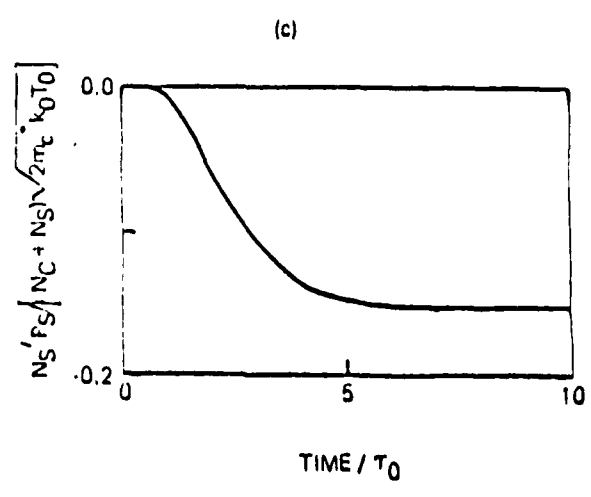
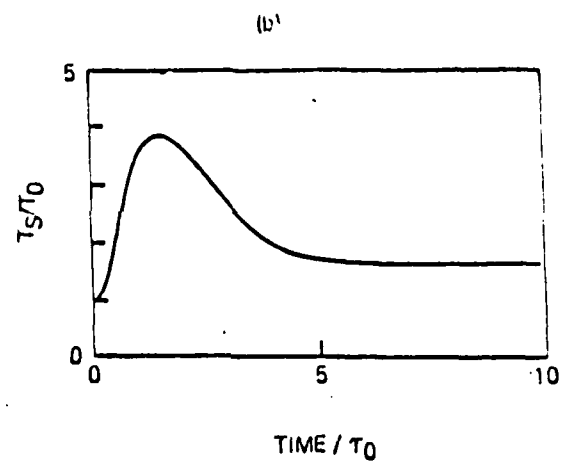
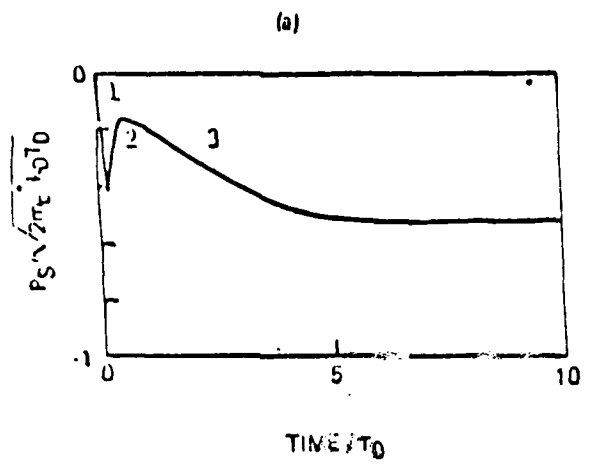


FIG. 7

CARRIER VELOCITY

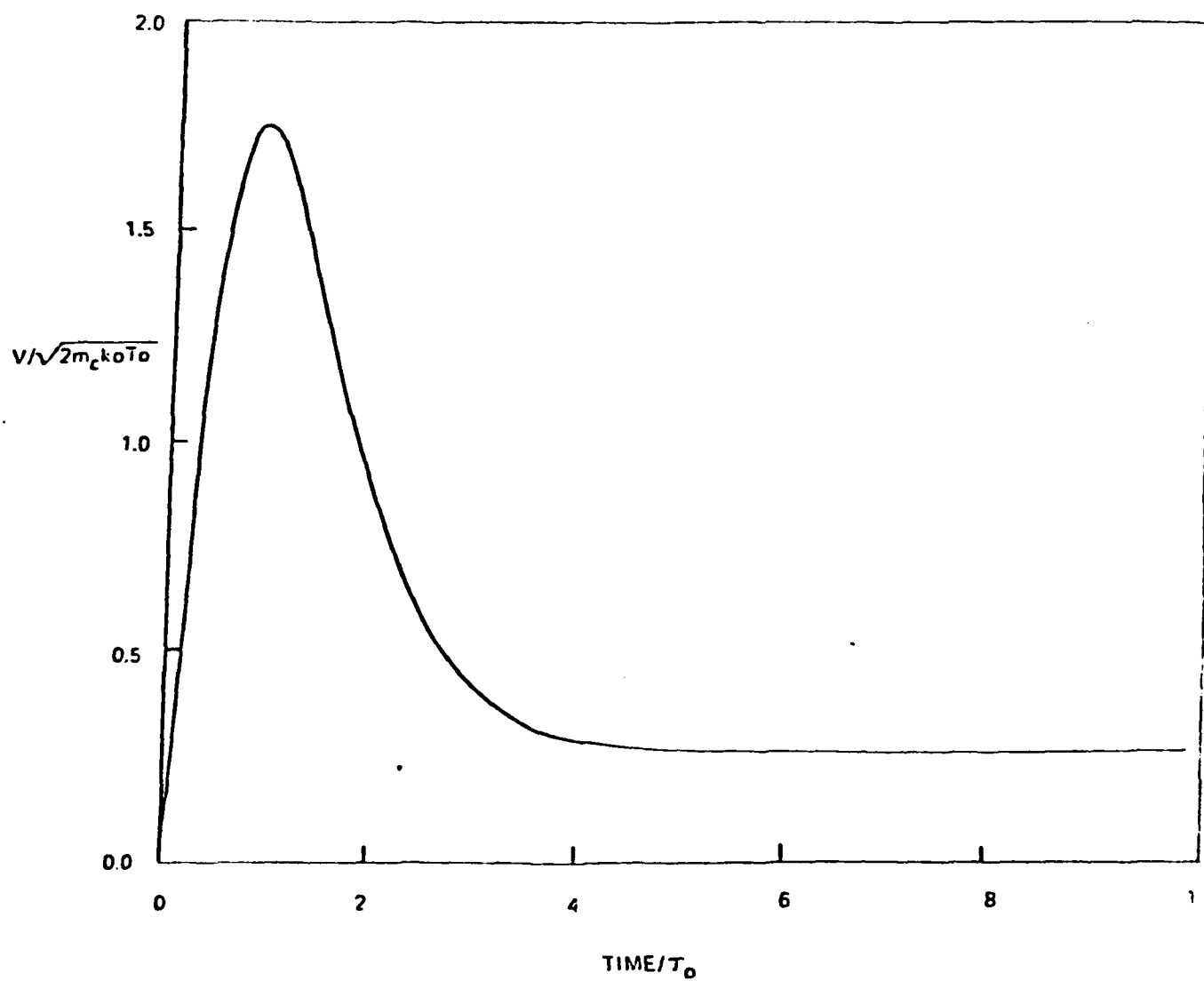


FIG. 8

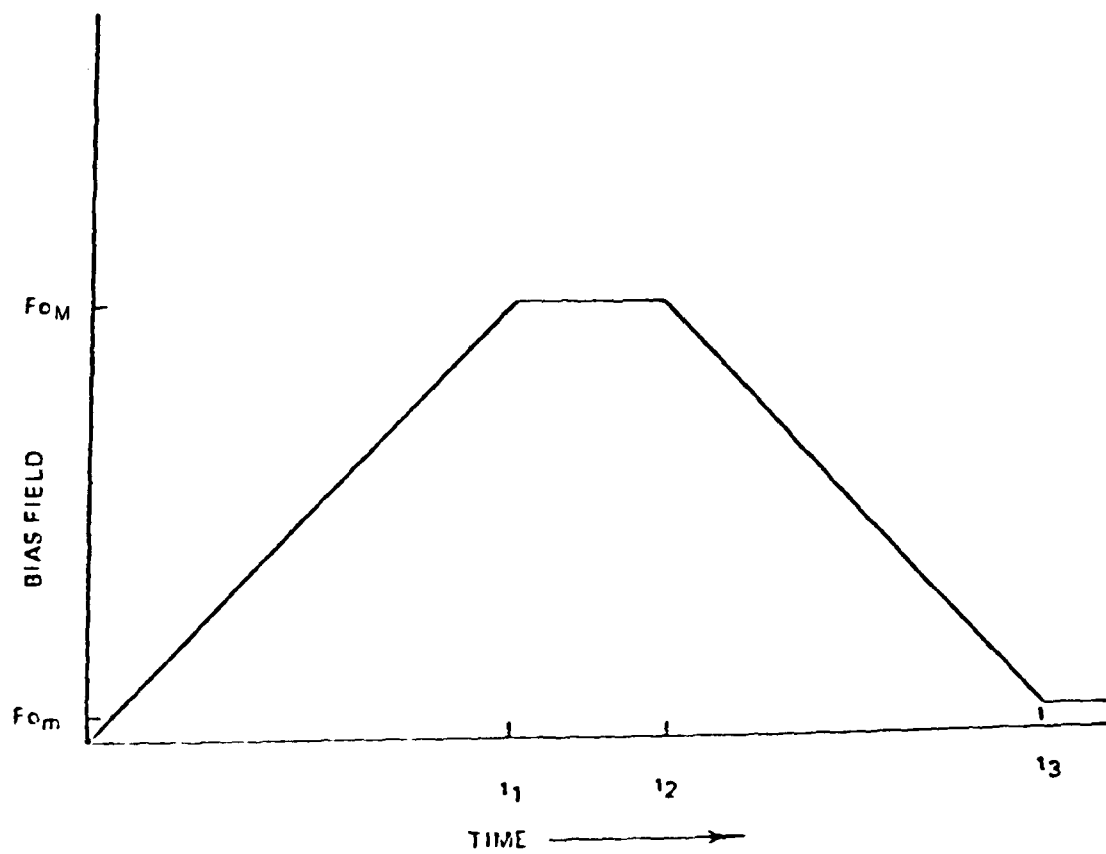


FIG. 9

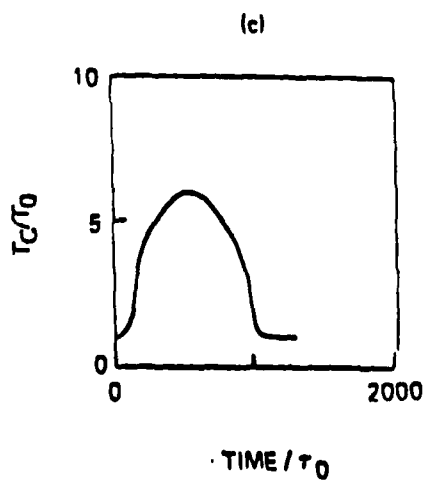
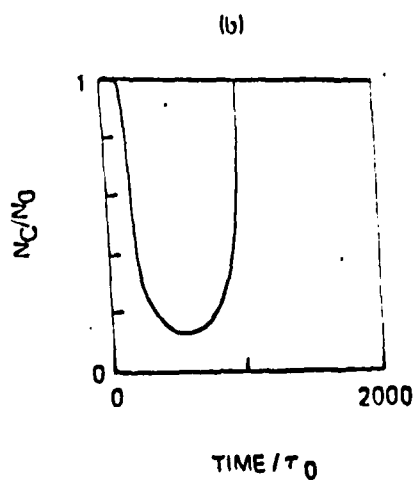
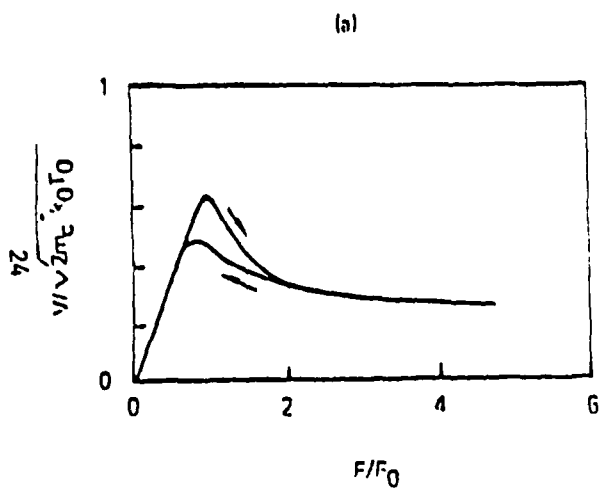


FIG. 10

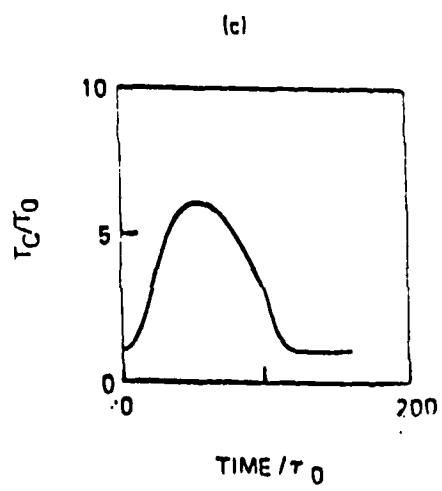
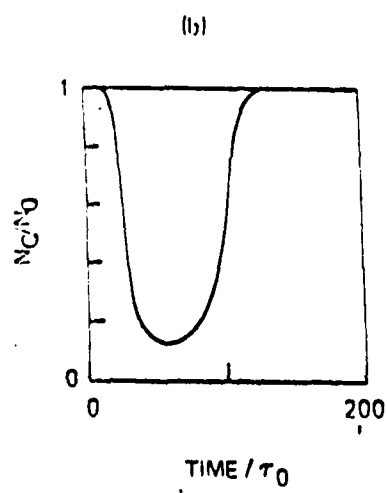
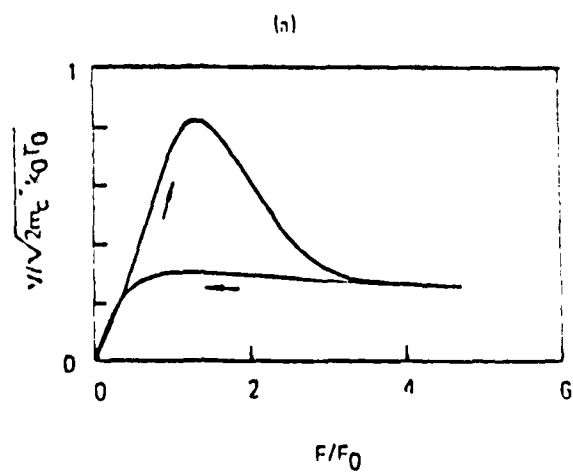


FIG 11

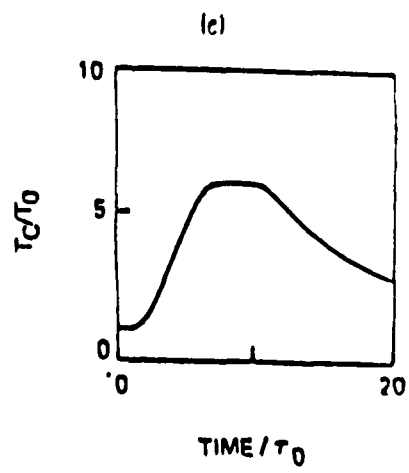
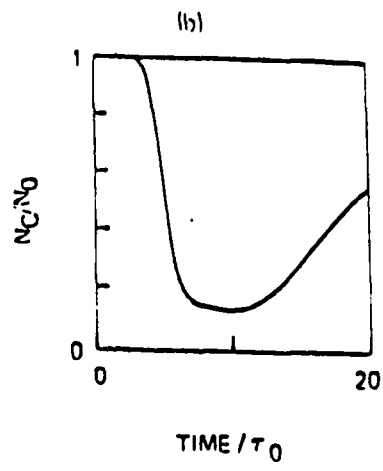
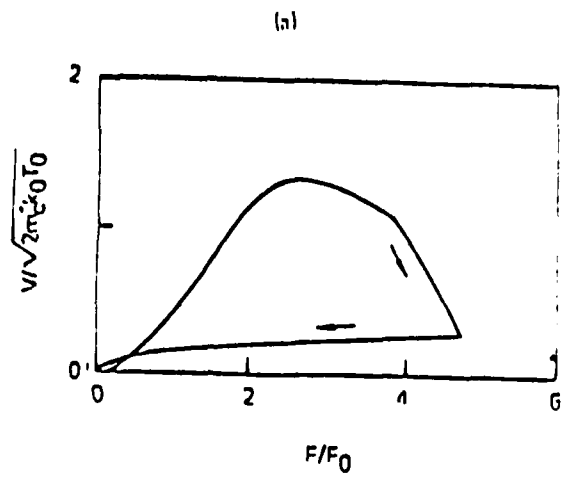


FIG. 12

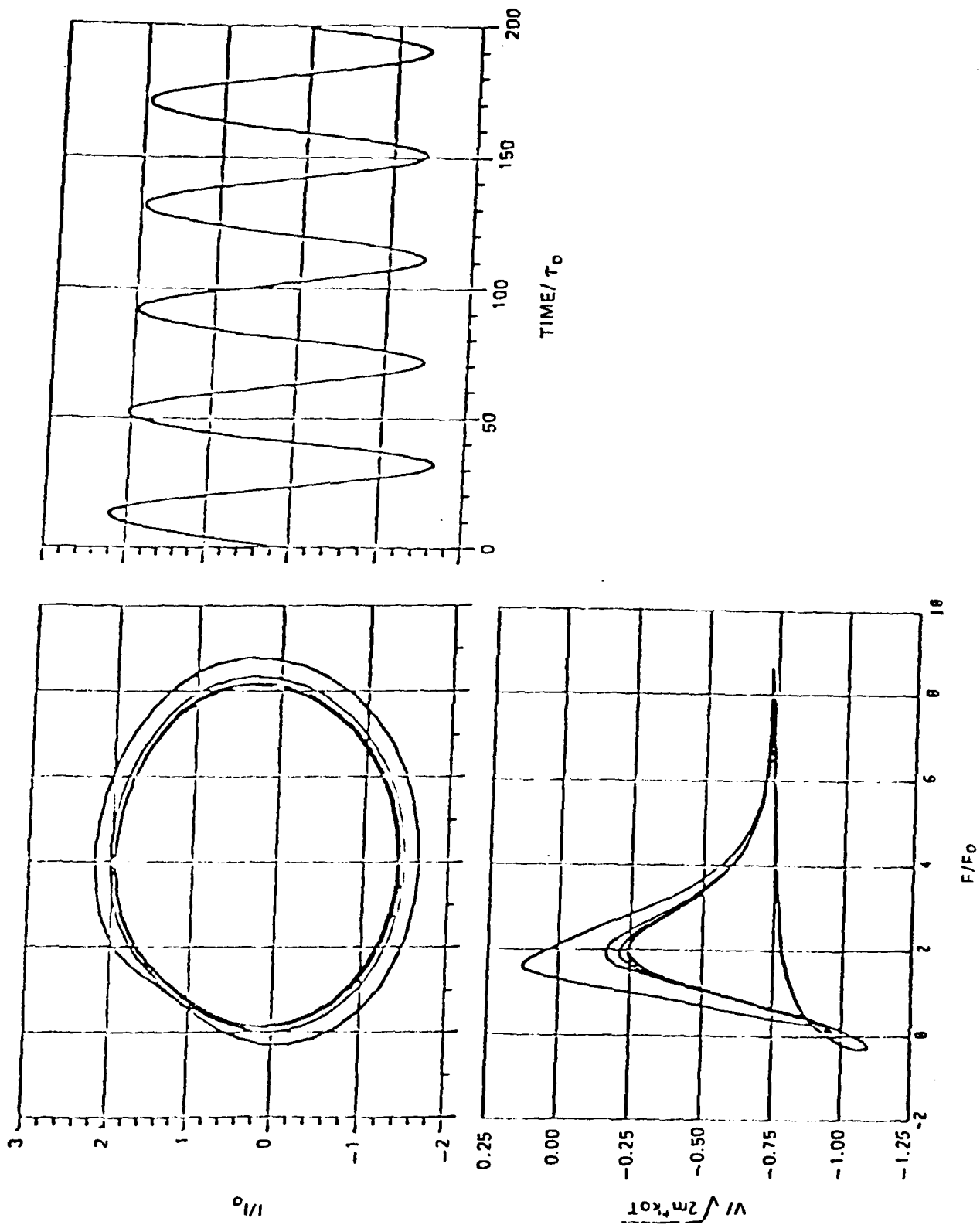
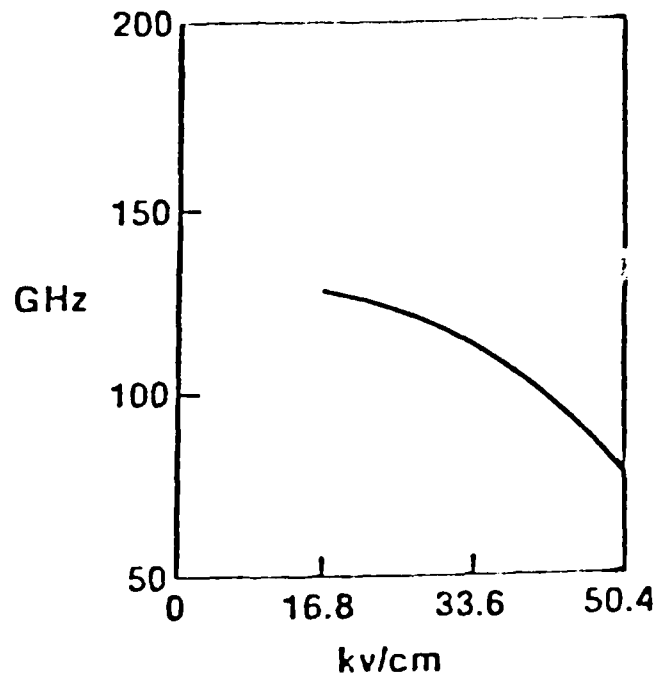
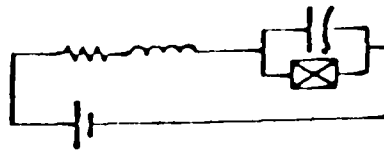


FIG. 13



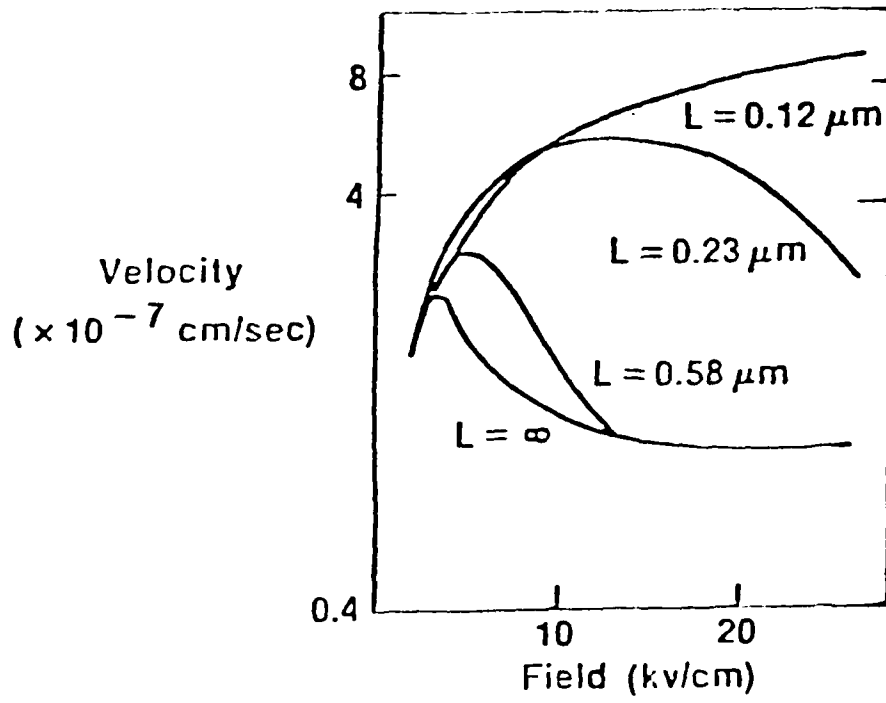


FIG. 15

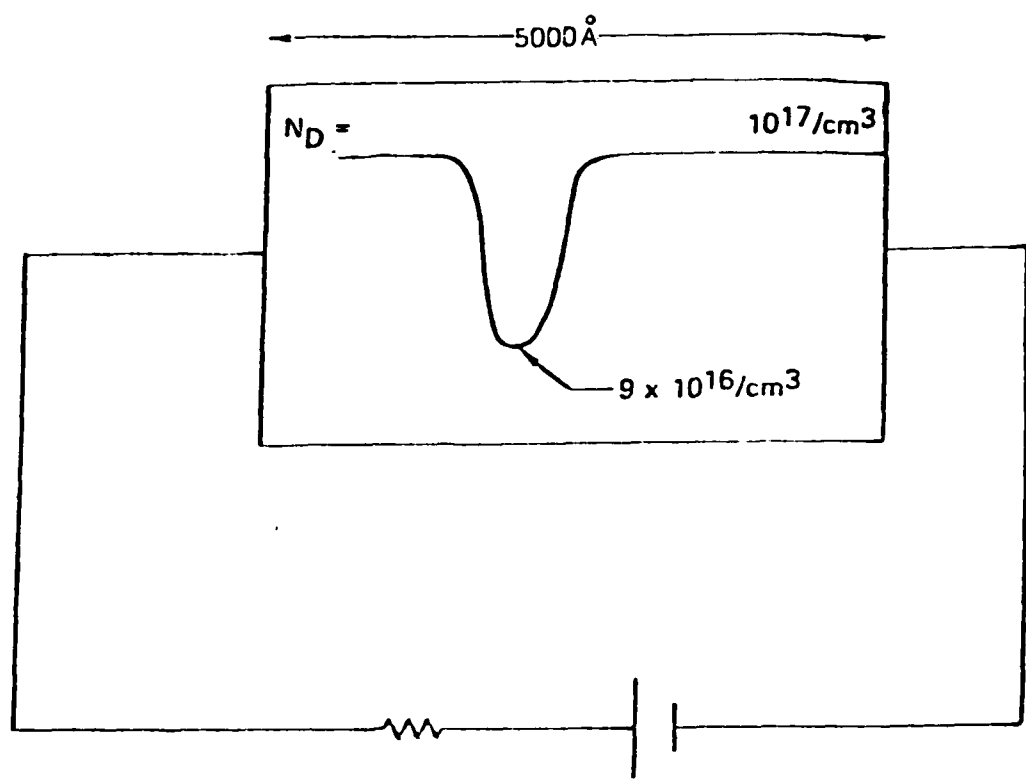
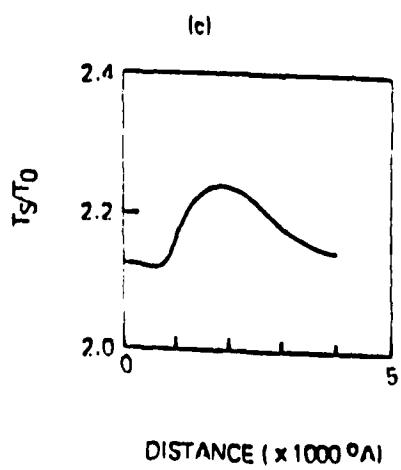
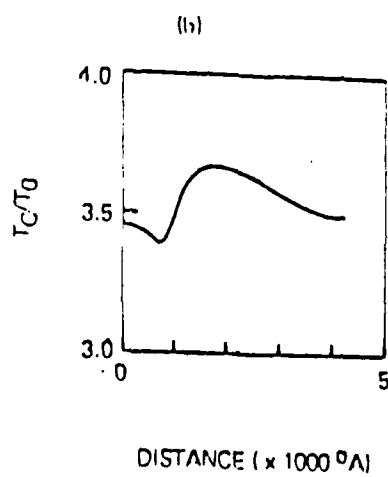
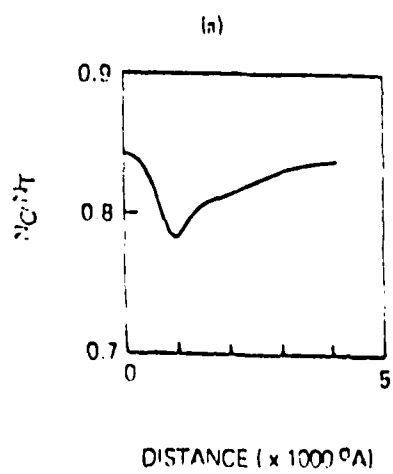
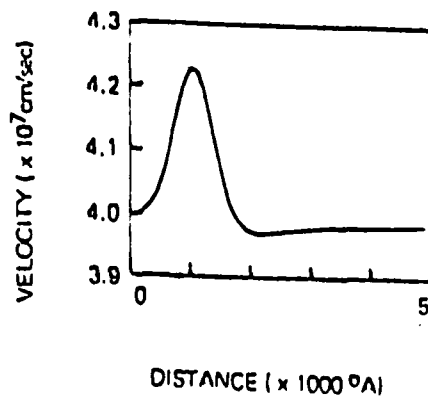


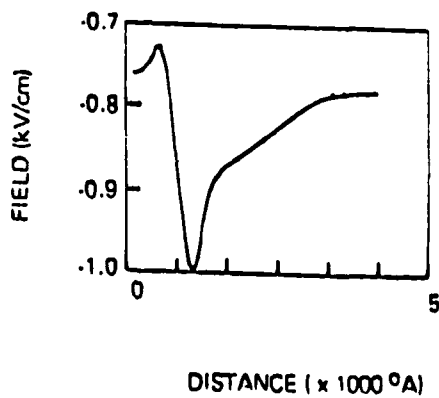
FIG. 16



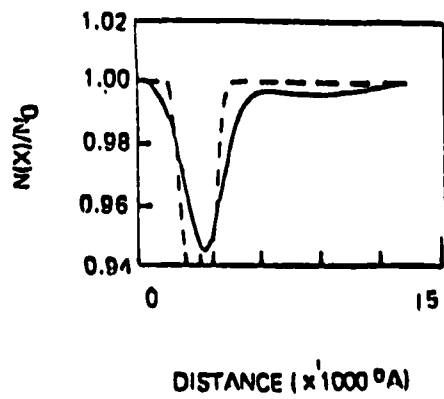
(a)

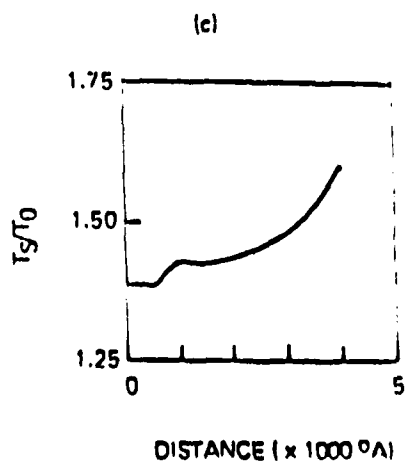
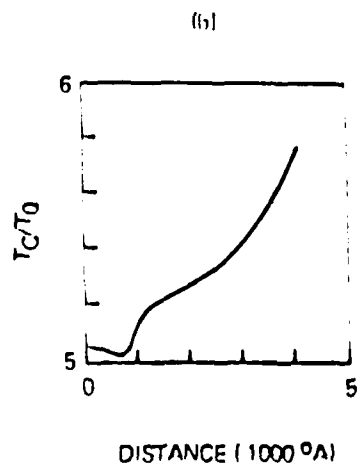
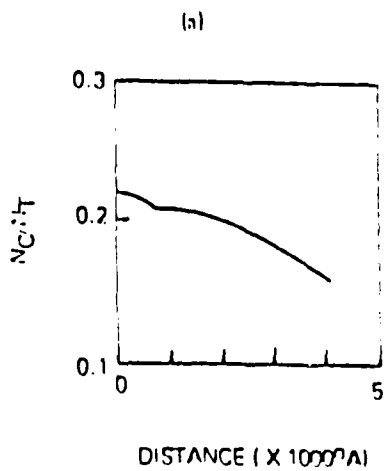


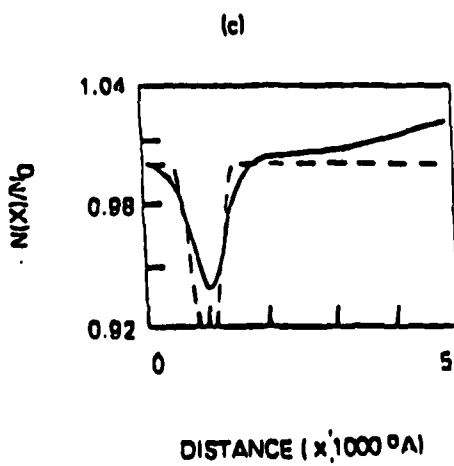
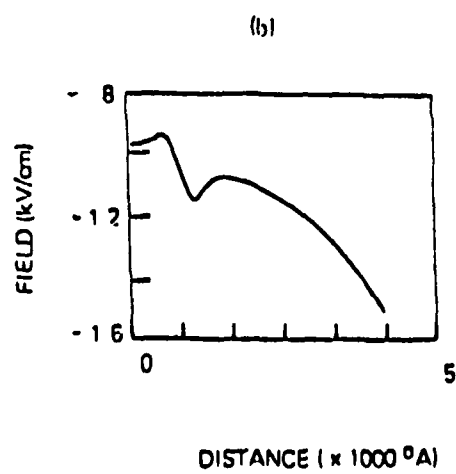
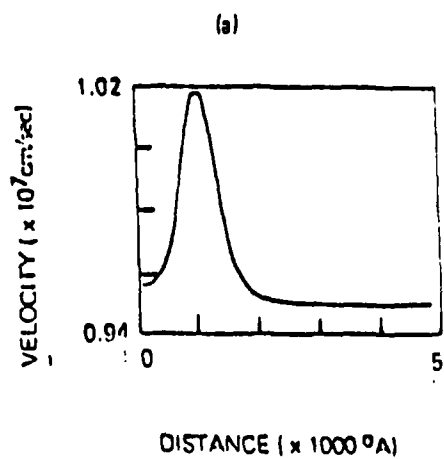
(b)



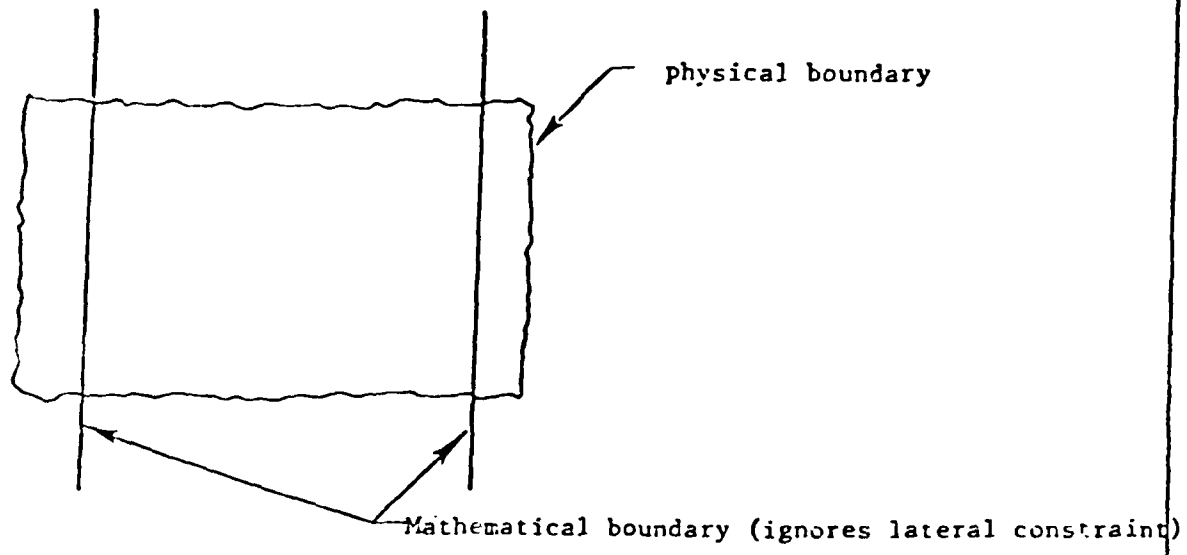
(c)



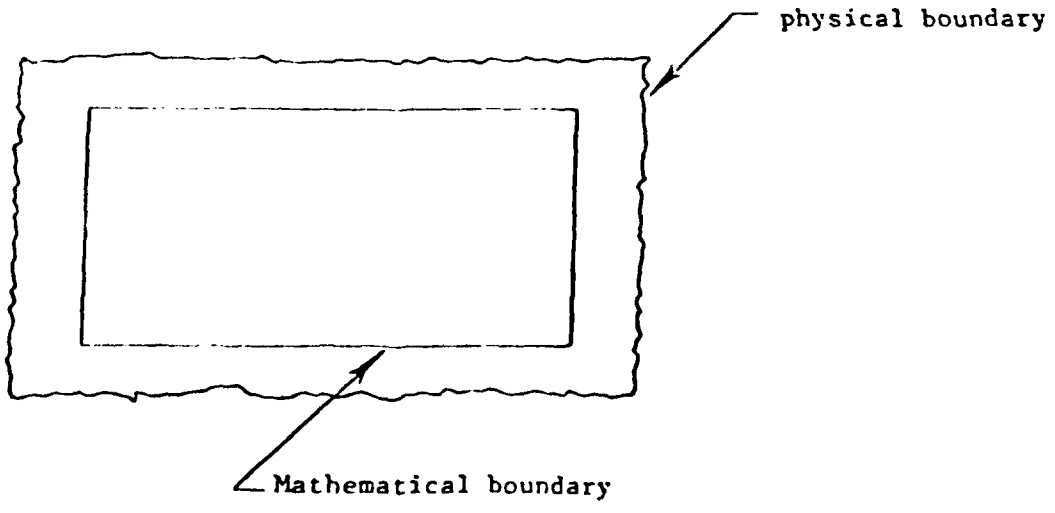




One Dimensional Calculations



Two Dimensional Calculations



Distribution List

<u>Name</u>	<u>Number of copies</u>
Scientific Officer Director, Electronic and Solid State Sciences Program Physical Sciences Division Office of Naval Research 800 North Quincy Street Arlington, Virginia 22217 Attention: Dr. Larry R. Cooper Reference: Contract No. N00014-78-C-0269	40
Scientific Officer Office of Naval Research Arlington, Virginia 22217 ATTN: DODAAD Code N00014	1
Administrative Contracting Officer Office of Naval Research Arlington, Virginia 22217 ATTN: DODAAD Code FY1725	1
Director, Naval Research Laboratory Attention: Code 2627 Washington, D. C. 20375	6
Office of Naval Research Department of the Navy Arlington, Virginia 22217 Attention: Code 102IP	6
Defense Documentation Center Building 5, Cameron Station Alexandria, Virginia 22314	12
Office of Naval Research Branch Office-Boston 495 Summer Street Boston, Massachusetts 02210	1
Dr. H. L. Grubin Scientific Research Associated, Inc. P. O. Box 498 Glastonbury, Connecticut 06033	6
Dr. G. A. Peterson UTRC	27

